Earth-Science Reviews 216 (2021) 103574

Contents lists available at ScienceDirect

Earth-Science Reviews

journal homepage: www.elsevier.com/locate/earscirev

Landslide failures detection and mapping using Synthetic Aperture Radar: Past, present and future

Alessandro Cesare Mondini [a,*], Fausto Guzzetti [b,a], Kang-Tsung Chang [c], Oriol Monserrat [d], Tapas Ranjan Martha [e], Andrea Manconi [f,g]

[a] Consiglio Nazionale delle Ricerche, Istituto di Ricerca per la Protezione Idrogeologica, via Madonna Alta 126, I-06128 Perugia, Italy
[b] Presidenza del Consiglio dei Ministri, Dipartimento della Protezione Civile, via Vitorchiano 2-4, I-00189 Rome, Italy
[c] National Taiwan University, Department of Geography, No. 1, Section 4, Roosevelt Rd, Da'an District, Taipei City 106, Taiwan
[d] Centre Technologic de Telecomunicacions de Catalunya, Castelldefels, Barcelona, Spain
[e] National Remote Sensing Centre, Indian Space Research Organisation, Hyderabad 500037, India
[f] Eidgenössische Technische Hochschule Zürich, Department of Earth Sciences, Sonneggstrasse 5, 8092 Zürich, Switzerland
[g] Gamma Remote Sensing AG, Worbstrasse 225, 3073 Gümligen, Switzerland

ARTICLE INFO

Keywords:
Landslide
SAR
Detection
Mapping
Inventory
Amplitude
Phase
Coherence
DInSAR
Modelling

ABSTRACT

Landslides are geomorphological processes that shape the landscapes of all continents, dismantling mountains and contributing sediments to the river networks. Caused by geophysical and meteorological triggers, including intense or prolonged rainfall, seismic shaking, volcanic activity, and rapid snow melting, landslides pose a serious threat to people, property, and the environment in many areas. Given their abundance and relevance, investigators have long experimented with techniques and tools for landslide detection and mapping using primarily aerial and satellite optical imagery interpreted visually, or processed by semi-automatic or automatic procedures or algorithms. Optical (passive) sensors have known limitations due to their inability to capture Earth surface images through the clouds and to work in the absence of daylight. The alternatives are active, "all-weather" and "day-and-night", microwave radar sensors capable of seeing through the clouds and working in presence and absence of daylight. We review the literature on the use of Synthetic Aperture Radar (SAR) imagery to detect and map landslide failures – i.e., the single most significant movement episodes in the history of a landslide – and of landslide failure events – i.e., populations of landslides in areas ranging from a few to several thousand square kilometres caused by a single trigger. We examine 54 articles published in representative journals presenting 147 case studies in 32 nations, in all continents, except Antarctica. Analysis of the geographical location of 70 study areas shows that SAR imagery was used to detect and map landslides in most morphological, geological, seismic, meteorological, climate, and land cover settings. The time history of the case studies reveals the increasing interest of the investigators in the use of SAR imagery for landslide detection and mapping, with less than one article per year from 1995 to 2011, rising to about 5 articles per year between 2012 and 2020, and an average period of about 4.2 years between the launch of a satellite and the publication of an article using imagery taken by the satellite. To detect and map landslides, investigators use a common framework that exploits the phase and the amplitude of the electromagnetic return signal recorded in the SAR images, to measure terrain surface properties and their changes. To discriminate landslides from the surrounding stable terrain, a classification of the ground properties is executed by expert visual (heuristic) interpretation, or through numerical (statistical) modelling approaches. Despite undisputed progress over the last 26 years, challenges remain to be faced for the effective use of SAR imagery for landslide detection and mapping. In the article, we examine the theoretical, research, and operational frameworks for the exploitation of SAR images for landslide detection and mapping, and we provide a perspective for future applications considering the existing and the planned SAR satellite missions.

* Corresponding author.
E-mail address: alessandro.mondini@irpi.cnr.it (A.C. Mondini).

https://doi.org/10.1016/j.earscirev.2021.103574
Received 11 October 2020; Received in revised form 19 February 2021; Accepted 21 February 2021
Available online 1 March 2021

1. Introduction

In all continents landslides contribute to shape landscapes (Densmore et al., 1997; Lavé and Burbank, 2004; Malamud et al., 2004b; Chang et al., 2014), and in many areas they pose a serious threat to people, properties, and the environment (Brabb and Harrod, 1989; Dowling and Santi, 2013; Guthrie, 2013; Nadim et al., 2013; Petley, 2012; Badoux et al., 2016; Grahn and Jaldell, 2017; Froude and Petley, 2018; Herrera et al., 2018; Salvati et al., 2018; Rossi et al., 2019). For geological and geomorphological studies, and for landslide hazard and risk assessments, investigators have long experimented techniques, tools, and methods for mapping landslides, in the field or exploiting terrestrial, aerial, and satellite imagery (Guzzetti et al., 2012).

In the last four decades, Earth Observation (EO) imagery – and many related processing and visualisation techniques and tools – have increased significantly the ability to prepare landslide maps (Joyce et al., 2009; Sassa and Canuti, 2009; Guzzetti et al., 2012; Scaioni, 2013; Casagli et al., 2016). Today, a variety of solutions exist to detect and map landslides applicable in areas of small to very large extent using EO imagery, including the visual interpretation of stereoscopic aerial photography, and the semi-automatic or automatic classification of optical, monoscopic or stereoscopic, imagery taken by space, airborne, drone, or terrestrial platforms (Gokceoglu and Sezer, 2009; Guzzetti et al., 2012; Scaioni, 2013; Scaioni et al., 2014; Casagli et al., 2016, 2017a; Giordan et al., 2018; Zhao and Lu, 2018).

The alternatives to passive (optical) sensors are active sensors. Synthetic Aperture Radar (SAR) remote sensing from airborne and satellite platforms exploits active emissions of electromagnetic radiation in the microwave spectral range – between 0.23 *GHz* (130 *cm*, P-band) and 40 *GHz* (0.65 *cm*, Ka-band) – to illuminate the Earth's surface. Since active radar sensors do not require illumination from the Sun, and microwaves penetrate the clouds, SAR imagery can – in principle – capture the occurrence (or recurrence) of landslides all day long, even in areas where clouds obstruct optical sensors (European Space Agency, 2020c). This makes SAR imagery a potentially ideal solution for the detection and mapping of landslides.

In this article, we attempt a systematic, critical review of the literature on the use of airborne and satellite SAR imagery to detect and map landslide failures – where a failure is "the single most significant movement episode in the [...] history of a landslide", as defined by Hungr et al. (2014) – and landslide failure events i.e., populations of one or many landslides in an area caused by a single trigger (Guzzetti et al., 2012). Similar systematic reviews of the literature on landslide detection and mapping techniques that exploit airborne and satellite, optical (multispectral) imagery, or airborne Lidar terrain data, were completed by e.g., Gokceoglu and Sezer (2009), Guzzetti et al. (2012), Scaioni (2013), Scaioni et al. (2014), Casagli et al. (2017a), and Ray et al. (2020). Our work complements and updates these reviews. Multi-temporal DInSAR techniques (e.g., Ferretti et al., 2001; Berardino et al., 2002; Lanari et al., 2004; Ferretti et al., 2011) have also been used extensively to detect and measure ground surface displacements caused by slow moving landslides – in the range from *mm* to *cm* per year – to update geomorphological and multi-temporal landslide inventory maps (Guzzetti et al., 2012), and to determine and rank the degree of activity (UNESCO Working Party on World Landslide Inventory, 1993) of single or multiple landslides (Bovenga et al., 2006; Farina et al., 2006; Lauknes et al., 2010; Notti et al., 2010; Righini et al., 2012; Bianchini et al., 2012; Ciampalini et al., 2012; Cigna et al., 2013; Bardi et al., 2014; Raspini et al., 2015; Michoud et al., 2016; Solari et al., 2019; Lu et al., 2019a). These techniques were reviewed extensively by e.g., Ciampalini et al. (2015), Casagli et al. (2016), Casagli et al. (2017a), Casagli et al. (2017b), Solari et al. (2020), and are not covered in our work.

The article is organised as follows. After an explanation of the terminology used in the work (Section 2), we describe the construction of the literature database on which we base our review (Section 3). Next, we give a brief description of SAR systems (Section 4). Then we present the theoretical basis, and the practical use of SAR amplitude (Section 5.1) and phase (Section 5.2) for landslide failure detection and mapping. This is followed by a critical analysis of the literature (Section 6), and a comparison of different approaches and methods for landslide detection and mapping using SAR imagery (Section 7). Ultimately, we discuss the theoretical, research, and operational frameworks, and we provide a perspective for the future exploitation of SAR imagery for detecting and mapping landslides (Section 8). We conclude (Section 9) by summarising the main lessons learnt.

2. Terminology

The term "landslide" describes the movement of a mass of rock, debris, or earth down a slope (Cruden and Varnes, 1996; Hungr et al., 2014). Landslides are of different types and forms, span multiple orders of magnitude in size and velocity (Cruden and Varnes, 1996; Hungr et al., 2014; Guzzetti et al., 2012), can evolve through multiple movement episodes (Leroueil et al., 1996; Hungr et al., 2014), and often happen where they have already occurred, through repetitions, recurrences, and reactivations (Temme et al., 2020). The large variability of the landslides complicates the terminology used to describe the slope failures.

We use the term "landslide" to encompass all types of mass movements, and the terms "mass movement" and "slope failure" as synonyms for "landslide". We use the terms "failure" and "landslide failure" as synonyms, to describe the single most significant movement episode in the history of a landslide (Hungr et al., 2014), and the term "landslide event" to describe a population of landslides, encompassing one to many landslide failures in the same general area caused by a single trigger e.g., an earthquake, a rainfall period, a rapid snowmelt event. To describe the individual landslides, we use the same terms and classification schemes adopted by the authors of the original studies, including terms used to describe the type (e.g., "fall", "flow", "slide", "spread", "compound", "complex" (Cruden and Varnes, 1996; Hungr et al., 2014)) and the rate of movement (UNESCO Working Party on World Landslide Inventory, 1995), the areal extent and volume of the single landslides (e.g., "small", "medium", "large" (Fell, 1994; Hungr et al., 2001; Jakob, 2005)), and the magnitude (numerousness) of the landslide populations (Malamud et al., 2004a). We adopt the same approach to describe the quality (e.g., "precision", "accuracy", "completeness" (Jackson Jr et al., 2012; Santangelo et al., 2015)) of the landslide mapping process. We acknowledge that some inconsistency exists in the use of landslide descriptive terms in the literature.

In the article, "landslide detection" (or "detection") refers to the action of noticing or discovering single or multiple landslide failures in the same general area, and "landslide mapping" (or "mapping) refers to the action of delineating the geometry of a landslide and, where possible, the geometry of the landslide internal features – including e.g., the landslide main boundary, the separation between the source, travel, and deposition areas, fractures, pressure ridges – and to portray the landslide information in map form. Given that to map a landslide the landslide has to be known to the interpreter, "mapping" encompasses "detection". We adopt the terminology proposed by Guzzetti et al. (2012) to classify the different types of landslide inventory maps, separating geomorphological, event, seasonal, and multi-temporal inventories.

A "quantitative" mapping method extracts information on the presence (or absence) of landslides from EO imagery using mathematical, statistical or computational techniques (Given, 2008). Most of these methods exploit machine learning classification techniques, including e.g., thresholds, logistic regression, random forest, unsupervised clustering (Michie et al., 1994; Richards and Jia, 2006). A "qualitative" mapping method obtains information on the presence (or absence) of landslides through an empirical and heuristic visual interpretation of EO imagery – also called "visual investigation", "visual analysis", "visual photograph data interpretation". When applied to map validation, the

terms “qualitative” and “quantitative” refer to methods and techniques that exploit the expert-based recognition of landslides, and mathematical and statistical procedures and associated results, respectively. A “study area” is a geographical area where a landslide event was investigated. Multiple articles may have investigated the same study area using the same or different approaches. A “case study” is a specific landslide event investigated using a single approach and discussed in a single article.

3. Construction of the literature database

To construct the literature database, we first considered all the relevant articles already known to us. Next, we searched peer-reviewed articles in the Core Collection of the “Web of Science” online platform using keywords and the Boolean search criteria AND, OR, NOT, SAME, NEAR applied to the “title”, “abstract”, and “keywords” of the publications. Keywords we used were “map / mapping”, “detect / detection”, “recognition”, “identification”, “SAR”, “amplitude”, “intensity”, “backscatter / backscattering”, “coherence”, and “InSAR / DInSAR”, in combination with landslide descriptive terms defined by Cruden and Varnes (1996) and Hungr et al. (2014), including “landslide”, “slope instability”, “landslip”, “rock fall”, “slump”, “slide”, “earth flow”, and “debris flow”. For our search, we included terms like “recognition” and “identification” used in the literature as a synonyms for “detection”.

We checked the list of references in all the selected articles, and we repeated the search multiple times from April 2019 to November 2020 to obtain a preliminary list of 126 articles. We examined thoroughly the articles in the preliminary list, and we excluded 72 of them (57%) because they were not relevant, mostly because they dealt with the evolution of single landslides (Hungr et al., 2014). Our final literature database lists 54 articles published between January 1995 and November 2020 in 26 peer-reviewed journals, including 17 remote sensing journals, six earth-science journals, and three multi-disciplinary journals (Fig. 1A). We consider the collection representative of the scientific literature on the use of SAR imagery for landslide detection and mapping in the 26-year period 1995–2020. A first conclusion we draw is that, despite the recognised need for landslide maps (Guzzetti et al., 2012), and the alleged capability of SAR imagery to detect and map landslides (Guzzetti et al., 2012; Scaioni et al., 2014; Casagli et al., 2016), the literature on the exploitation of SAR imagery for landslide event detection and mapping remains limited. Inspection of Fig. 1B reveals a constant increase in the number of published articles per year, with the rate of publications increased first in 2012, and more significantly from 2018.

To characterise the individual studies in our collection, we searched for information of five categories, namely: (i) the characteristics of the study areas, including the extent of the areas and their geological, geomorphological, land cover, climate, and seismicity settings; (ii) the characteristics of the landslide event, including the number, type, and size of the triggered landslides, and the main landslide trigger (e.g., intense or prolonged rainfall, earthquake); (iii) the image pre-processing approaches; (iv) the image classification methods used in the studies; and (v) additional ancillary data. This information was not available for all the studies. Two recent papers (Mondini et al., 2019; Burrows et al., 2020) examined multiple case studies, influencing the statistics of the case studies. We found that 70% of the studies provided information on the event landslide trigger, but only 26% gave information on the extent of the study area. Considering the landslides, 28% of the studies reported information on the exact or approximate number of the detected or mapped landslides, 48% gave information on the type, or types of landslides, and only 30% of the studies provided information on the size (area, volume) of the landslides. Overall, we consider the information on the landslide characteristics given in the articles limited, and we recommend to provide more, and more accurate, landslide information when presenting the results of landslide detection and mapping studies.

We also found that 78% of the studies provided information on the image pre-processing approaches. We attribute this high percentage to the fact that most of the articles (42, 77.7%) were published in remote sensing journals (Fig. 1A). We further found that only 40% of the studies gave information on the land cover type, important for many EO remote sensing applications. Only one article provided information on the geological, morphological, climate, and seismicity settings. Ultimately, we found that 68% of the articles provided information on the validation of the landslide detection and mapping results. The figure is similar to

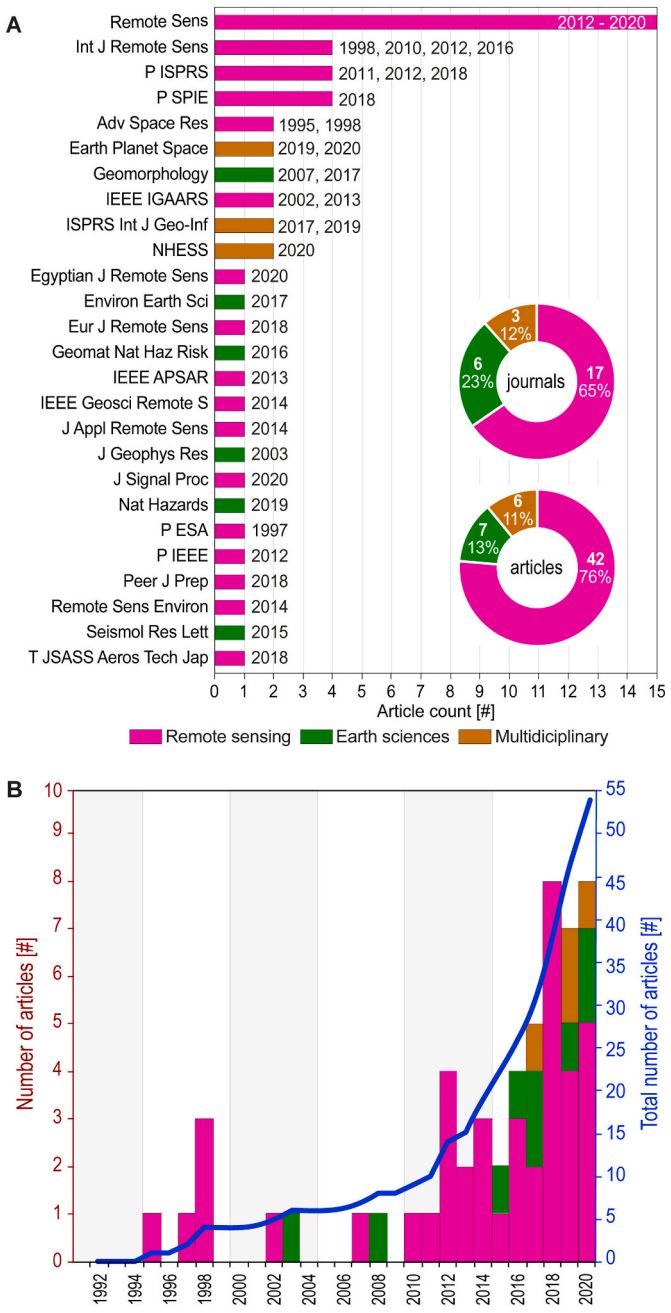

Fig. 1. Articles and journals in the literature database. (A) The 26 journals represented in the literature database. Horizontal bars show number of articles in each journal. Numbers on the side of the bars show the year of publication of the articles. Pie charts show number and percentage of journals and articles in the three journal categories. (B) Temporal distribution of the articles in the literature database. Vertical bars show number of published articles per year (left y-axis). Blue line shows cumulated number of articles per year (right y-axis). Colour shows journal category: pink, remote sensing; green, Earth sciences; brown, multi-disciplinary. (For interpretation of the references to colour in this figure legend, the reader is referred to the web version of this article.)

the percentage of statistically-based landslide susceptibility assessment studies that accomplished model validation (Reichenbach et al., 2018).

Fig. 2 portrays the geographical distribution of the study areas in the literature database.

4. Background on Synthetic Aperture Radar

Airborne and space-borne radar systems are active microwave sensors with an onboard, side looking antenna that illuminates the ground surface (i.e., the "target") with single band pulses of electromagnetic radiation. Their common operational range of interest for this work includes the central frequencies of ~ 9.6 *GHz*, ~ 5.4 *GHz*, or ~ 1.3 *GHz*, named X-band, C-band, and L-band, respectively (IEEE, 2020) (Table 1). The antenna receives the returning signal (i.e., the "echo"), and measures the strength of the echo and the time it takes the signal to return to the antenna. The strength of the echo depends on the properties of the scattering ground surface in relation to the radiation frequency (e.g., the dielectric constant, the terrain roughness), the distance between the antenna and the ground, and the satellite view angle (Fig. 3), and it is recorded in the "amplitude" of the electromagnetic wave. The echo return time depends on the relative distance between the antenna and the illuminated object (the "scatterer") on the ground surface and it is recorded in the "phase" of the electromagnetic wave (Meyer, 2019).

The side looking configuration of SAR systems (Fig. 3) introduces a number of peculiarities. The pixel coordinates in sensor geometry are expressed in terms of distance from the radar track ("range direction" or "across-track"), and of the sensor flying direction ("azimuth direction" or "along-track"). The "slant range" measures the distance between the radar antenna and the portion of the illuminated ground represented by the pixel, inferred from the time delay. The "azimuth" is perpendicular to the slant range direction, and measures the along-track distance between the antenna and the scatterer (Fig. 3).

The spatial resolution of the SAR images varies along the range direction – decreasing with the increase of the distance between the illuminated area and the sensor – and is constant and independent from the range along the azimuth direction (Fig. 3). Both resolutions depend on multiple factors, including the sampling frequency, the orbital parameters, and the acquisition mode (Oliver and Quegan, 2004). Image preprocessing procedures (e.g., interpolation, filtering, multi-looking) can also change the resolution of SAR images. Hence, a comparison with optical products in terms of pixel size or ground sampling distance (GSD) is meaningful only when a SAR image is projected to ground coordinates ("geocoding").

The side looking geometry of SAR sensors introduces geometric distortions in the images, including "foreshortening", "layovering", and "shadows", in particular in mountainous or hilly terrain (Fig. 3B). Foreshortening occurs when illuminated slopes are mapped with a compressed scale relative to its appearance. A layover is an extreme form of foreshortening where the top of a backscattering object (e.g., a mountain top) is recorded closer to the radar (in slant range) than are the lower parts of the object (e.g., the base of the slope). Shadows are caused by the lack of radar illumination (Fig. 3B) (European Space Agency, 2020b; Meyer, 2019). Geometric distortions depend on the satellite orbit parameters (e.g., ascending or descending), the satellite configuration (e.g., side of look), and the acquisition parameters (e.g., look angle, Θ), and their presence remains a problem for landslide

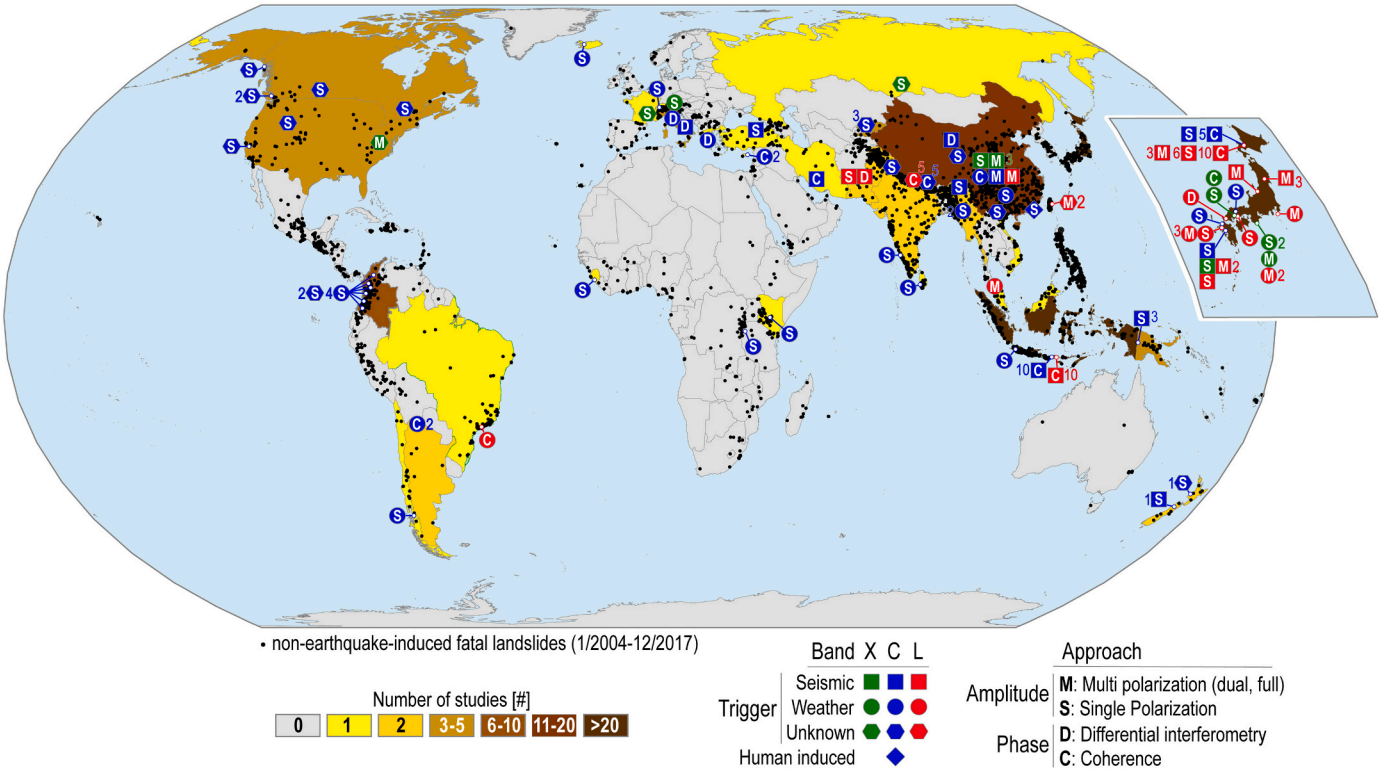

Fig. 2. Geographical distribution of 70 study areas in the literature database. Countries coloured based on the number of studies, in seven classes. Symbols show the approximate location of the study areas. Colour of symbol shows SAR band: green, X-band; blue, C-band; red, L-band. Shape of symbol shows main landslide trigger: square, seismic; circle, weather; hexagon, unknown trigger; diamond, human induced slope failures. Capital letter in the symbol shows the adopted approach: C, coherence; D, differential interferometry (DInSAR); M, multi (dual, full) polarisation; S, single polarisation. Number to the side of the symbol shows number of case studies. Inset map on the right side of the main map portrays enlargement for Japan. Small black dots show non-earthquake-induced fatal landslides between 2004 and 2016 inventoried by Froude and Petley (2018) and updated recently to cover the period from January 2004 to December 2017 (Froude and Petley, personal comm. 2019). Map uses the Equal Earth map projection (EPSG:8857). (For interpretation of the references to colour in this figure legend, the reader is referred to the web version of this article.)

Table 1
Past and present SAR satellites and constellations useful for landslide detection and mapping, listed from oldest to most recent.

Satellite	N.	Band	Ch	Mode - Resolution	Revisit	Period	Oper.	Used
ERS-1	1	C, 5.3 GHz, 5.6 cm	S	(IM) 30a×26r m	35 d	7/1991–4/2001	ESA	Y
JERS-1	1	L, 1.2 GHz, 23.5 cm	S	18 m (ML)	44 d	11/1992–11/1998	*	Y
ERS-2	1	C, 5.3 GHz, 5.6 cm	S	(IM) 30a×26r m	35 d	4/1995–9/2011	ESA	Y
Radarsat	1	C, 5.3 GHz, 5.6 cm	S	(SM) 28a×25r m	24 d	11/1995–3/2013	CSA	Y
Envisat ASAR	1	C, 5.3 GHz, 5.6 cm	S	(IM) 30a ×30r m	35 d	3/2002–4/2012	ESA	Y
ALOS	1	L, 1.2 GHz, 23.6 cm	S	(SM) 10 m (ML)	46 d	1/2006–5/2011	JAXA	Y
COSMO-SkyMed	4	X, 9.6 GHz, 3.1 cm	D	(SM) 5 m (ML)	16 d	6/2007–	ASI	Y
TerraSAR-X	2	X, 9.6 GHz, 3.1 cm	F	(SM) 3.3a×1.70r m	11 d	6/2007–	DLR	Y
Radarsat-2	1	C, 5.4 GHz, 5.5 cm	F	(SM) 28a×25r m	24 d	12/2007–	MDA	Y
Risat-1	1	C, 5.3 GHz, 5.6 cm	F	(FRS-2) 3a×4r m	25 d	4/2013–	ISRO	N
Kompsat-5	1	X, 9.6 GHz, 3.2 cm	D	(ST) 3 m (ML)	28 d	3/2014–	KARI	N
Sentinel-1	2	C, 5.4 GHz, 5.5 cm	D	(IW) 14.1a×2.3r m	12 d	3/2014–	ESA	Y
ALOS-2	1	L, 1.2 GHz, 22.9 cm	F	(SM) 3 m (ML)	14 d	5/2014–	JAXA	Y
PAZ	1	X, 9.6 GHz, 3.1 cm	D	(SM) 3 m (ML)	11 d	4/2018–	Hisdesat	N
Saocom-1	2	L, 1.2 GHz, 23.5 cm	D	(SB) 3 m (ML)	6 d	10/2018–	CONAE	N
Radarsat Cons.	3	C, 5.4 GHz, 5.5 cm	F	(MR) 16 m (ML)	12 d	4/2019–	CSA	N
Capella	36	X, 9.6 GHz, 3.1 cm	S	min 0.5 m	nyd	9/2020–	Capella	

Legend: N.; number of satellites in a constellation. For Capella, the deployment of 36 satellites is planned for 2021; one operational satellite and one test satellite are currently in orbit. Band; X, C, L, frequency (GHz), wavelength (cm). Ch; channels: S, single polarisation, D, dual polarisation, F, full polarisation. Resolution (m); a, azimuth; r, range; most commonly used resolution is listed. Revisit; revisit cycle, in days (d). For constellations, the revisit cycle can be obtained dividing the listed revisit cycle by the number of satellites in the constellation (N). nyd, not yet defined. Period; period during which the satellite or constellation was/is operational. Oper., satellite operator; *, JERS-1 was jointly operated by NASDA, MITI, and STA. Used; imagery used (Y) or not used (N) for landslide detection and mapping in the literature database. All the listed satellites allow for multiple products configurations. For used sensors (Y), we list the most comm acquisition modes i.e., SM, "StripMap"; IW, "Interferometric Wide Swath"; IM, "Image Mode", and the related spatial resolutions. We add ML when the resolution is given after "Multilooking" filtering. For sensors that were not used (N), we list modes similar to the modes used in similar missions, or modes of potential interest based on swath and spatial resolution i.e., ST, Standard mode; SB, Single beam.

studies that exploit SAR imagery. An additional limitation of the side looking geometry of SAR systems is related to the fact that along-track displacements cannot be measured. Hence, ground movements along about the NS direction can hardly be detected.

5. Literature review

5.1. SAR amplitude

In the radar sensors of interest for landslide detection and mapping (Table 1), the amplitude of the transmitted and the received radiation can have a horizontal (H) or a vertical (*V*) geometrical orientation, or "polarisation". For most of the sensors, the amplitude is acquired in single (HH or VV) polarisation (SP) or in dual (HH + HV, or VV + VH) polarisation (DP). Fully-polarimetric systems acquire all the possible combinations of polarised backscatter i.e., HH, HV, VH, and VV (FP) (Czuchlewski et al., 2003). In the following, we first address works that performed a multi-polarimetric (full- or dual-polarimetric) analysis. Next, we present articles that exploited single-polarimetric analyses.

5.1.1. Multi-polarisation

From a theoretical perspective, where a landslide removes the vegetation that covers a slope, the terrain microwave scattering properties change from the adjacent areas that were not affected by the landslide, and where the vegetation has remained unchanged. As an example, a forested slope has a typical "volume" or "diffuse" backscatter, whereas an area where a landslide has removed the forest (i.e., the vegetation) cover exhibits a backscatter signal typical of a rough, bare surface (Yamaguchi, 2012). In the case of landslide failure detection and mapping, the single scattering components are obtained mainly through decompositions of matrices describing the overall scattering behaviour of the targets, namely, the Sinclair scattering matrix S for pure scatterers, or the covariance ($[C_2]$, $[C_3]$) or coherence ($[T_2]$, $[T_3]$) matrixes for distributed scatters, with subscripts $_2$ and $_3$ referring to dual and full polarisation systems, respectively, and whose elements are proportional to the backscattering coefficients for the different channels (i.e., σ_{xy} where subscripts $_x$ and $_y$ represent one of the possible polarisation configurations of the sent and the return wave, respectively) (Cloude, 1992; van Zyl, 1993; Cloude and Pottier, 1996; Praks et al., 2009; European Space Agency, 2020d). The decompositions allow to obtain parameters closely related to the physics of the various scattering mechanisms, including e.g., Entropy H, the "weighted average scattering" $\overline{\alpha}$, Anisotropy $\mathscr{A}$, and Pedestal height P_H (Cloude and Pottier, 1996; European Space Agency, 2020d). For visualisation purposes, the single bands can be combined to form Red, Green, Blue (RGB) or Hue, Saturation, Intensity (HSI) colour space composites, together with other indices, including e.g., (i) the direct analysis of correlations of HH-VV, HH-HV, HV-VH; (ii) the power ratios of HH/HV, HH/VV, VV/HV; and (iii) the Radar Vegetation Index, *RVI* that increases with the vegetation cover (Kim and van Zyl, 2001; Kim and Zyl, 2009).

In the literature database, five studies adopted qualitative methods and 15 studies used quantitative methods to classify multi-polarimetric, satellite or airborne, images and derivative products, including two studies that used dual-polarimetric images (Plank et al., 2016).

Rodriguez et al. (2002) were the first to use a hybrid classification scheme to identify polarimetric parameters for the visual detection of landslides on SAR imagery. Using L-band airborne FP AIRSAR images (NASA Jet Propulsion Laboratory, 2020a) taken about one year after the 21 September 1999, M_w 7.7, Chi Chi earthquake in Central Taiwan, the authors were able to detect and map visually the $\approx 1.25 \times 10^8 m^3$ Tsaoling rockslide (Hung et al., 2002; Chigira et al., 2003; Chen et al., 2006). In the landslide area, the σ_{vv}, $\sigma_{hv}\sigma_{hh}$ backscattering coefficients (Oliver and Quegan, 2004) proved sensitive to the scattering properties of the bare, rocky ground surface, whereas Entropy (H), Pedestral height (P_H), and the Radar Vegetation Index (*RVI*) characterised well the backscatter properties of the undisturbed forest surrounding the landslide. The same landslide was studied by Czuchlewski et al. (2003) who performed an empirical analysis of the backscattering indices H, P_H, and $\mathscr{A}$, obtained from the same L-band airborne FP AIRSAR images. Contrast between the surface scatter inside the landslide depletion and depositional areas, and the diffuse scatter of the untouched forest outside the landslide, allowed for the visual recognition and mapping of the large rockslide. Czuchlewski et al. (2003) pointed out that in landscapes characterised by a complex land cover, and where the landslide backscatter signature is not unique, the proposed method may result in misclassifications.

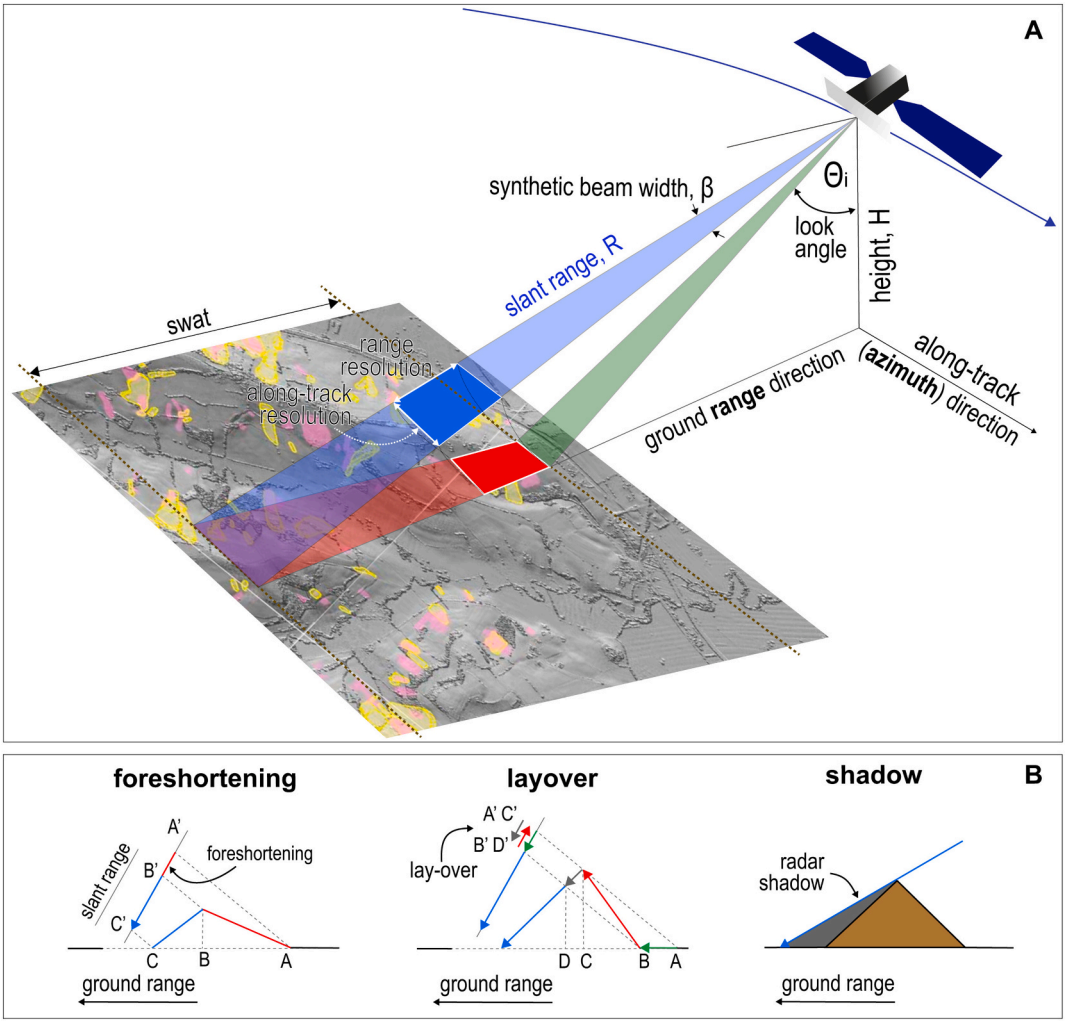

Fig. 3. SAR geometry. (A) Exemplification of the side looking geometry of a typical SAR system. The example is for a right-looking satellite flying along a descending orbit. Coloured polygons on the shaded relief image exemplify landslides of different types. (B) Geometric distortions and shadows typical of a SAR system. Modified after Meyer (2019). The proportions of objects, distances, and angles are exaggerated, and are not in scale.

Watanabe et al. (2012) used pre-event and post-event L-band FP ALOS imagery with 30 $m \times 30$ m ground resolution (Table 1) to map eleven of the thirteen landslides triggered in the Dozow-sawa area, NE Japan, by the 14 June 2008, 6.9 M_w, Iwate-Miyagi Nairuku earthquake. For the purpose, they adopted the semi-empirical model proposed by Yisok (2004) that combines backscattering coefficients with terrain surface properties (i.e., roughness and dielectric constant) to reduce the number of landslide false positives in some land cover classes, including pasture, grassland with sparse trees, and lakes. The same landslide event was investigated by Yonezawa et al. (2012) who used a Freeman-Durden decomposition (Freeman and Durden, 1993; Freeman and Durden, 1998) of the same pre-event and post-event L-band FP ALOS images. The decomposition was based on a fitting of a physically-based, three-component scattering mechanism model, including the canopy scatter, the Bragg surface scatter, and the double-bounce scattering mechanism. The authors attributed high values of surface backscatter to the presence of newly formed, seismically induced landslides. In parallel, an unsupervised classification that used the $H-\overline{\alpha}$ plane of the eigenvector decomposition (Cloude, 1992; European Space Agency, 2020d) allowed the authors to discriminate landslide areas from lakes and areas covered by snow.

Konishi and Suga (2018b) used three polarimetric indices obtained by processing pre-event and post-event L-band FP ALOS-2 imagery to detect and map landslides triggered by the 6 April 2016, 7.0 M_w, Kumamoto earthquake, Kyoshu, Southern Japan. Adopting a change detection approach, the authors trained a random forest classifier using separately $\overline{\alpha}$, H, and polarimetric correlation coefficients (European Space Agency, 2020d) between the HH and VV channels in bare soil (considered to be landslides), forest, grass and crop, paddy, and urban (built-up) areas. Overall accuracy (OA) was high for the three classifications (0.86, 0.85, and 0.73, respectively), confirming the potential of the technique for landslide detection and mapping.

Park and Lee (2019) also used pre-event and post-event L-band FP ALOS-2 images and polarimetric eigenvector decomposition (Cloude, 1992; European Space Agency, 2020d), to detect and map landslides triggered by the same Kumamoto earthquake in Kyoshu island, Japan. Quad-polarisation parameters capturing signal depolarisation properties revealed noticeable landslide-induced temporal changes for all local incidence angles (the angle between the satellite and the normal to the surface of the target cell), allowing for an automatic threshold-based detection of the seismically-induced landslides. The last two studies suggest that landslide detection from L-band images are useful when pre-event and post-event imagery is available.

To map 22 landslides caused by intense rainfall brought by typhoon Talas in August and September 2011 in a forested mountain region of Japan, Shibayama et al. (2015) used L-band FP ALOS-2 and FP L-band airborne Pi-SAR-L2 images (Table 1), and found that the backscattering in the landslide areas – and hence, the ability to discriminate the

landslides from the forested terrain – decreased with the increase of the local incidence angle. To improve the landslide detection accuracy, the authors used multiple thresholds on the backscattering based on the local incidence angle. The same landslide event was studied before by Shimada et al. (2014) who used only the airborne FP Pi-SAR-L2 images. Interestingly, in this earlier study a dependance of the backscattering on the image incidence angle was not found, probably because of the very different image acquisition angles. A sensitivity to the observational direction of the Pi-SAR-L2 images was also found by Watanabe et al. (2016) who detected and mapped rainfall-induced landslides caused by Typhoon Wipha in October 2013, in the Izu Oshima Island, Japan (Yang et al., 2015). The authors found that the adoption of a modelled backscattering coefficient σ_0 (Ulaby et al., 1982), H, $\overline{\alpha}$, $\mathscr{A}$ (Cloude, 1992; European Space Agency, 2020d), and coherence between HH and VV channels (Ferretti et al., 2007; Richards, 2009b), improved discrimination between landslide areas and forested areas when using small image incidence angles.

In a recent work, Ohki et al. (2020) repeated the mapping experiments executed previously by Watanabe et al. (2012), Shimada et al. (2014), Shibayama et al. (2015), Watanabe et al. (2016), and partially by Park and Lee (2019), and used 3 m × 3 m resolution, FP ALOS-2 images to map landslides triggered by heavy rainfall on 5–6 July 2017, in Kyushu, Japan (Ochiai et al., 2017), and by the 6 September 2018, 6.6 M_w, Hokkaido Eastern Iburi earthquake, Northern Japan. The authors proposed empirical thresholds for the Pauli components of the coherency matrix [T_3](Cloude and Pottier, 1996; European Space Agency, 2020d), and found that their mapping results depended on the site and the local image incident angle, with Cohen's k (Cohen, 1960) in the range from 0.37 to 0.66.

Based on the results of these studies, we conclude that the image local incidence angle i.e., the angle between the radar line-of-sight (LOS) and the normal vector to the slope surface, affects the sensitivity of L-band imagery to the surface and volume backscatter and, hence, to the possibility to detect and map landslides.

Shorter wavelength, X-band and C-band imagery was also used in multi-polarisation configurations for landslide detection and mapping, often in combination with machine learning classification methods. Li et al. (2014a, 2014b) used imagery taken by an undefined Chinese high-resolution airborne FP X-band SAR system to detect and map large landslides caused by the 12 May 2008, 7.9 M_w, Wenchuan (or Sichuan) earthquake, South-central China. The authors tested various decompositions, and found that the Yamaguchi four component decomposition (Yamaguchi, 2012) – which adds the Helix to the three standard components – performed better where the reflection symmetry condition, HV = VH did not hold, and that the Cloude decomposition (H-$\overline{\alpha}$) (Cloude, 1992; European Space Agency, 2020d) revealed complicated scattering mechanisms in the landslide areas, which the authors attributed to the landslide surface becoming relatively "rough" at the X-band scale (≈ 3.1 cm). The authors classified the landslide areas using a supervised Wishart classifier (Lee et al., 1994b), and verified a posteriori that landslide areas had higher Polarimetric Scattering Similarity (*PSS*) parameters (Jian Yang et al., 2001; Chen et al., 2018) compared to the surrounding forested terrain, indicating stronger surface scattering and double-bounce scattering components. The latter information proved useful to tune a *PSS* threshold-based classifier. The authors also studied the Pauli's coherent decomposition of the Sinclair scattering matrix S (Cloude and Pottier, 1996; European Space Agency, 2020d), and used its three components to fill an HSI colour space (Haydn et al., 1982; Carper, 1990) in which the H channel was sensitive to both landslide areas and noise. Ultimately, a k-means unsupervised classifier (Jin and Han, 2010) was used to discriminate between the different terrain classes, including the landslide areas (Li et al., 2014a, 2014b).

A different attempt to exploit X-band DP TerraSAR-X imagery was conducted by Plank et al. (2016) who identified changes in the vegetation cover caused by two landslides, one in Charleston, West Virginia, USA, and another near Bolshaya Talda, Kemerovo Oblast, Russia. In the dual-polarisation [C_2] eigenvector decomposition (Lee and Pottier, 2017), both landslides showed low dual-polarimetric H in post-event images in areas where before the landslides the ground was covered by vegetation. Use of the dual-polarimetric $\overline{\alpha}$ proved critical, due to the heterogeneity of the landslide material.

Luo et al. (2016) used C-band FP Radarsat-2 (Table 1) images to detect and map landslides triggered by the 12 May 2008, 7.9 M_w, Wenchuan earthquake, China. The study revealed the efficacy of the polarimetric eigenvector (Cloude and Pottier, 1996; European Space Agency, 2020d) and the target decompositions (Freeman and Durden, 1998) to detect and map the seismically-induced landslides. The components of the two polarimetric decompositions were first clustered, the clusters were grouped into nine land-cover classes using a Wishart classifier (Lee et al., 1994b), and the landslide class was assigned to the class segments showing a dominant surface scattering component. The authors acknowledged the high false positive rate (FPR) of their classification, which jeopardised the widespread application of the proposed method.

Ultimately, in a landslide susceptibility modelling exercise, Tien Bui et al. (2018) used FP AIRSAR L-band and P-band imagery, and SP AIRSAR, C-band imagery, in addition to a re-sampled 10 m × 10 m resolution DEM, to confirm the presence of 92 landslides in the Cameron highlands, central Malaysia, detected and mapped interpreting visually very-high-resolution WorldView-1 multispectral satellite imagery and digital aerial photographs, aided by field surveys. The authors concluded that the spatial resolution of the SAR images was insufficient to separate the different land cover types, but details were not given in the article.

5.1.2. Single-polarisation

For single polarisation (SP) imagery, the interaction between matter and radiation is recorded in the amplitude of the return wave and in its derivative products, including intensity I, and the backscattering coefficients (e.g., σ_0, β_0, or γ_0) (Oliver and Quegan, 2004; El-Darymli et al., 2014), whose values depend on the combination of land cover, including landslide, surface dielectric properties, shape, and roughness, and on system parameters (Oliver and Quegan, 2004).

In the literature database, 26 articles reported results of the use of single polarimetric, satellite or airborne, SAR imagery.

In his pioneering work Singhroy (1995) used C-band images taken by the Canada Centre for Remote Sensing (CCRS) C-HH airborne SAR at a resolution of 6 m × 6 m, to improve the quality of a landslide inventory for a part of the Fraser River valley, British Columbia, Canada. Visual interpretation of changes in tones in the SAR images allowed for the recognition of rock slumps and block slides (Hungr et al., 2014), which had not been recognised before. For visualisation purposes, Singhroy (1995) used an HSI transformation (Haydn et al., 1982; Carper, 1990) to combine the SAR images projected into geographical coordinates with a re-sampled, 6 m × 6 m, multi-spectral Landsat Thematic Mapper (TM) image (NASA, 2020) projected onto a 1:20,000 topographic base map. The Landsat TM image provided visual information useful for landslide mapping, including the presence of sparse or dense vegetation, of thin soil with exposed rocks, and of clear cut areas.

Vargas Cuervo (1997) described a similar experiment in an area of the Easter Cordillera, Colombia, where the use of optical images to detect and map landslides was hampered by a persistent cloud cover. The author interpreted visually a C-band ERS-1 amplitude image to identify seven landslides in a list of 458 obtained through field mapping and the visual interpretation of an optical stereoscopic pair of SPOT and Landsat TM images. In the SAR amplitude image, landslide deposits exhibited higher backscattering coefficients (shown by bright grey tones) than the unaffected areas (shown by dark grey tones), due to higher terrain roughness.

Singhroy et al. (1998) performed a similar experiment in the Saskatchewan, Fraser, and Ottawa valleys study areas, in Canada. For the first two experiments, he used C-band Radarsat images, and for the third

experiment images taken by the Canada Centre for Remote Sensing (CCRS) C-HH airborne SAR (Table 1). A result of the study was a qualitative analysis on the impact of different Radarsat viewing geometries in the Fraser valley where the Radarsat Extended High beam mode, EH6 (57–59), proved more effective in recognising landslide features than the Standard beam mode, S1, on the steep slopes of the valley.

Chorowicz et al. (1998) used a C-band ERS-1 (12.5 m × 12.5 m pixel) and an L-band JERS-1 (18 m × 18 m pixel) images (Table 1), together with a coarse resolution, 100 m × 100 m DEM, to prepare two simulated image stereo-pairs. Visual interpretation of the pseudo-stereoscopic images allowed for the recognition of small "geomorphic features" in the landslide areas, and the identification and mapping of fourteen landslides in Paz de Rio, Colombia. Details on the type and size of the landslides were not given in the article, but inspection of Fig. 4 in the article indicates that the largest landslide was about 600 m^2. The conclusion of the study was that variations in the backscatter inside and outside the landslides due to different terrain roughness, were not sufficiently large for the visual recognition of all the landslides, and that only the largest landslides could be mapped, due to the limited ground resolution of the imagery.

After these early works, there is a gap of about a decade in the literature database before the next article describing the visual interpretation of SAR images to detect and map landslides. While mapping the disruption caused by the 12 May 2008, 7.9 M_w, Wenchuan earthquake in Beichuan, China, Balz and Liao (2010) recognised and mapped the seismically induced landslides using post-event X-band, Stripmap TerraSAR-X intensity images with a resolution of about 3 m × 3 m (Table 1). Visual recognition of the landslides was possible due to the different backscatter of the landslide areas, compared to the nearby built-up areas. In the images, the presence of the landslides was revealed by abrupt tonal changes in the landslide scarp (source) and toe (depositional) areas.

In a later work, Xue et al. (2011) discussed the use of SAR σ_0, in combination with optical imagery, to identify landslide-related geological features and faults. Where the landslide surface was bare, and alluvial Quaternary deposits cropped out, the radar echo was affected mainly by terrain roughness, and by the water content and structure of the shallow soil. Where the soil water content was high, and the terrain surface was rough, the σ_0 image tone appeared light grey, revealing the presence of the landslide, whereas where the terrain was stable (i.e., free of recent landslides) and vegetated, the image tone was dark grey.

The synergic use of optical and SAR imagery was further explored by Mwaniki et al. (2017) who tested the possibility of using C-band Sentinel-1 imagery to increase edge identification when "fused" to Landsat 8 Operational Land Imager (OLI) images, to recognise landslides in Kenya. The authors filtered the SAR data using the (Frost et al., 1982) and (Lee, 1986; Lee et al., 1994a) filters to outline the image textural information.

A few authors attempted to use indices and measures of backscattering changes for landslide detection and mapping. Furuta and Tomiyama (2008) were able to detect and map a few seismically-induced landslides triggered by the 29 October 2008, M_w 6.4, Zirat earthquake, in Western Pakistan, using the normalised difference between pre-event and post-event scatter (NDSI) L-band ALOS σ_0 imagery. However, the authors failed to recognise a large, seismically-induced rock slide. Spatial variations in the NDSI changes were also used by Konishi and Suga (2017) who mapped large debris flows caused by a high-intensity rainfall event on 20 August 2014 in Hiroshima, Central Japan (Wang et al., 2015) exploiting changes in the backscattering properties of the topographic surface caused by sediments and driftwood mobilised by the large debris flows. Tessari et al. (2017) interpreted visually amplitude changes in X-band COSMO-SkyMed images to detect a 60 m wide by 400 m long roto-translational landslide triggered by heavy rainfall in November 2017, in the Val Maso municipality, NE Italy.

To map landslides caused by record-breaking rainfall brought by Typhoon Talas in the Kii Peninsula, south-central Japan, beginning on 30 August 2011, Suga and Konishi (2012) and Konishi and Suga (2018a) investigated the potential of thresholded backscattering coefficient difference and intensity correlation measures, obtained from pre-event and post-event X-band, COSMO-SkyMed images multi-looked at a ground resolution of 5 m × 5 m. In particular, Konishi and Suga (2018a) showed that the intensity correlation measures obtained by applying the Lee (1981) and Frost et al. (1982) filters with different-sized moving kernels (Matsuoka and Yamazaki, 2004), outperformed the backscattering coefficient. Results were compared to a landslide inventory prepared exploiting a 0.7 m × 0.7 m resolution EROS-B optical image. Large kernels of 19 × 19 pixels (9025 m^2) for the backscattering coefficient difference, and of 25 × 25 pixels (15,625 m^2) for the intensity correlation, proved to be the best options to detect and map landslides up to $A_L \approx 3.7 \times 10^5 m^2$.

Liu et al. (2018) also attempted to use changes of the intensity measured for C-band Sentinel-1 images to visually detect and map three new landslides occurred on 1 October 2017 in the loess area of Dangchuan, Southern China, for a total volume of mobilised debris of $V_L = 33.9 \times 10^4 m^3$. However, given the ground resolution of the satellite imagery (16 m × 16 m), and the relatively small size of the landslides (≈ 140 m × 270 m), mapping of the landslides was not accurate.

Mondini et al. (2019) were the first to use changes in the β_0 backscattering coefficient, also called radar brightness coefficient, between pre-event and post-event C-band Sentinel-1 images for the systematic detection and mapping of rapid moving landslides. For a set of 32 landslides of very different sizes ($0.01 \times 10^6 m^2 \leq A_L \leq 21.0 \times 10^6 m^2$) selected randomly in different geological, morphological, and environmental settings globally, a team of geomorphologists trained in the visual interpretation of aerial and satellite imagery for landslide mapping identified correctly 27 (84%) of the studied landslides, without any a-priori knowledge on the location, type, and size of the slope failures. In one case, they recognised the landslide only after knowing its exact location. In at least six cases, the landslide events included multiple slope failures. In three of the four unsuccessful cases, the geometry of the acquisition was considered responsible for the failed detection, and not the size or the type of the landslide.

Attempting to map landslides triggered by the 16 April 2016, 7.0 M_w, Kumamoto earthquake in Kyushu, Southern Japan, Uemoto et al. (2019) used airborne, X-band Pi-SAR2 images (Table 1) and combined thresholded changes in amplitude and terrain elevation in highly coherent pixels. A conclusion of the work was that, in forested areas, the occurrence of landslides (of unknown type and size) should result in (i) an increase of the amplitude and a decrease in the terrain elevation in the upper part of the landslide (i.e., the source or depletion area), (ii) a decrease of both amplitude and elevation in the main landslide deposit, and (iii) an increase of amplitude and elevation in the lower part of the landslide (i.e., in the deposition area). Absolute amplitude changes (resulting from changes in the surface backscatter) ≥ 5 Db, and changes in elevation ≥ 5 m were selected as thresholds to detect landslides. To measure the performance of their classifications, the authors confronted their new landslide map against an existing inventory prepared through the visual interpretation of stereoscopic areal photographs taken by the Japanese National Research Institute for Earth Science and Disaster Resilience (NIED). The two maps showed an inter-rater reliability of 0.60 and 0.46 in two separate areas, which was deemed moderate by the authors. Detection problems were related mainly to the inability to detect "small" (≈ 50 m × 50 m, $A_L = 2500\ m^2$) landslides, and the limited detectability of "medium size" (≈ 200 m × 500 m, $A_L = 1.0 \times 10^5 m^2$) landslides, mainly due to limits in the information of the terrain elevation changes.

The remaining articles in the literature database are recent, and address the problem of landslide recognition and mapping using machine learning techniques (Michie et al., 1994; Richards and Jia, 2006).

Mondini et al. (2017) measured the increase in the spatial autocorrelation (Griffith, 1987; Griffith and Chun, 2016) of a time series of

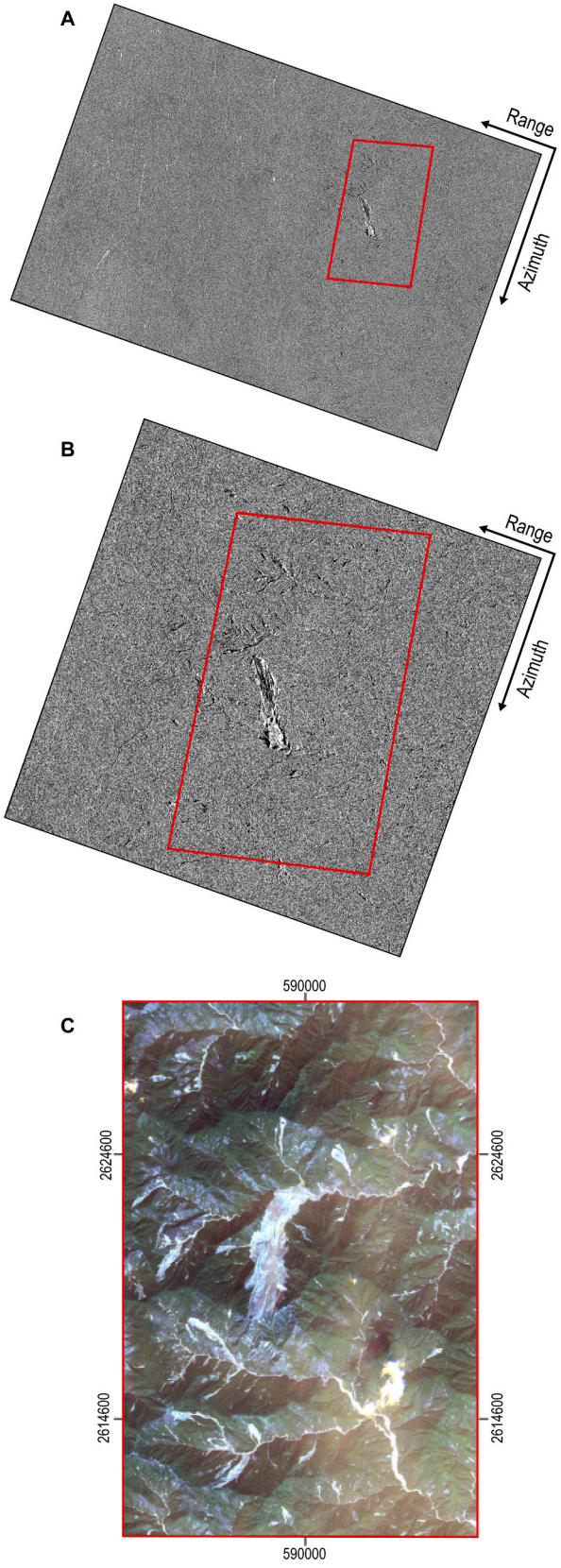

Fig. 4. Gigantic, rainfall-induced Tozang landslide, Myanmar, July 2015. (A) In radar azimuth–range coordinates, image shows natural logarithm of the ratio between post-event and pre-event β_0 radar brightness coefficient of VV polarised, C-band, ESA Sentinel-1 images taken along descending orbits. Red box shows approximate location of (C). (B) Enlargement of a portion of (A). "Salt & pepper" pattern reveals forested terrain where landslides did not occur. Clusters of similar black or white pixels show the Tozang landslide. (C) GeoEye image of the landslide area, in UTM WGS84 Zone 46 projected coordinates. Whitish areas are landslide areas. (For interpretation of the references to colour in this figure legend, the reader is referred to the web version of this article.)

measurements of changes of the β_0 radar brightness coefficient in C-band Sentinel-1 images, which the author attributed to a group of rainfall-induced landslides – mainly debris flows and slide flows – caused by heavy rainfall in Tozang, Myanmar, in July 2015. Landslides appeared as organised clusters within a matrix of speckles in an image showing the natural logarithm of the ratio between the post-event and the pre-event β_0 radar brightness coefficient images. An image optimal segmentation revealed that the size of the segments delineating the landslides was within the 95% percentile of the distribution of the areas of the segments.

A similar experiment was conducted by Esposito et al. (2018) who used a "mean shift" clustering method (Yizong Cheng, 1995; Comaniciu and Meer, 2002) to detect and map seismically-induced landslides triggered on 25 February 2018 by the 7.5 M_w Papua New Guinea earthquake in the Tagari River Valley of central Papua New Guinea. The experiment was extended recently by Esposito et al. (2020) who introduced an automatic selection of the segments containing landslides using statistics of the image changes. The algorithm was calibrated on landslides triggered by the 25 February 2018 earthquake, and then applied to detect landslides triggered by the 6 March 2018, 6.7 M_w earthquake in the same area. The work confirmed the potential of continuous SAR-based satellite monitoring of areas where seismically-induced landslides are frequent and abundant.

In a study of landslides triggered by the 6 September 2018, 6.6 M_w, Hokkaido Eastern Iburi earthquake, Northern Japan, Ge et al. (2019) compared the performances of the intensity difference and its absolute value, and the average of the absolute value over a moving window whose size was optimised through an AUC ROC analysis. The indices were used as covariates in a linear discriminant analysis, obtaining classification performance indices (i) for the correlation coefficient d_{abs2}, OA = 69.36%, recall = 87.76%, precision = 47.04%, and F1-score = 61.25%, and (ii) for the correlation coefficient difference, OA = 64.57%, recall = 81.68%, precision = 42.59%, and F1-score = 55.99%. The high recall indicated that the parameters were relevant to detect landslides, whereas the low precision was the result of many false positive non-landslide pixels, mainly in the vicinity of a landslide, where surface erosion was indistinguishable from landslide related changes, including vegetation tilt. The same landslide event was studied by Aimaiti et al. (2019) who used the same ALOS-2 images and the same performance indices to construct a decision tree based on geomorphological variables and "ad-hoc" thresholds. The study revealed that imagery taken along descending orbits performed better than the corresponding imagery taken along ascending orbits, because of the more favourable view point, and that the combined use of images taken along ascending and descending orbits performed better than the images taken from a single orbit, either ascending or descending.

Mabu et al. (2020) applied a Convolutional Neural Network (CNN) (Goodfellow et al., 2016) to a post-event L-band, 3 m × 3 m, ALOS-2 image (Table 1) to detect landslides triggered by heavy rainfall on 5–6 July 2017, in Kyushu, Japan (Ochiai et al., 2017). The trained CNN was capable of distinguishing between different size patches (from 8 × 8 to 128 × 128 pixels) of (probably) intensity values having (and not having) landslides, with a best accuracy of 0.67 and a best F-score of 0.70.

Ultimately, to map landslides triggered by the 6 September 2018, 6.6 M_w Hokkaido Eastern Iburi earthquake, Northern Japan, Jung and Yun (2020) used 3 m × 3 m, L-band HH ALOS-2 imagery, 16 × 16 multi-looked, and investigated the potential of bi-temporal, de-trended multi-temporal intensity and intensity-correlation change detection approaches in different land cover types. The bi-temporal intensity approach proved able to detect landslides in urban areas – due to the strong backscatter changes – and in forest terrain with relative low noise, but resulted in a high rate of false positives in croplands, where better performances were obtained by the intensity-correlation approach, which was closely related to the spatial distribution of the backscatter changes.

5.2. SAR phase

The electromagnetic radiation transmitted by a radar antenna reaches the ground and returns to the antenna in a time that depends on the two-way travel distance, 2R of the radiation (Fig. 3A). Under the approximation of a purely sinusoidal nature of the transmitted signal, the delay τ corresponds to a phase change ϕ i.e., the portion of the wavelength that measures the last fraction of the two-way travel distance, between the transmitted and the received signals (Ferretti et al., 2007; Richards, 2009a). The phase is measured recording twice the amplitude with an offset in phase of $\pi/2$ radians, in-phase and quadrature components (Ferretti et al., 2007; Richards, 2009a) and, by itself, it does not provide any useful information for landslide detection and mapping, because it cannot estimate the radiation backscattering. This is because individual scatterers within each image pixel are of much smaller size than the resolution of the SAR image to be uniformly distributed in the range $[-\pi,+\pi]$ ("speckle-like") (Oliver and Quegan, 2004). Further, a single image cannot be used to measure the distance between the antenna and the ground surface, because no geometric relationship exists between the phases of the different pixels.

5.2.1. Bi-temporal differential interferometry

Flying around the Earth along different orbits, a SAR sensor illuminates the same target on the ground surface from (slightly) different viewing angles during different passages. If the target area on the ground has moved between two satellite acquisitions (e.g., it was displaced by a landslide), with a component of the movement, along the satellite line of sight (LOS), the phase difference between the two images obtained by cross multiplying the "first scene" image with the complex conjugate of the "second scene" image (i.e., the "interferogram"), has a component related to the ground deformation (caused e.g., by a moving landslide) and other components that can be removed entirely using pre-processing techniques, removed partially using filters, or reduced using the same acquisition geometry and short revisit times (Rocca et al., 2000; Ferretti et al., 2007; Richards, 2009a). Changes in the interferometric phase between adjacent pixels in an interferogram allow to outline the spatial pattern of the surface deformation caused e.g., by a slope movement occurred between two successive images. For visualisation purposes, the deformation pattern is shown typically using a colour scheme that repeats every 2π cycles i.e., each colour "fringe" represents a (relative) displacement along the satellite LOS of about $\lambda/2$ (Ferretti et al., 2007; Richards, 2009a). To obtain the "true" deformation, one has to add to the wrapped phase the number of 2π-multiples, measuring the two way distance between the satellite and the ground target ("phase unwrapping") (Rocca et al., 2000; Ferretti et al., 2007; Richards, 2009a). Phase unwrapping can be important in the case of landslide scenarios, where usually sharp discontinuities are caused at the landslides borders (Manconi, 2019).

In the literature database, seven articles discuss the use of bi-temporal differential interferometry – or DInSAR – techniques to detect and map landslide failures.

Moro et al. (2007) used DInSAR to investigate the surface deformation caused by the 1997 Colfiorito seismic sequence (Basil et al., 1998) – one of the first earthquakes whose surface deformation was measured using DInSAR (Stramondo et al., 1999), and found local anomalies in the fringes obtained by processing a pair of C-band ERS-1/2 images taken one before and the other after three, moderate-magnitude, 5.6, 5.9, and 5.5 M_s earthquakes occurred on 26 September and 14 October 1997, in Central Italy. The local anomalies could not be explained by the fault displacement modelled adopting the (Okada, 1985) elastic formulation. A detailed photogeological analysis of the areas where the "anomalous" surface deformations were observed, revealed evidence of morphological elements that were associated to co-seismic (because they were evident in the interferometric fringes) activity of deep-seated gravitational slope deformations, or to (re-)activations of parts of large, deep-seated, dormant landslides. Interestingly, the slope deformations

detected by DInSAR were not observed by Bozzano et al. (1998) and by Esposito et al. (2000), who performed independent surveys of the earthquake-generated surface effects, including landslides, nor by Antonini et al. (2002), who used post-event aerial photography to prepare a geomorphological and landslide event inventory map of the area affected by the seismic sequence. Most probably, this was because the surface deformations were too small to be seen in the field or in the aerial photography.

Furuta and Tomiyama (2008) applied DInSAR to L-Band ALOS imagery taken before and after the 28 October 2008, 6.4 M_w Ziarat earthquake, Western Pakistan (Rafi et al., 2013) to detect and map a large, seismically induced rockslide. Visual inspection of a DInSAR-based surface displacement map allowed for the detection of the single, large landslide that generated displacements along the LOS smaller than 6 *cm*. Furuta and Sawada (2013) performed a similar experiment using L-Band polarimetric ALOS imagery to detect a rainfall induced landslide of unknown type (Furukawa et al., 2009; Nagano et al., 2011) occurred on 21 July 2009 in Hofu, Yamaguchi Prefecture, Southern Japan. The authors attributed the phase changes in the HH and HV ALOS imagery to changes in the position of the trees caused by the slope failure inside the landslide failure deposit, which allowed them to detect the landslide.

Working in the Molise Region of Central Italy, an area where landslides of different types and sizes are abundant (Trigila et al., 2010), Barra et al. (2016) tested the use of C-band Sentinel-1 imagery for regional-scale landslide mapping and monitoring. The authors integrated DInSAR-derived products with geological and geomorphological information in a GIS environment, to detect 62 active landslides, thirteen of which were "new" failures i.e., event landslides triggered by intense rainfall in the season from December 2014 to March 2015. The result led to the production of a seasonal landslide inventory, but the authors argued that manual processing, visual analysis of the imagery, and interpretation of the results, were cumbersome, and that further developments were necessary for the automatic recognition and mapping of landslides using DInSAR techniques to be effective, in their study area.

Kyriou and Nikolakopoulos (2018b) also used C-band Sentinel-1 imagery to generate interferograms, which they used to map ground deformations caused by a landslide triggered by rapid snow melting on 20 January 2016 in the Patras area, Greece. A similar result was obtained for the same landslide by Kyriou and Nikolakopoulos (2018a) who paired their DInSAR analysis with information obtained by processing optical, Sentinel-2 imagery. Lastly, Huang et al. (2017) proposed an "earthquake-derived landslide detecting method" capable of outlining high frequency areas (considered "landslides") by subtracting from an original interferogram obtained from two C-band Sentinel-1 images, a low pass filtered interferogram, followed by thresholding. The authors tested the method to map the ground deformation caused by the 21 January 2016, 5.9 M_w Menyuan earthquake, China. To adjust the phase change threshold, high frequency areas were visually classified as glaciers, landslides, or mudslides, exploiting very-high resolution optical imagery.

In addition to the previous articles, the works by Barboux et al. (2014) and García-Davalillo et al. (2014) provided valuable insight on the visual interpretation of DInSAR products for landslide detection and mapping. Barboux et al. (2014) used DInSAR to update existing regional-scale, geomorphological landslide inventory maps with daily, monthly, and yearly frequencies, and offered guidelines on how to interpret surface displacements in relation to factors that could induce a loss of coherence, including e.g., the imaging geometry, DEM errors, soil moisture, snow, atmosphere, and vegetation. The authors concluded that, where possible, landslides detected using DInSAR-derived products should be compared against field data ("ground truth"), pre-existing information (i.e., landslide inventories), and geodetic data. García-Davalillo et al. (2014) assessed the performances of DInSAR applied to L-band ALOS imagery to measure the degree of activity of very slow moving landslides (of unknown type) in the Valle de Tena, in the Spanish Pyrenees. The authors detected secondary – possibly event-triggered – landslides, apparently independent from the movement of the main, larger and pre-existing landslides.

Ultimately, we note that a number of authors have used multi-temporal DInSAR techniques (e.g., Ferretti et al., 2001; Berardino et al., 2002; Lanari et al., 2004; Ferretti et al., 2011) to measure the surface displacements caused by active, slow moving landslides. This information has been used to update geomorphological and multi-temporal landslide inventory maps, adding information on the degree of activity (UNESCO Working Party on World Landslide Inventory, 1993) in a period of single or multiple known landslides Bovenga et al., 2006; Farina et al., 2006; Lauknes et al., 2010; Notti et al., 2010; Righini et al., 2012; Bianchini et al., 2012; Ciampalini et al., 2012; Cigna et al., 2013; Bardi et al., 2014; Ciampalini et al., 2015; Raspini et al., 2015; Casagli et al., 2016; Michoud et al., 2016; Casagli et al., 2017a, 2017b; Solari et al., 2019; Lu et al., 2019a), to detect potential slope failures, confirmed or confuted by field checks (Raspini et al., 2018), and to model and anticipate the kinematics of known deep-seated, slow-moving, active landslides (Herrera Garcia et al., 2009; Del Ventisette et al., 2013; Herrera Garcia et al., 2013; Calò et al., 2014; Herrera Garcia et al., 2017). Overall, we maintain that these studies are different in scope from the articles considered in our work and, hence we have not presented them in detail here. Reviews covering extensively this type of studies are available e.g., in Ciampalini et al. (2015), Casagli et al. (2016), Casagli et al. (2017a), Casagli et al. (2017b), Solari et al. (2020).

5.2.2. Coherence

Atmospheric disturbances, temporal variations in the location and properties of the ground scatterers, slightly different image look angles, volume scattering due to e.g., the presence of a forest, and image pre-processing procedures can all introduce noise in the interferometric phase (Prati et al., 1990; Rodriguez and Martin, 1992; Rocca et al., 2000; Richards, 2009a), affecting the coherence γ between two SAR images, measured by combining phase and amplitude from the two complex SAR images (Ferretti et al., 2007; Richards, 2009a). Besides being used to assess the reliability of multi-temporal DInSAR analyses (Prati and Rocca, 1993; Ferretti et al., 2007; Richards, 2009a), maps showing the geographical distribution of the magnitude of the coherence, γ and its spatial and temporal changes, are used for multiple purposes, including e.g., mapping land cover and its changes (Khalil and Saad-ul-Haque, 2018; Jacob et al., 2020; Bai et al., 2020), mapping areas inundated by river floods (Nico et al., 2000; Pulvirenti et al., 2017; Tay et al., 2020) or burnt by forest fires (Donezar et al., 2019), and even for damage assessment (Oxioli et al., 2018). Occurrence of a rapid (compared to the time between the two images) landslide in an area may result in significant modifications of the ground surface and its scattering properties, and therefore of the coherence between the interferometric pair, allowing for the detection and mapping of the landslide.

In our literature database, 13 articles reported results on the exploitation of coherence variations to detect and map landslides. The studies are all recent, and their number has increased in the most recent years.

First, Furuta and Sawada (2013) interpreted local changes in the the polarimetric coherence (Cloude and Papathanassiou, 1998) of the *HH* and *VV* bands of L-band ALOS images as evidence of the presence of landslide failures caused by heavy rainfall in the period from February to March 2011, in the Paranagua area, Brazil.

Mapping the extent of the damage caused by the 25 April 2015, 7.8 M_w Gorkha earthquake, Nepal, using L-band ALOS-2 and X-band COSMO-SkyMed images, Yun et al. (2015) identified three landslides in the Langtang Valley, one of the most popular trekking destinations in the Himalayas. Rock falls and debris falls were visually detected by a decrease of coherence in the ALOS-2 images, allowing the authors to delineate – albeit only roughly – the extent of the landslide debris. Similarly, Konishi and Suga (2017) used changes of coherence in X-Band

COSMO-SkyMed images to detect some of the 107 debris flows and 59 shallow slides caused by heavy rainfall in Hiroshima, Japan, on 20 August 2014 (Wang et al., 2015).

Using C-band Sentinel-1 coherence time series for 2017, Olen and Bookhagen (2018) detected eight changes – of a minimum of ten pixels in size, 300 m^2 – in the magnitude of the coherence from 18 to 30 March 2017, in the Quedraba del Toro area, Central Argentina, which they attributed to new mudflows and other landslides caused by heavy seasonal precipitation. Detection of the landslides was conducted by analysing the geometrical shape of the changes, and assuming a high susceptibility of the local geo-environmental setting. Also using C-band Sentinel-1 imagery, Burrows et al. (2019) exploited a method proposed by the NASA's Advanced Rapid Imaging and Analysis (ARIA) project to prepare urban damage proxy maps (Yun et al., 2015), which they used to classify large landslides caused by the 25 April 2015, 7.8 M_w Gorkha earthquake, Nepal. Landslides showed a drop in the co-event coherence map values compared to the pre-event map values.

Ge et al. (2019) used L-band ALOS-2 images, and tested the use of the coherence, and changes in coherence, to detect and map landslides caused by the 6 September 2018, 6.6 M_w Hokkaido earthquake, Northern Japan (Fujiwara et al., 2019). In apparent contrast with results obtained earlier by Plank (2014) and Konishi and Suga (2017), the coherence and its changes were not good predictors of the presence (or absence) of the event triggered landslides. The authors attributed the (unsatisfactory) result to the vegetation present in their study area. Similar conclusions were reached by Aimaiti et al. (2019) who, when interpreting local surface deformations caused by the same Hokkaido earthquake, found changes in coherence in L-band ALOS-2 images, which they attributed to the presence of newly formed, event landslides. Visual inspection of the map showing changes in coherence allowed for the accurate mapping of the landslide areas. The positive results was counterbalanced by many false positives.

Jung and Yun (2020) used coherence-based approaches to map landslides triggered by the 6 September 2018, 6.6 M_w Hokkaido Eastern Iburi earthquake in Northern Japan (Fujiwara et al., 2019). For the purpose, the authors exploited bi-temporal and multi-temporal, detrended coherence difference and normalised coherence difference changes, obtained from 3 m × 3 m, L-band ALOS-2 imagery, to map the seismically induced landslides, which were detected as statistical anomalies in the imagery in the considered time intervals. The approach performed well where the pre-event coherence was high (i.e., in urban areas, where artificial structures were present), and proved less effectively in areas prone to decorrelation (e.g., in forested terrain, 71% of the study area), confirming the results obtained by Ge et al. (2019).

Goorabi (2020) used C-band, Sentinel-1 images to detect the giant – 3,570 m in length × 2,300 m in width – Maleh-Kabood landslide caused by the 12 November 2017, 7.3 M_S Kermanshah earthquake, Iran. The slope failure caused a decease in coherence of 0.3 in a time series spanning the earthquake, with the coherence increasing after the main shock. The evidence allowed the authors to detect the landslide. A similar multi-temporal approach was used by Tzouvaras et al. (2020) to detect rainfall-induced landslides caused by heavy precipitation on 15 and 20 February 2019 along two main roads in Cyprus. Through statistical analysis, the authors calibrated optimised change thresholds for the 17 February landslide, and then applied the thresholds to detect the 20 February landslides. The experiment revealed that changes in coherence, and in normalised coherence difference in the landslides varied with the satellite orbit and the acquisition angle.

Recently, Burrows et al. (2020) have completed a comprehensive comparison of five coherence-based methods to estimate landslide density at different spatial resolutions using ESA, C-band, Sentinel-1, and JAXA, L-band, ALOS-2 imagery, for four seismically induced landslide events caused by (i) the 2015 7.8 *Mw* Gorkha, Nepal, earthquake, (ii) the 2018, 6.6 *Mw* Hokkaido, Japan, earthquake, and (iii) the 6.8 *Mw* and 6.9 *Mw* earthquakes in the 2018 Lombok, Indonesia, seismic sequence. The authors used two existing methods that exploited pre-event and co-event coherence estimation, the Co-Event Coherence Loss (CECL) (Yun et al., 2015) and the boxcar–sibling method (Burrows et al., 2019), and proposed three new methods that add and combine in different ways post-event coherence measures, including the Post-Event Coherence Increase (PECI), the sum of the coherence increase and decrease (ΔC_sum), and the maximum of coherence increase or decrease, (ΔC_max). The results showed significant variations for the different events and sensors, making it difficult to select an "optimal" method, even if a general preference was given to the three new ones, in particular when used at low resolution (200 m × 220 m). A relevant conclusion of the work was that SAR-based classification methods should be tested on multiple events, as one cannot assume that a method that performs well with one SAR dataset will be equally successful on imagery taken by a different sensor.

Table 2
Summary list of recommendations.

Recommendation	Aim	Section
Provide accurate landslide information	Avoid misinterpretations; favour comparison & interaction	3
Use and explain accepted, standard terminology	Avoid misinterpretations; favour comparison & interaction	6.1
Increase application of SAR imagery	Reduce and manage landslide risk	6.2
Expand number of studies and study areas; focus on poorly investigated physiographical settings	Reduce & manage landslide risk; improve detection & mapping; improve understanding of landslide phenomena	6.2
Perform systematic investigations of landslide failure events in all physiographical settings	Portfolio of detection & mapping solutions for different landslide types	6.4
Test new sensors & combinations of sensors	Expand sensors understanding	6.5
Test image pre-processing designed for landslide failure detection and mapping methods	Improve detection & mapping	6.6
Execute physically based backscatter response studies	Improve detection & mapping	6.7 & 8.2
Combine different bands, for both qualitative and quantitative approaches and classification methods	Improve detection & mapping	6.7 & 8.2
Evaluate the detection and mapping efforts using common set of performance indices	Favour comparison & interaction	6.8
Provide geomorphological insight for numerical results	Avoid misinterpretations; improve understanding of landslide phenomena	6.8
Compare SAR bands performances in different settings and for different types of landslides	Portfolio of detection & mapping solutions for different landslide types	7.3
Perform field measurement of surface backscatter in landslide areas	Theoretical models validation	8.2
Foster the use of fully-polarimetric imagery	Improve detection & mapping	8.2
Combine amplitude and phase products	Improve detection & mapping	8.2
Experiment with sophisticated machine learning	Improve detection & mapping	8.2
Implement operational SAR-based services	Mitigate landslide hazard and associate risk	8.3.2
Adopt standards for landslide failure detection & mapping	Enhance products credibility & usefulness	8.4
Missions to adopt flexible data acquisition programs and distribution policies	Expand use of SAR imagery for landslide detection & mapping	8.4
Define interpretation criteria for landslide failure detection & mapping based on SAR imagery	Favour comparison	8.4
A cost-benefit analysis of a dedicated landslide failure detection & mapping mission	Scientific & operational advancement	8.4

6. Literature analysis

6.1. Terminology and ontology

We noted in the selected literature a lack of homogeneity in the semantic use of the technical language. Key words used in the articles in different, and sometimes contrasting, ways included "resolution, "precision", "accuracy", "recognition", "identification", "mapping", "classification", "validation", "new" (referred to landslides), and "event". In a few articles, "landslide mapping", and its synonyms (e.g., to "construct" or "prepare" landslide inventories), referred to mapping or updating properties of existing landslides, chiefly the activity of slow moving landslides. In a few articles, the detection (and the synonyms, e.g., "recognition", "identification") and mapping of new landslides was in fact the (retrospective) characterisation of the backscattering properties of known landslide areas, and not the detection, mapping, and classification of new slope failures. We further noted a lack of consensus on the meaning of the term landslide "reactivation", and on how to interpret and classify displacements inside pre-existing landslides (Temme et al., 2020).

We conclude that, despite the existing landslide classifications (Cruden and Varnes, 1996; Sidle and Ochiai, 2006; Hungr et al., 2001, 2014; Temme et al., 2020), including recommended terminology and ontology, issues related to the contrasting, and sometimes improper, use of the technical language remain. We consider the problem relevant, because it hampers the comparison of different methods, and it limits the credibility and usefulness of the results (Guzzetti et al., 2012; Reichenbach et al., 2018; Guzzetti et al., 2020). We encourage investigators to use accepted, standard terminology, as this will facilitate multi-disciplinary cooperation. We further recommend that authors explain the terminology they use in their works. This will contribute to avoid misinterpretations, and will favour the interactions among the different disciplines involved in the detection and mapping of landslides exploiting SAR imagery, including e.g., geomorphology, remote sensing, machine learning, visualisation (Table 2).

6.2. Geographical analysis

The 54 articles in our literature collection discussed the use of SAR imagery and related processing approaches and methods for landslide detection and mapping in 147 case studies and 70 study areas located in 32 nations, in all continents, except Antartica (Fig. 2). Japan has the largest number of case studies (50, 34.0%) and of articles published (19, 35.1%), followed by Indonesia (21 case studies, 14.3%), and by China and Nepal (12 case studies each, 8.1%). Asia is by far the continent with most case studies (112, 76.2%, 40 in a single work (Burrows et al., 2020)) and published articles (31, 57.0%), followed by South America and Europe (9 case studies each, 6.1%), and by North America (8 case studies, 5.4%). With no article published, Oceania and Africa have the least number of case studies (5, 3.4%, and 3, 2.0%, respectively) (Fig. 2).

Although the exact or the approximate extent of the study areas was given only in 97 studies, 72 of which in two articles (Mondini et al., 2019; Burrows et al., 2020), visual inspection of Fig. 2 reveals that the studies cover a very small percentage of the global terrain potentially affected by landslides (Nadim et al., 2006; Kirschbaum Bach et al., 2009; Nadim et al., 2013). Comparison of the location of the case studies with (i) the global distribution of fatal, non-seismically-induced landslides from 2004 to 2016 compiled by Froude and Petley (2018), updated to cover the period from January 2004 to December 2017 (black dots in Fig. 2), and with (ii) a global database of inventories of earthquake-induced landslides (Tanyaş et al., 2017), confirms that many areas where landslides are abundant and landslide risk is high were not covered by studies in the literature database. This is surprising, given the well known extent of the global landslide problem (Brabb, 1991; Schuster and Highland, 2001; Nadim et al., 2006; Kirschbaum Bach et al., 2009), and the proclaimed need for modern landslide mapping tools, specifically tools that exploit remotely sensed imagery to prepare landslide maps covering large and very large areas (Guzzetti et al., 2012; Zhao and Lu, 2018; Guzzetti, 2021) and to obtain information on event landslides for the validation of geographical landslide early waning systems (LEWSs) (Piciullo et al., 2018; Guzzetti et al., 2020; Calvello et al., 2020).

We recommend increasing the application of remotely sensed SAR imagery to detect and map landslides, focusing where landslide risk is high or very high, and in areas not yet covered by previous studies (Table 2).

Landscape morphology is known to control the occurrence of landslides (Turner and Schuster, 1996). For each study area, we collected information on terrain elevation and relief – a joint proxy for the landscape topographic and morphological variability and complexity. We note that the case studies were conducted in a broad range of terrain elevation – from sea level to almost 5300 m of elevation in Nepal (Burrows et al., 2019) – and relative relief (from less than 10 m to more than 1880 m). We conclude that, overall, the variability and complexity of the landscape do not limit the application of SAR imagery for the detection and mapping of landslides. This is a positive conclusion. However, due to limitations inherent to the side-looking geometry of SAR sensors (Fig. 3) terrain morphology, chiefly slope angle and orientation, affect the ability of the radar sensors to properly illuminate the terrain, and consequently of an investigator to detect and map the landslides. In steep mountain terrain, the number and proportion of the slopes that are not illuminated by a radar sensor because of shadows or layover effects (Fig. 3B) can be significant, preventing the detection and mapping of landslides.

Geology, seismicity, meteorology, climate, land use and land cover are all known to condition the distribution and abundance of landslides (Turner and Schuster, 1996; Sidle and Ochiai, 2006; Hungr et al., 2014; Vanmaercke et al., 2014; Gariano and Guzzetti, 2016; Tanyaş et al., 2017; Vanmaercke et al., 2017; Fan et al., 2019). Hence, we investigated the local or regional settings of the study areas searching for relations with the SAR detection and mapping methods and capabilities.

We first used the map showing the Generalized Geology of the World compiled by Chorlton (2007) to assign a prevalent geological domain to each study area, considering five rock type domains (i.e., igneous, metamorphic, sedimentary, tectonic, and volcanic rocks). We found that the study areas were in all the geological domains, and primarily in sedimentary rocks (58.5%), and subordinately in crystalline metamorphic rocks (12.8%), volcanic and intrusive rocks (8.5%), volcanic rocks (7.1%), intrusive rocks (5.7%), sedimentary and volcanic rocks (4.2%), in a combination of crystalline, intrusive and sedimentary rocks (2.8%), and in other rock combinations in smaller percentages.

We then used the Global Seismic Hazard Map of Giardini et al. (2003) to attribute a seismicity level to each study area, in four classes (low, moderate, high, very high). We found that the study areas were in all seismic classes, and more numerous in the moderate (30.0%) and the high (30.0%) classes, followed by the very high (24.2%) and the low (15.8%) classes. Considering the location of the 30 studies that detected and mapped seismically-induced landslides, we found that most of the studies were in compressive tectonic regimes where the movement of regional thrusts was the primary cause of the landslides. This was expected, given the known global distribution of earthquake-induced landslides (Fan et al., 2019).

Next, we used the world climate map of Peel et al. (2007) to assign a dominant, or prevalent Köppen-Geiger climate type (i.e., tropical, arid, temperate, cold, polar), and the high resolution, interpolated annual precipitation information of Hijmans et al. (2005) to assign an estimate of the mean annual precipitation (MAP) – or a range of MAP – to each study area. We found that the study areas were in all climate types, except the polar climate. The temperate climate type, with 36 study areas (51.4%), sixteen of which in the hot summer sub-group (Cfa), has twice as many study areas than the cold (15, 21.4%) and the tropical (13, 18.5%) climate types. In the study areas, the MAP ranges from a

minimum of 244 $mm \cdot y^{-1}$ at Quadreba del Toro, Argentina, to a maximum of 4477 $mm \cdot y^{-1}$ in the Karnatak Province, India. In both areas landslides were rainfall-induced.

Ultimately, we used Google Earth to assign visually a predominant land cover type to each study area. Adopting the Corine Land Cover (CLC) second level nomenclature (European Environment Agency, 1992, 2007), we assigned the "forest" type (3.1) to 25 study areas (35.7%), "open spaces with little or no vegetation" (3.3) to seven study areas, "shrub, herbaceous vegetation" (3.2) to three study areas, and "mine, dump, construction sites" to two study areas. To the remaining 33 study areas, we attributed two predominant land cover types i.e., 3.1 and 3.2 in 11 study areas, 3.2 and 3.3 in eight study areas, and 3.1 and 3.3 in six study areas. A few study areas exhibited percentages of "pastures" (2.3), "heterogeneous agricultural areas" (2.4), and "urban fabric". The presence of forest in at least 47 study areas (67.1%) suggests that multi-, single-polarisation, and in some cases coherence based products are well suited to detect and map landslides in forested terrain. This is a positive result because SAR sensors can complement optical sensors in the absence of direct solar illumination to detect and map landslides. However, we note that Mondini et al. (2019) failed to detect landslides in four study areas in Colombia where an equatorial forest was present.

From this geographical analysis, we conclude that SAR imagery can be used to detect and map landslides in most of the morphological, geological, seismic, meteorological, climate, and land cover settings. This is good news. However, we note that for some of the settings the number of studies was limited, reducing the significance of the results. We therefore recommend to expand the number of studies and of study areas, focusing on physiographical settings poorly or not previously investigated (Fig. 2), as this will foster our understanding of possible limitations of the SAR imagery in specific settings (Table 2). We expect the role of SAR imagery to be more relevant in equatorial, tropical, and sub-tropical areas where landslides are abundant and the cloud coverage can be persistent, hampering the use of optical imagery.

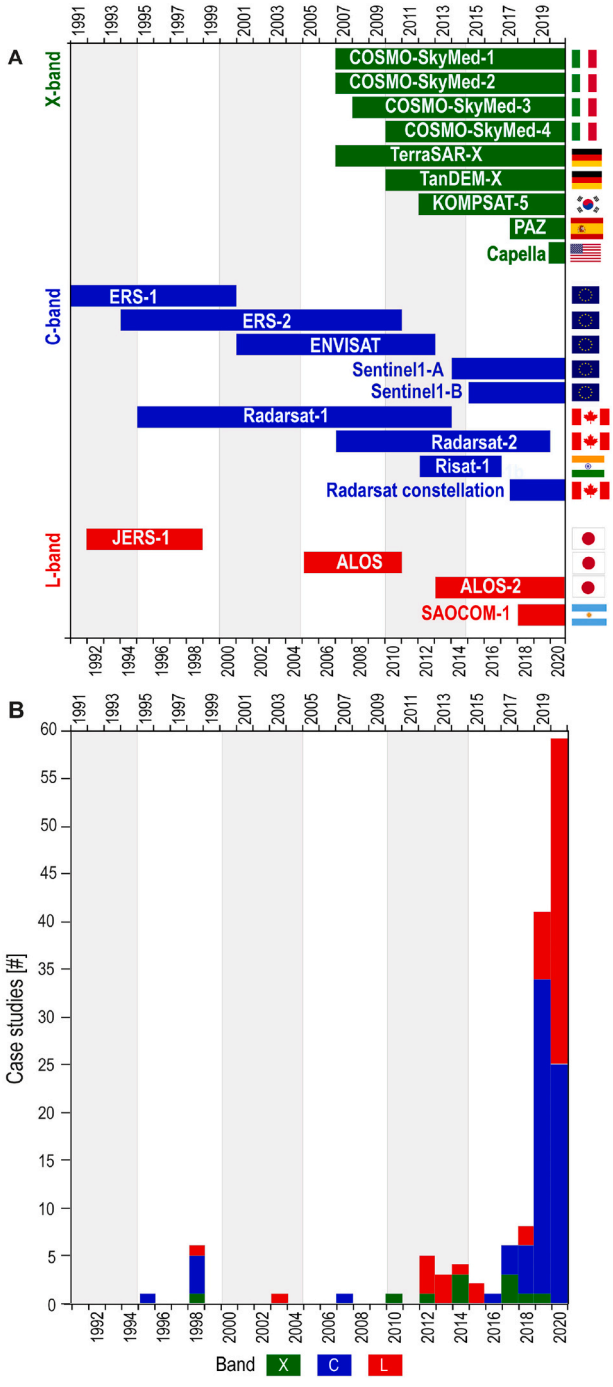

Fig. 5. Temporal analysis. (A) Temporal coverage of SAR satellites. (B) Number of case studies that used different SAR bands. See Table 1 for details on the satellite sensors.

6.3. Temporal analysis

Of the 147 case studies in the literature database, 139 (94.5%) provided information on the time, date, or period of occurrence of the landslides, including four articles for which we inferred the temporal information from the date or period of the landslide-triggering event e.g., an earthquake, a typhoon.

Inspection of Fig. 1B reveals a constant increase in the number of articles published, with a rate of about one article per year between 1992 and 2011, increased to about 5 articles per year between 2012 and 2017, and increased further to exceed 7 articles per year between 2018 and 2020 – with the figure for 2020 limited to the eleven-month period from January to November. We take this as evidence of the increasing interest of investigators in the use of SAR imagery for landslide detection and mapping. We further notice a nearly constant period of ≈2.7 years between the date of the triggering event and the publication of the article. This rather long period reveals the interest of the investigators to experiment with their detection and mapping techniques, as opposed to documenting the landslide events. Ultimately, we notice an average period of ≈4.2 years between the launch of a satellite and the first appearance of an article using the imagery taken by the satellite, and we observe that this latency has decreased over the years. We consider this evidence of the investigators' confidence in the SAR capabilities, interest to experiment with new sensors, and the ability to obtain and process SAR images.

The rising number of published articles per year is only partially related to the increasing availability of SAR imagery, and particularly of satellite imagery. Inspection of Fig. 5A reveals that (i) the availability of X-band sensors has increased rapidly from 2007 to 2010, and has remained about constant since then; (ii) following an early period (1991–1994) when only the ESA ERS-1/2 satellites were at hand, the availability of C-band sensors has remained about constant; and (iii) the availability of L-band sensors has also remained constant – albeit intermittent – until 2018. Further, inspection Fig. 5B reveals that, despite the larger availability of X-band sensors, investigators have preferred C-band, and L-band sensors. The sharp increase in the number of case studies that used C-band imagery in 2019, and C-band and L-band imagery in 2020, is due to the works of Mondini et al. (2019) and Burrows et al. (2020), with 32 and 40 case studies, respectively.

6.4. Landslide types and triggers

Only 26 articles (48.1%), investigating 103 case studies, (70.0%), provided information on the type (or types) of landslides using standard nomenclature (Cruden and Varnes, 1996; Hungr et al., 2014), with "debris flow" (6), "shallow landslide" (5), and "mud flow" (3) the most commonly reported landslide types in the catalogue. This was expected, as these landslide types are among the ones that leave a distinct signature on the ground surface. Further, only 18 articles (33.3%) gave quantitative information on the size (length, width, area, volume) of the landslides. We consider this a limitation of the published studies that prevents in-depth analyses of the relations among landslide types and sizes, the types and resolutions of the imagery used, and the methods used to detect and map the landslides.

About 53% of the case studies concentrated on single landslides. For these studies, the study site coincided with the landslide area, the landslide area and its immediate surroundings, or the slope where the landslide was located. The remaining ≈ 47% of the studies detected or mapped landslide populations. In these more regional studies, the study area extended from a few tens (Moro et al., 2007) to several thousands (Ge et al., 2019; Aimaiti et al., 2019) square kilometres, and for most of the cases it was limited by the coverage of the available imagery. This limits the possibility to investigate and measure the extent and magnitude of the landslide events (Malamud et al., 2004a). The evidence confirms that investigators were interested primarily in testing their detection or mapping techniques on single sites or areas of limited extent, and less interested in documenting the landslide events and in preparing landslide inventory maps for large and very large areas, albeit a few exceptions exist (Singhroy, 1995; Singhroy et al., 1998; Barra et al., 2016). This is confirmed by the prevalent type of journals where the articles were published, which are mainly remote sensing journals (Fig. 1A).

A large proportion of studies were aimed at mapping event landslides i.e., individual landslides or populations of landslides caused by a single trigger – including an earthquake (35 studies), an earthquake sequence (three studies), a rapid snowmelt event (four studies), a rainfall event (40 studies), or a series of rainfall events in a season (one study) – with only seven studies aimed at updating geomorphological inventory maps (Guzzetti et al., 2012). We conclude that SAR imagery and related pre-processing and classification techniques are well suited to investigate event landslides, either single or populations of landslides, and we encourage investigators to perform systematic investigations of landslide events in all physiographical settings, wherever this is possible. This will contribute to building a portfolio of detection and mapping solutions for different physiographic and landslide types (Table 2).

6.5. Platforms and bands

In the early days, airborne sensors were instrumental to prove that SAR imagery could be used to detect and map landslides successfully (Singhroy, 1995; Rodriguez et al., 2002; Czuchlewski et al., 2003). Today, the studies that exploit SAR images taken by satellites (134, 91.1%) outnumber more than 10-to-1 the studies that use images taken by airborne sensors (10, 5.8%), with only four (2.7%) studies that exploit both (Singhroy et al., 1998; Yamaguchi, 2012; Shibayama and Yamaguchi, 2013; Shimada et al., 2014). This was expected, given the higher availability of SAR imagery taken by space-borne sensors, and the higher difficulty in obtaining and treating SAR imagery taken by airborne sensors (e.g., designing and running a campaign, removing the motion errors), despite the higher flexibility of the airborne platforms in resolution, flight direction, and configuration (e.g., in the choice of the band). Unfortunately, the only found example on the use of a band different from X,C, or L (Tien Bui et al., 2018), was not documented and then, it was not not taken into consideration in our analysis).

Of all the satellite platforms, the most used are the ESA, C-band, Sentinel 1a/b (https://sentinel.esa.int/web/sentinel/missions/sentinel-1), which were used by the authors of 14 articles for 65 case studies – with 52 case studies in two works [182, 24] – followed by the Japanese, L-band, ALOS and ALOS-2, used in six and twelve articles, respectively, in 34 different case studies.

An inspection of Fig. 5B reveals that, despite the larger availability of X-band sensors (Fig. 5A), investigators have preferred C-band and L-band sensors. Of all the satellite platforms, the most used are the ESA, C-band, Sentinel 1a/b (https://sentinel.esa.int/web/sentinel/missions/sentinel-1) – used by the authors of 14 articles for 65 case studies – followed by the Japanese, L-band, ALOS and ALOS-2 – used in six and twelve articles, respectively, in 34 different case studies. We note that the sharp increase in the number of case studies that used C-band imagery in 2019, and C-band and L-band imagery in 2020, is due to the works of Mondini et al. (2019) and Burrows et al. (2020), with 32 and 40 case studies, respectively. We do not know if this is casual, or a shift in the scientific community towards a more systematic use of the two bands for landslide detection and mapping. The trend needs to be verified in the future.

A number of SAR satellites potentially suited for landslide detection and mapping, including the Korean X-band KOMPSAT-5 (KARI, 2020), the Indian C-band RISAT-1 (Department of Space, Indian Space Research Organisation, I, 2020), the Canadian C-band Radarsat constellation (Canadian Space Agency, 2020), or the Argentinian L-band SAOCOM 1A (Comisión Nacional de Actividades Espaciales, 2020) (Fig. 5, Table 1), have not been used yet. This is surprising, considering that some of these satellites were used to monitor landslides with DInSAR (e.g., Lee, 2010; Bhattacharya and Mukherjee, 2017; Bovenga et al., 2018; Roa et al., 2020). The lack of studies may be due to the fact that some of these satellites are recent (e.g., the C-band Radarsat constellation, the L-band SAOCOM 1A), whereas for others it may not be easy or it may be expensive to obtain the images. We encourage investigators to test the new sensors, wherever possible in combination with other sensors, as this will expand our understanding of the use of different platforms (Burrows et al., 2020) to detect and map landslides (Table 2).

Ultimately, it is difficult to determine whether there is a relationship among the number of the case studies, of the available satellites (Fig. 5), and of the images used. In our review, we counted approximately 200 images used in 26 years, a minute number.

6.6. Pre-processing

"Speckle", illumination, geometric distortion, and geocoding were the primary problems faced by investigators in the preparation of the SAR images. Speckle (or "speckle-like") hampers – or prevents – the heuristic, visual interpretation (Gabriel, 2002) and the quantitative use of SAR imagery. Various filters are used to reduce the speckle. In the catalogue, the most popular are the Lee filter (Lee, 1981, 1986; Lee et al., 1994a) used ten times, two times in the "refined" or "advanced" version, and the Frost filter (Frost et al., 1982) used six times, followed by the "median" filter, used three times. Park and Lee (2019) used the IDAN (Vasile et al., 2006) filter, Li et al. (2014a, 2014b) an "averaging" filter, and Esposito et al. (2018) an "anisotropic" filter. Konishi and Suga (2018a) confronted the "median", Lee, and Frost filters, and preferred the later, in terms of overall classification accuracy (OA), whereas Mwaniki et al. (2017) experimented the joint use of the Lee and Frost filters. When multi-look is applied to obtain images with a nominal pixel size, the averaging process on the original cells can introduce a filtering effect (Cantalloube and Nahum, 2000; Oliver and Quegan, 2004). Multi-look was performed by the authors of 24 articles, but only eight articles considered filtering (Luo et al., 2016; Mondini, 2017; Konishi and Suga, 2018a; Fujiwara et al., 2019; Mondini et al., 2019; Esposito et al., 2020; Burrows et al., 2020; Goorabi, 2020). Interestingly, Czuchlewski et al. (2003) deliberately did not perform any speckle filtering, speculating that their scattering mechanism extraction approach was sensitive enough to detect the gigantic Tsaoling rockslide at the spatial resolution of the L-band airborne FP AIRSAR imagery used.

Illumination issues are a consequence of the side-looking geometry typical of SAR systems (Meyer, 2019), and consist of shadows, foreshort and layover (Fig. 3B). Only a few authors assessed or considered the impact of geometric distortions on their analyses (Singhroy et al., 1998; Balz and Liao, 2010; Watanabe et al., 2012; Konishi and Suga, 2017; Liu et al., 2018; Mondini et al., 2019; Adriano et al., 2020; Goorabi, 2020; Tzouvaras et al., 2020), and others excluded from the analyses (i.e., masked) the areas affected by shadows or in layover (Chorowicz et al., 1998; Li et al., 2014a, 2014b; Mondini, 2017; Tessari et al., 2017; Konishi and Suga, 2018a; Burrows et al., 2020; Esposito et al., 2020; Jung and Yun, 2020; Ohki et al., 2020). To mitigate geometric distortions distortions, Aimaiti et al. (2019) used images taken along ascending and descending orbits, whereas Luo et al. (2016), for their change detection approach, considered irrelevant the geometric distortions. Only Mondini et al. (2017) gave the percentage of pixels affected by geometric distortion in his analysis, key information to quantify the areas in which landslides could not be detected.

We note that for most of the studies the image pre-processing was not designed specifically for landslide detection and mapping, but for other applications. Studies that exploited the SAR phase through DInSAR and coherence products used pre-processing designed chiefly for interferometry. Studies that exploited multi-polarisation used some form of signal decomposition, whereas the multi-temporal studies exploited different forms of calibration and co-registration. We conclude that there is no guarantee that the performed pre-processing was "optimal" for landslide detection and mapping. We consider this a limitation, and we encourage investigators to experiment with image pre-processing approaches designed specifically for the purpose of detecting and mapping landslides in particular in relationship to filters and terrain correction (Table 2).

6.7. Detection and mapping methods

For the detection and mapping of landslide failures, investigators have experimented multiple methods, which – for descriptive purposes – we group loosely into qualitative and quantitative methods. The qualitative methods consist of the expert, visual interpretation of images derived, in various ways, from SAR images. This is similar to the visual interpretation of aerial photography or optical satellite imagery (Guzzetti et al., 2012). A total of 23 articles (42.6%) discussed qualitative, visual interpretation methods applied to 58 case studies (39.4%) with a nearly constant rate of ≈ 1.5 studies per year until 2019, a maximum of three studies in 2018, and no studies in 2020. The visual interpretation methods were applied mainly to images showing the ground backscatter and its changes obtained by processing C-band imagery (Fig. 7A).

The quantitative methods include empirical investigations based on numerical and/or statistical techniques. This is equivalent to statistically-based landslide susceptibility modelling (Reichenbach et al., 2018). In 31 articles discussing results in 33 different study areas, investigators have used 89 times a quantitative method – including 70 times a threshold based method, eight times unsupervised, and seven times supervised classification methods – and four times mixed, thresholds and decision tree methods (Fig. 7). Beginning in 2012, the rate of articles exploiting quantitative methods has risen continuously, with Burrows et al. (2020) and Ohki et al. (2020) who repeated experiments conducted by previous authors. Regardless of the method, all the investigators interpreted landslides as "anomalies" in regular patterns in the imagery and maps. Interpretation was facilitated where multi-polarisation derived products were available, mainly because the decompositions allowed for the visual discrimination between forested or vegetated (i.e., stable) terrain and bare terrain, the later inferred to be a landslide. Where multi-temporal approaches were adopted, landslide detection and mapping was further facilitated by the fact that in the imagery landslides appeared as clusters of homogeneous pixels surrounded by a "salt and pepper" matrix of random changes (Fig. 4).

For quantitative methods, most authors preferred multi-polarisation

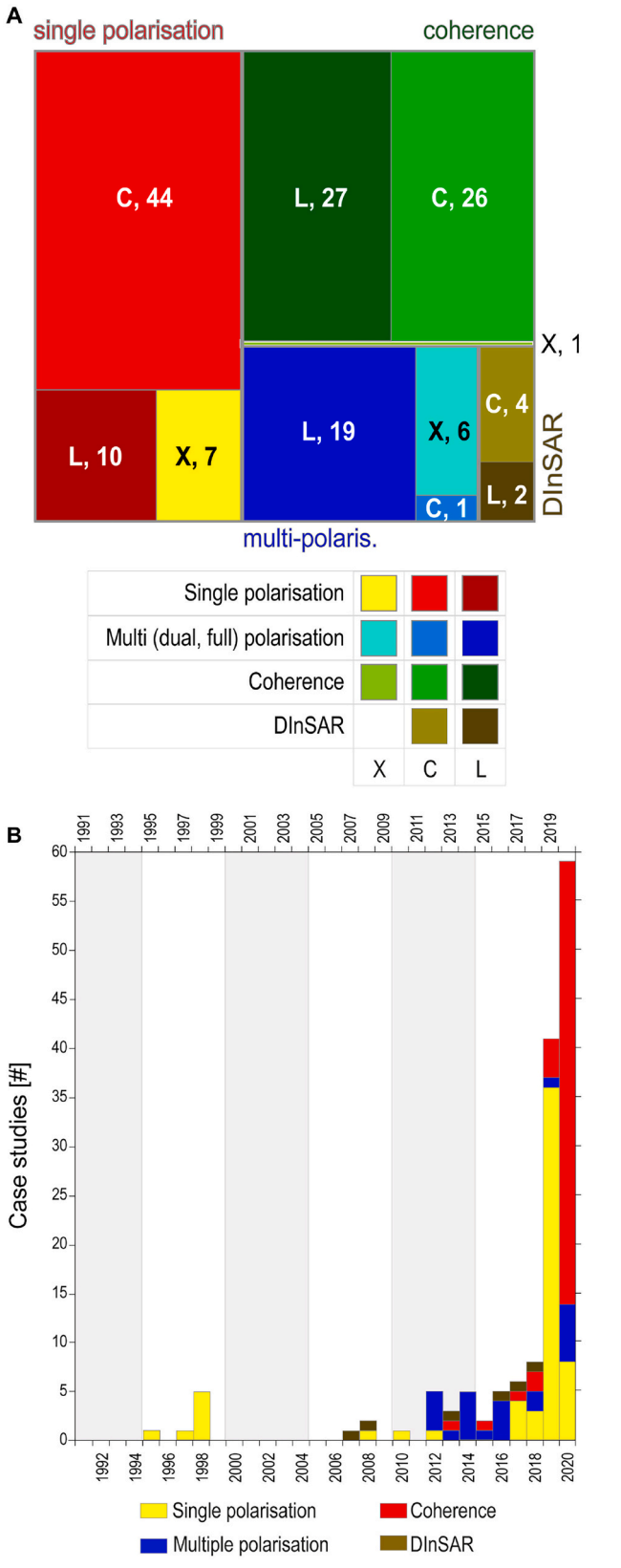

Fig. 6. Analysis of approaches in the literature database. (A) Tree chart shows number of case studies that used (i) the type of approaches (single polarisation, multiple (dual, full) polarisation, coherence, DInSAR) and (ii) the selected band type (X-band, C-band, L-band). (B) Bar chart shows the temporal trend of the approaches.

products obtained from L-band imagery. This was expected, because of the high information content of the imagery. Inspection of the literature reveals a large number of studies (15, 27.7%) that exploited FP L-band imagery, with most of the study areas in Japan. We maintain that this is the result of the availability of L-band, ALOS and ALOS-2 imagery taken after large landslide triggering events in Japan, and not an a-priori research design based on the specific properties of the L-band imagery (e.g., its high penetration capacity).

Overall, the quantitative methods exploited the statistical behaviour of the backscatter properties of different land cover classes (e.g., forest, bare ground), or their temporal and spatial variations, and did not investigate the physical properties of the observed objects. We note that the covariates used in the statistically-based classification models follow different statistical distributions whose shape can change when the images are over- or sub-sampled, filtered, or transformed (Oliver and Quegan, 2004; Lopès et al., 2008), with consequences on the use of the quantitative methods. We recommend to address these issues, and to design and execute physically based (i.e., "theoretical") studies in which the backscattering response of the landslide surface structures are related to the penetrating capacity of the different radar bands. We further recommend designing experiments that combine different bands, for both qualitative and quantitative approaches and classification methods (Table 2).

Considering on the relationships between the SAR bands and the methods used to detect and map the landslides, Fig. 6A reveals that: (i) C-band imagery was used in 75 case studies (51.0%), L-band imagery in 58, (39.4%), and X-band imagery in only 14 studies (9.5%); (ii) the case studies that used amplitude data, including single-polarimetric (61, 41.4%) and multi-polarimetric (26, 17.6%) approaches, outnumbered the case studies that used phase data, including coherence (54, 36.7%) and DInSAR (6, 4.0%) approaches; (iii) the case studies that used C-band amplitude, single-polarimetric approaches were the single most numerous (44, 29.9%), followed by case studies that used L-band and C-bands coherence approaches (27, 18.3% and 26, 29.9% respectively) – with the figures influenced by the works of Mondini et al. (2019) and Burrows et al. (2020); and (iv) no study used DInSAR techniques with X-band data, whereas only one study used coherence of X-band imagery, and one study C-band, multi-polarimetric approaches.

6.8. Quality analysis

For a quality analysis, we consider two, equally important aspects: (i) the completeness of the information, and (ii) the analysis of information on the validation of the results of the landslide detection or mapping exercises.

To quantify the abundance of information in each study, we selected eight information types, which we consider of primarily relevance for the quality of a study i.e., (i) areal extent of the study area – most relevant for case studies dealing with populations of landslides, (ii) land cover types, (iii) number of landslides, (iv) landslide type(s), (v) landslide size, (vi) landslide trigger, (vii) the type of SAR imagery and the description of the pre-processing, and (viii) whether a validation was performed. Next, for each article, we counted the number of information types for which data was available. Then, we attributed to each article a "completeness score" equal to the number of information types, from zero to eight. Inspection of the frequency of the completeness scores (Fig. 8) reveals that no article has the lowest completeness score (0), one article has the highest score (8), and the average score is 4.7 (st.dev = 1.7). We stress that the completeness score does not measure the quality of the information given in the articles, but we maintain that more information characterises a better quality article.

Analysis of the landslide detection and mapping experiments revealed that 24 studies (44.4%) performed a qualitative validation, 20 studies (37.0%) a quantitative validation, and the remaining 10 studies (18.6%) did not perform any form of validation (Fig. 9A). The quantitative analyses performed the validation using multiple combinations of six different performance indices obtained from standard confusion matrices, including the overall accuracy (OA), Recall (Rc), Precision (Pr), Cohen's k (Cohen, 1960), F1-score (F1), and Success rate (Sr).

Most of the qualitative validations were executed comparing the landslide detection or mapping results with satellite optical images or ortho-photographs that captured the same landslide events. Three authors preferred to validate their landslide detection results using independent information obtained in the field or from chronicles. In some articles, in particular where photo-interpretation was used to classify the images, validation was not discussed or was missing entirely. For the quantitative validations, the necessary confusion matrix was prepared using independent landslide information obtained from official sources (Balz and Liao, 2010; Mwaniki et al., 2017; Ge et al., 2019; Aimaiti et al., 2019; Ohki et al., 2020; Jung and Yun, 2020; Adriano et al., 2020), or from landslide inventory maps prepared for validation purposes using satellite optical imagery.

Fig. 9B illustrates the temporal trend of the performed validations. We note that the number of quantitative validations has increased over time. This is a positive finding. We also note that the number of combinations of performance indices is large (Fig. 9A), and we encourage investigators to perform the evaluations of their detection and mapping exercises using a common set of performance indices. This will facilitate the quantitative comparison of the results of different studies. We further recommend authors to provide a geomorphological insight for their numerical results, and in particular to motivate the false classifications (Table 2).

7. Comparison of approaches and results

A few investigators have confronted the results of the application of different techniques in the same study areas, or the application of the same or similar techniques using different imagery. In this *sec*tion we summarize these comparisons.

7.1. Amplitude and phase products

Konishi and Suga (2017), Ge et al. (2019), Aimaiti et al. (2019), and Jung and Yun (2020) confronted coherence and various amplitude-based products. To detect and map the numerous large debris flows triggered by torrential rainfall in Hiroshima, Japan, on 20 August 2014 (Wang et al., 2015), (Konishi and Suga, 2017) preferred coherence over NDSI obtained by processing X-band COSMO-SkyMed images. The choice was based on an heuristic, qualitative assessment. Differently, to map shallow landslides (Yamagishi and Yamazaki, 2018) triggered by the 6 September 2018, 6.6 M_w, Hokkaido Eastern Iburi earthquake, Northern Japan, Ge et al. (2019), Aimaiti et al. (2019), and Jung and Yun (2020), processed a set of ALOS-2 images and obtained better OA scores using intensity difference and intensity correlation rather than coherence based products.

We explain the contrasting result with (i) the presumed higher sensitivity of SAR coherence to subtle or minor land cover changes, and the corresponding higher sensitivity of SAR backscatter to major land cover changes (Plank, 2014), in particular in forested areas where coherence is typically low; (ii) the different landslide types (debris flows and shallow landslides); and (iii) the different characteristics of the images used, namely a 3 m × 3 m, shorter wavelength, X-band COSMO-SkyMed image for the first study, and a 1.43 m × 1.95 m, longer wavelength, L-Band ALOS-2 image for the last studies. As pointed out by Ge et al. (2019), more tests on different events are needed to confirm these results.

To map a single, large, seismically-induced rockslide triggered by the 6.4 M_w earthquake that hit western Pakistan on 28 October 2008, Furuta and Tomiyama (2008) preferred DInSAR to NDSI obtained by processing an L-band ALOS-2 image, originally at 10 m × 10 m resolution. DInSAR analysis showed a maximum, local, LOS deformation of about 6 cm in the landslide area, which was too small to produce changes visible in the

NDSI. Conversely, other landslides causing large displacements were captured by the NDSI, and not by DInSAR.

7.2. Polarisation products

In the attempt to map the giant, 1.25 × $10^8 m^3$ Tsaoling rockslide (Hung et al., 2002; Chigira et al., 2003; Chen et al., 2006) triggered by the 21 September 1999, M_w 7.7, Chi Chi earthquake in Central Taiwan, Czuchlewski et al. (2003) preferred post-event full-polarisation to dual-polarisation (HV-HH) L-band, airborne AIRSAR imagery (NASA Jet Propulsion Laboratory, 2020a), because the decomposition of the backscattering matrix allowed for a direct identification of two types of terrain useful to detect landslides i.e., bare, rocky terrain (the landslide), and forest (the stable terrain). Still, the authors were able to recognise the same landslide proposing a dual-polarisation based, simplified vegetation index, and concluded that an L-band system with dual co-polarisation and cross-polarisation channels was sufficient to identify landslides that took out the vegetation. The large areal extent of the landslide, the high resolution of the airborne imagery, and the strong ground changes caused by the landslides facilitated its detection.

In an experiment aimed at mapping six seismically-induced landslides – three in forested terrain and three in grassland and shrubs – triggered by the 16 April 2016, 7.0 M_w Kumamoto earthquake, Kyushu, Southern Japan, Park and Lee (2019) used two fully-polarimetric L-band ALOS-2 images, one taken before and one after the earthquake. They preferred changes of P, H, and $\mathscr{A}$ (sec. 5.1.1) between the pre-event and the post-event images, than P, H, and $\mathscr{A}$ obtained from the single post-event image.

Although the authors did not provide information on the type of landslides, Xu et al. (2017) reported independently that most of the seismically-induced landslides were shallow, disrupted falls, with a few flow-type slides, and rock and soil avalanches. Large, deep-seated, co-seismic landslides were also identified by Mukunoki et al. (2016). The study revealed that thresholded changes of single- and dual-polarisation backscatter coefficient allowed for high detection rates, but suffered from a large number of false positives (commission errors). The map prepared using change detection products obtained from pre-event and post-event, fully-polarimetric images performed better (Cohen's k = 0.45) than all the other products – i.e., single, post-event fully-polarimetric image; post-event, dual-polarisation image; change detection of pre-event and post-event single-polarisation imagery – when compared to a reference inventory map obtained through the visual analysis of post-event aerial photography. The same conclusions were reached by Ohki et al. (2020) who mapped landslides triggered by heavy rainfall on 5–6 July 2017, in Kyushu, Japan (Ochiai et al., 2017), and by the 6 September 2018, 6.6 M_w, Hokkaido Eastern Iburi earthquake, Northern Japan, using 3 m × 3 m resolution, FP ALOS-2 images. The authors found that the single polarimetric (SP) imagery was not useful to detect the event triggered landslides, but did not provide information on the parameters used for the comparison.

Konishi and Suga (2018b) used three polarimetric indices obtained from processing pre-event and post-event L-band ALOS-2 imagery to detect and map landslides triggered by the 6 April 2016, 7.0 M_w, Kumamoto earthquake, Kyushu, Southern Japan. Adopting a change detection approach, the authors trained a random forest classifier using separately the $\bar{\alpha}$, entropy H, and polarimetric correlation coefficient in bare soil (considered to be landslides), forest, grass and crop, paddy, and urban (built-up) areas. Overall accuracy was high for the three classifications (OA = 0.86, 0.85, and 0.73, respectively), confirming the potential of the technique for landslide detection and mapping.

7.3. Band comparison

To map landslides of unknown type and size in the Chicamocha valley, Northern Colombia, Chorowicz et al. (1998) used 12.5 m × 12.5 m C-band ERS-1 and 18.0 m × 18.0 m L-band JERS-1 images in simulated pseudo-stereoscopic amplitude-based products. The authors preferred the JERS-1 images due to the larger acquisition incidence angle (≈35° vs. ≈23°), which facilitated the 3-D stereoscopic view of the surface deformations caused by the landslides. They also concluded that the different wavelengths (C, L) and spatial resolutions were not important for landslide detection and mapping.

In an attempt to detect rainfall-induced landslides caused by typhoon Talas, in Totsukawa-mura, Japan, in August and September 2011, Shimada et al. (2014) compared airborne Pi-SAR-L2 L-band and X-band TerraSAR-X imagery. The experiment revealed that polarimetric entropy, H and the HH/HV power ratio were both effective in detecting land cover changes (from forest to bare ground) caused by the occurrence of the landslides, and more so when using the L-band airborne SAR. The experiment also showed that the X-band TerraSAR-X was less sensitive to land cover changes, probably because of the reduced penetration through forest of the shorter wavelength, X-band, compared to the longer wavelength, L-band, imagery (Shimada et al., 2014).

Burrows et al. (2020) confronted low resolution (200 m × 220 m) and high resolution (20 m × 22 m) landslide density maps (Guzzetti et al., 2000) prepared using C-band, Sentinel-1 and L-band, ALOS-2 imagery for the areas affected by (i) the 2015, 7.8 *Mw* Gorkha, Nepal, earthquake, (ii) the 2018, 6.6 *Mw* Hokkaido, Japan, earthquake, and (iii) the 6.8 *Mw* and 6.9 *Mw* earthquakes in the 2018 Lombok, Indonesia, seismic sequence. Results obtained using the L-band imagery outperformed the results obtained using the C-band imagery. Despite, the authors argued that Sentinel-1 imagery was a valuable choice for emergency management due to the mission 6-day revisit time (Table 1).

The number of experiments that compared the performance of SAR bands is too limited, and the results are too dependent on the local settings to allow for a general conclusion. We recommend performing experiments to compare systematically the performance of SAR bands for landslide failure detection and mapping in different environmental and physiographical settings, and for different landslide types.

8. Discussion and perspective

Our literature review shows empirical evidence that satellite or airborne SAR imagery can be used to detect and map landslide failures in a variety of settings. However, no clear evidence is provided on the characteristics of SAR imagery that allow it to be used for detecting and mapping landslide failures. To fill this gap, we first examine if the SAR imagery commonly used for landslide failure detection and mapping (Table 1) are theoretically adequate for the scope, and we present a general framework for the detection and mapping of landslide failures and of populations of event failures using SAR imagery (Fig. 10). Next, we outline the main research needs to consolidate the theoretical framework, and to improve the existing capabilities to detect and map landslide failures. Ultimately, we consider the potential for SAR-based operational landslide mapping services, and we provide a perspective for the extensive use of satellite and airborne SAR-imagery for landslide failure event detection and mapping.

8.1. Theoretical framework

Where landslides occur, they leave discernible signs that can be recognised and mapped (Rib and Liang, 1978; Turner and Schuster, 1996; Guzzetti et al., 2012). Most of the signs used to recognise a landslide in a landscape are changes in the ground surface characteristics from the situation before the landslide, including morphological, lithological, geological, and land-cover modifications. Depending on the landslide velocity (Cruden and Varnes, 1996; Hungr et al., 2014), the style of activity (Cruden and Varnes, 1996), and the landslide repetition, recurrence, and reactivation pattern (Temme et al., 2020), changes can be abrupt or gradual and multiple signs can coexist in an area, facilitating the recognition of a landslide by trained investigators.

When using remote-sensing imagery, the most relevant and effective

signs are related to morphological modifications and land-cover changes (Guzzetti et al., 2012). Morphological modifications – i.e., the landslide topographic or geometric "signature" (Pike, 1988) – consist of changes in the form, shape, position, or appearance of the topographic surface, and can occur at very different length-scales (from sub-centimetre to kilometre scale) depending on the size and type of the landslides. Land-cover changes result chiefly from the partial or total removal, or from the modification of the vegetation in the landslide area, or in parts of the landslide area, which result in radiometric differences in the imagery. The type and extent of the land-cover changes depend on the size, type, and velocity of the landslide (Sidle and Ochiai, 2006; Hungr et al., 2014).

Optical imagery taken by airborne or space-borne sensors has long been used to detect and map landslides of very different types in a variety of physiographical settings (Turner and Schuster, 1996; Guzzetti et al., 2012). In an optical image, landslides – and in particular "fresh", event-triggered landslides – are easy to recognise by trained investigators, mainly because they appear as (visual) morphological and land-cover "anomalies" compared to the surrounding stable terrain. The modern, automatic or semi-automatic methods used to detect and map landslides by processing optical images mimic the mental (heuristic) process performed by an investigator and attempt to capture "anomalies" in the imagery. This can be done by comparing pre-event and post-event conditions, or by searching for local differences in image patterns at various length scales (Mondini et al., 2011; Lu et al., 2011; Guzzetti et al., 2012; Lv et al., 2018; Tavakkoli Piralilou et al., 2019; Lu et al., 2019b).

When using optical imagery, the heuristic (human) or numerical (computer-based) interpretation and recognition process is "natural", because optical sensors – including the human eyes – operate in the range of the electromagnetic spectrum to which we are accustomed (400–700 *nm*, 430–750 *THz*). Radar sensors commonly used for landslide detection and mapping (Table 1) operate in a different region of the electromagnetic spectrum, and it is worth asking if landslides can – in principle – be detected by radar sensors.

We first consider the wavelength and the ground resolution of the satellite SAR sensors. The first controls the size of the ground elements that can interact with the wave, and the second the size of the smallest geomorphological feature that can be detected and mapped. The SAR bands used to detect and map landslides range from ≈ 3.1 *cm* (X-band), to ≈ 5.5 *cm* (C-band), to ≈ 23 *cm* (L-band) (Table 1). These wavelengths are much smaller than the characteristic landslide length scales – in the range from meters to kilometres (Malamud et al., 2004a; Hungr et al., 2014) – and comparable to the length scales of morphometric elements typical of landslides, including e.g., irregularities ("roughness") in the landslide sliding surface, fractures, tension cracks, small pressure ridges and hummocks, and pebbles, cobbles, boulders and blocks (Blair and McPherson, 1999) typical of landslide deposits. The typical pixel size of a modern SAR image ranges from 3.0 $m \times 3.0$ m to 16.0 $m \times 16.0$ m (Table 1), much smaller or comparable to the size (area) of most of the small, shallow landslides. We conclude that the wavelengths of the SAR sensors, and the area covered by pixels of modern SAR sensors are – in principle – adequate to detect landslides, and their internal elements.

We next consider that SAR sensors – differently from e.g., optical, passive sensors – are active sensors that illuminate the ground with pulses of electromagnetic radiation whose characteristics are known. The amplitude and phase of the echo (Sec. 4) depend (among others) on the geometrical and physical (mass) characteristics of the ground surface, which are assumed to be different in landslide areas and in stable terrain. Measured by amplitude, the terrain backscatter depends on the ground dielectric constant, related e.g., to soil moisture, and the surface roughness. Variations in coherence depend on the properties of the ground surface, including the presence or absence of vegetation and on target displacement. All these properties can be related to the presence (or absence) of a landslide, and interpretation of their spatial and temporal variations can be used to detect and map landslides.

By comparing amplitude-based or coherence-based products in different parts of a SAR image having and not having landslides (e.g., Singhroy, 1995; Czuchlewski et al., 2003; Balz and Liao, 2010; Furuta and Sawada, 2013), or the changes in SAR amplitude or coherence in images taken before (pre-event) and after (post-event) a landslide (e.g., Suga and Konishi, 2012; Konishi and Suga, 2017; Mondini et al., 2019), a trained investigator can detect and map the landslides. Variations in the SAR phase can also measure geometric (topographic) changes in the ground surface caused by the movement of a landslide (Sec. 5.2.1). We conclude that, although we cannot "see" landslides in SAR imagery in the same way we see them in optical imagery, the available SAR imagery are – in principle – well suited to detect and map landslides, even allowing for strategies not (easily) feasible with optical imagery. We maintain that the simultaneous sampling of different properties of the ground surface measured by the SAR amplitude and phase should facilitate landslide failure detection and mapping.

Analysis of the literature (Sections 5.1 and 5.2) revealed that – in practice – the exploitation of this theoretical framework for landslide failure detection and mapping using SAR imagery requires a number of steps which, for descriptive purposes, can be loosely grouped into two main phases: (i) a first phase aimed at the preparation of SAR imagery (image "pre-processing"), and (ii) a second phase for the SAR image classification.

For amplitude-based approaches (Sec. 5.1), pre-processing transforms the amplitude recorded in a SAR image into a measure of the surface backscatter, which can then be used to discriminate different surface classes, including landslides and some of their internal features (e.g., the source or depletion area, the transport and depositional areas). The image can be corrected radiometrically and geometrically, multi-looked, filtered, co-registered to other images, and projected or ortho-rectified. Multi-polarimetric imagery allows for more complex transformations because it carries more information on the surface characteristics. In principle, it should be possible to describe the backscatter from a complex ground surface as the sum of simpler components, including backscatter from the bare ground e.g., a landslide, and the volumetric backscatter of a forest, facilitating the detection of landslides and stable terrain. For interferometry-based products (Sec. 5.2.1), pre-processing transforms the phase changes in surface (ground) displacements caused by a moving landslide, or other geological processes (e.g., an earthquake, volcanic activity, subsidence). It includes an accurate co-registration of an image pair, usually multi-looking, eventually Earth curvature and topographic phase subtraction, and filtering, in particular when the interferogram is unwrapped. For coherence-based products (Sec. 5.2.2), pre-processing consists of the calculation of coherence or its changes, and it requires images co-registration, usually multi-looking, and eventually Earth curvature and topographic phase subtraction. Coherence is sensitive to changes in the position and the physical properties of the scatterers.

Image classification is then executed through visual or numerical approaches, in which qualitative (heuristic, visual interpretation) or quantitative (statistical modelling) classification of the surface spectral response, or of changes in the surface response, are used to detect and map the landslides. Investigators have mainly (i) interpreted visually tonal changes, and their spatial variations, of amplitude-based and coherence-based products; (ii) considered the statistical properties of amplitude-based and coherence-based products in different land cover classes (including landslides) and their spatial and temporal changes; or (iii) used interferometry-based products to measure surface displacements. Interestingly, and with the exception of the interferometry-based products, the qualitative and the quantitative approaches are both similar to the corresponding classification approaches used for landslide detection and mapping using optical (multi-spectral) imagery (Guzzetti et al., 2012). And similar to the optical-based approaches, they require expert interpretation and geomorphological insight, mainly to resolve ambiguities (radiometric or morphological convergence), and to reduce the number of commission (false positive) and omission (false negative)

errors.

8.2. Research framework

Since the first application of SAR imagery for landslide failure detection and characterisation (Singhroy, 1995; Vargas Cuervo, 1997), significant research progresses have been made, driven manly by the increased availability of (mostly satellite) SAR imagery (Fig. 5), and the increased image processing capabilities, due to faster computer and more effective software. Despite the progress, a number of issues remain open. Here, we discuss four of them, which we consider most relevant and broad.

First, we note the lack of rigorous, theoretical "radiation-matter" models that explain the interaction between the incoming SAR radiation and the geometrical and physical surface structures of different landslide types, at the sampled resolution, and specifically the geometrical structure and dielectric constant of the ground (i.e., the "matter"), at the sampled resolution (Ulaby et al., 1982; Watanabe et al., 2016). Such models will allow for the prediction of the backscatter, providing the theoretical basis for the detection of landslide failures and for the discrimination of unstable ("landslide") from stable ("non landslide") terrain, assuming that the backscattering responses will be different in landslide and in stable areas. Similar models exist e.g., for forests (Durden et al., 1989; Pulliainen et al., 1994), for inundated forested areas (Richards et al., 1987), for bare soil parameters, including soil moisture content (Altese et al., 1996; MirMazloumi and Sahebi, 2016; Ghorbanian et al., 2019), for agricultural areas (Sun et al., 2019).

Likewise, there is a lack of rigorous, theoretical models to explain how coherence changes where and when a landslide failure occurs, depending on the landslide type and extent, the ground dielectric constant (dependent on soil moisture) and surface roughness, and on the land cover type. We further note the lack of systematic measurements and comparisons of the backscattering properties, coherence, and their geographical and temporal changes, in landslide areas, for different landslide types and extents, and in different physiographical settings. We recommend investing in the development of theoretical models able to predict the backscattering and coherence responses to different landslide types, and in the design and execution of systematic campaigns to obtain accurate measurements of the surface backscatter in landslide and stable areas, to test the models (Table 2).

Second, we note that despite the high potential (Bruzzone et al., 2004; Nielsen et al., 2015), and the clear advantages in determining the surface backscattering properties and their changes (useful for the image visual interpretation and for machine-learning based methods), use of fully-polarimetric imagery remains uncommon in the literature. The main reason is the limited availability of fully-polarimetric (satellite) imagery, a result of the lack of systematic acquisitions. Given the technical problems that prevented the deployment of multi-channel SAR sensors on satellites (Bruzzone et al., 2004), access to fully-polarimetric imagery was limited to airborne systems until the advent of ALOS (2006), Radarsat-2 and TerraSAR-X (2007), and later on ALOS-2 (2014) (Table 1). Even the mentioned fully-polarimetric satellites have often been operated in single or dual polarisation modes, for power supply and coverage reasons (Nielsen et al., 2015), further limiting the availability of fully-polarimetric (satellite) imagery. Despite the inherent difficulties, we encourage the exploitation and testing of fully-polarimetric imagery for landslide failure detection and mapping (Table 2).

Third, we note that studies that experimented with the combination or the "fusion" of SAR products with other imagery or products are rare (e.g., Singhroy, 1995; Singhroy et al., 1998; Mwaniki et al., 2017). The experiments were limited to the combined, visual interpretation of optical-based and SAR-based products. In the experiments, the optical and SAR images were processed separately for information and feature extraction; then, the separate classifications were combined through some decision, heuristic processes (Pohl and Van Genderen, 1998). The approach proves useful, but has drawbacks, the most important of which is the need for optical imagery, which prevents the use of the approach at night (Mondini et al., 2019) or during a rainfall event e.g., a typhoon (Mondini and Chang, 2014; Tay et al., 2020). We speculate that other fusion approaches can be used to improve the quality of the statistical classifications obtained exploiting SAR products.

Learning from what is currently done exploiting optical imagery (Guzzetti et al., 2012; Scaioni et al., 2014; Zhong et al., 2020), we encourage investigators to experiment with the pixel level combination of images acquired in different bands, to fully exploit their different backscattering scales and measures (Table 2), although we acknowledge it may be difficult and costly to obtain imagery of different types for the same area, or for the same landslide event. In this context, pixel-based or terrain-based landslide susceptibility models (Reichenbach et al., 2018) can be used as "geomorphological filters" in probabilistic frameworks to reduce the number of false classification positives, excluding areas where landslides cannot, or are not likely to occur given the local settings (Mondini and Chang, 2014; Mondini et al., 2017; Alvioli et al., 2018).

A yet different way of combining SAR-based products is exemplified in the work of Ge et al. (2019), who used Linear Discriminant Analysis (LDA) to combine coherence, intensity difference, and the correlation coefficient between pre-event and post-event images, exploiting the different sensitivities of the products to ground changes caused by the landslide failures. Similarly, Ohki et al. (2020) combined Pauli matrix elements (Cloude and Pottier, 1996), coherence, phase variation (Fielding et al., 2005), and DEM derived slope and curvature using a Random Forest machine learning algorithm.

As expected (Rossi et al., 2010; Reichenbach et al., 2018), application of the LDA resulted in a reduction in the number of false positives (commission errors), compared to the two single techniques, and the Random Forest algorithm increased the overall quality of the classification, with a Cohen's $k = 0.7$ (Cohen, 1960). To the best of our knowledge, these are the only attempts to combine statistically different detection techniques.

We encourage investigators to perform similar combination experiments using DInSAR products, to understand whether the image classification would benefit from information on surface displacements (Table 2). For large displacement dynamics landslides, information on surface displacement can be obtained using pixel-offset tracking approaches (Furuta and Tomiyama, 2008; Casu et al., 2011; Manconi et al., 2014; Singleton et al., 2014; Sun and Muller, 2016; Darvishi et al., 2018). Considering the peculiar statistical distributions of the pixels in the SAR images, we further recommend experimenting with more sophisticated machine learning techniques (Table 2).

Ultimately, our literature analysis (Sec. 6) revealed that (i) the combinations of product types and investigation methods (55) exceeded the number of published articles (54) (Sec. 3) and, (ii) the numerical predominance of threshold-based (40) and visual-based (34) classification methods (Fig. 7) was mainly determined by two articles (Mondini et al., 2019; Burrows et al., 2020). Such considerable fragmentation of research results may be indicative of the narrow interest of individual investigators to experiment and test their own detection or mapping techniques on single sites or areas of limited extent, without any strategic interest or effort towards a common, shared result – like in other fields of landslide research (e.g., Reichenbach et al., 2018) – or it may outline the lack of a consensus in the research community on the "best" or optimal methods to detect and map landslide failures using SAR imagery.

To explore further the advantages and limitations of the solutions proposed in the literature, and of new possible solutions, we recommend a more systematic use of the SAR imagery. In particular, we encourage repeating the detection and mapping experiments using qualitative and quantitative methods in different geomorphological settings, not just where the setting is favourable, and also using different imagery. This will help identifying a portfolio of solutions best suited for different conditions and data availability (Table 2). The extended use of the SAR

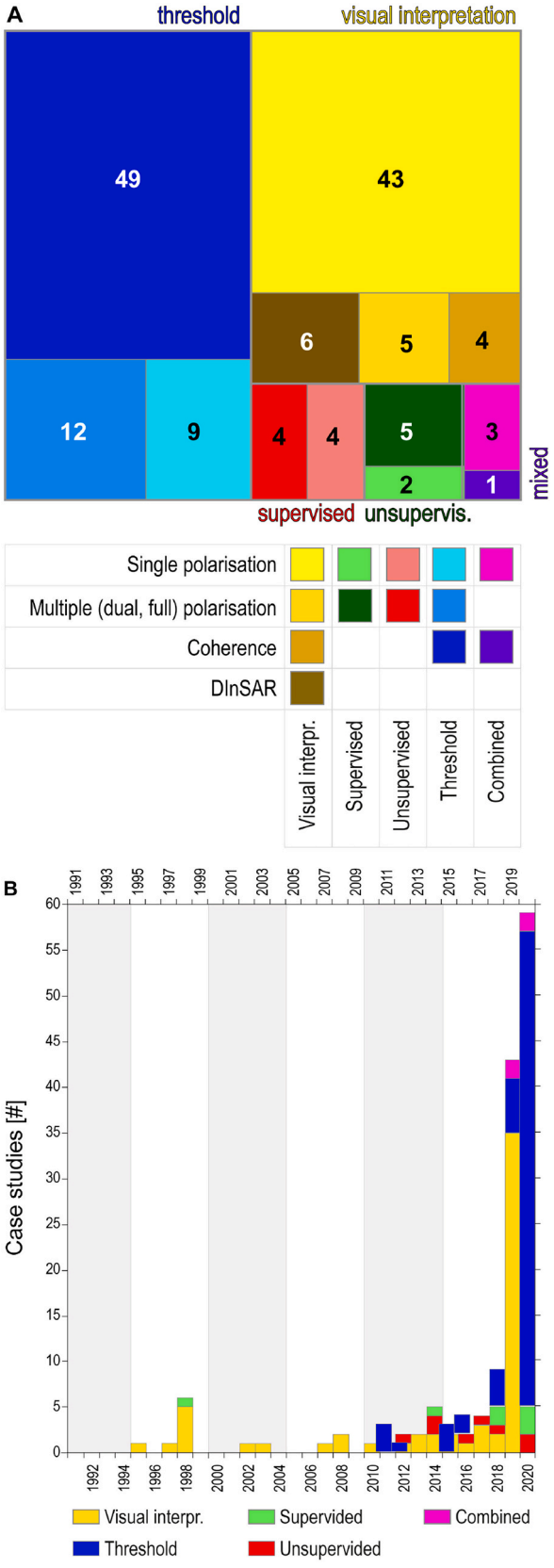

Fig. 7. Analysis of classification methods in the literature database. (A) Tree chart shows the number of case studies that used (i) the type of classification methods (visual interpretation, unsupervised, supervised, threshold-based) or a combination of them, and (ii) the pre-processing approaches (single polarisation, multiple (dual and full) polarisation, coherence, DInSAR), and of the combined approaches. (B) Bar chart shows the temporal trend of the classification methods.

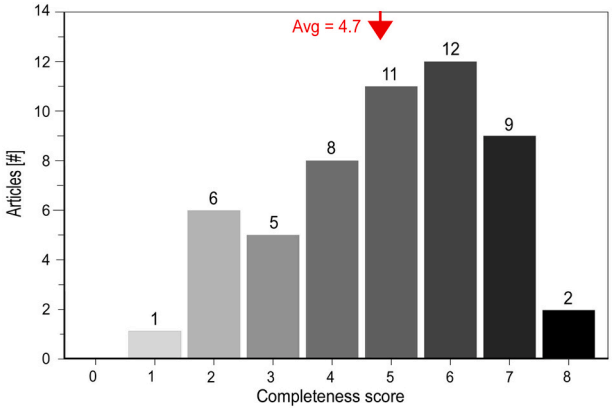

Fig. 8. Completeness of information in the 54 articles in the literature database. Bar chart shows the number of articles (y-axis) per each completeness score (x-axis). The darker the grey bar, the higher the completeness of the information.

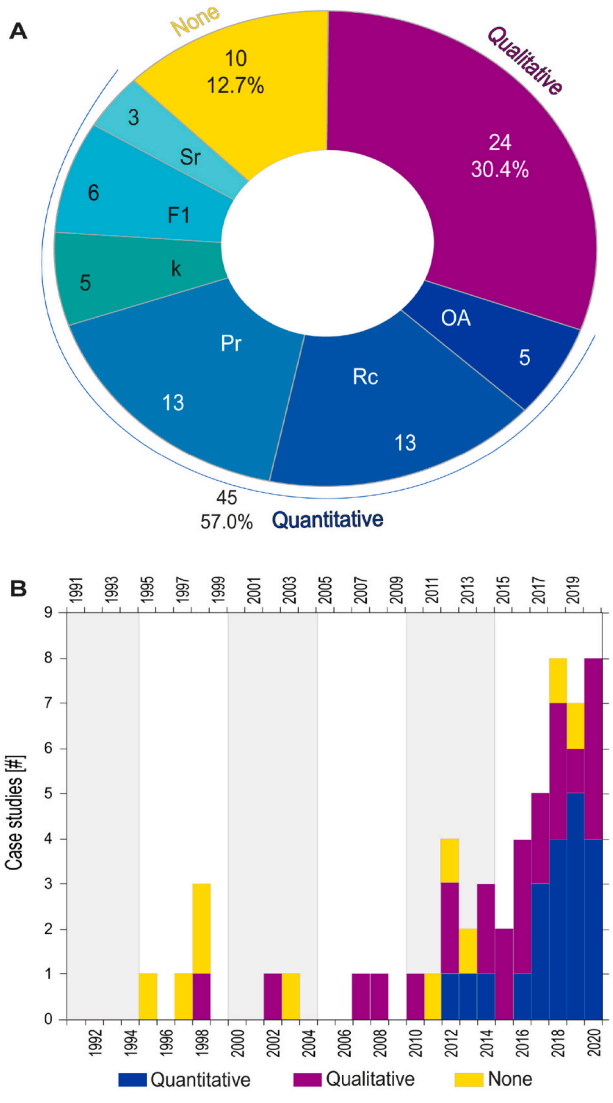

Fig. 9. Quality analysis. (A) Number and percentage of validation approaches. None, no validation performed. Qualitative, qualitative (visual) validation. Quantitative validation: OA, Overall accuracy index; Rc, Recall; Pr, Precision; k, Cohen *k*; F1, F1 score; Sr, Success rate. (B) Temporal distribution of application of the different validation methods.

imagery should be assisted by physically-based and empirical ("data driven") models describing the properties of the pixels inside (and outside) the landslides. The models should consider the natural (e.g., surface geometry and structure, surface deformation, soil moisture, landcover type) and the engineering (e.g., wavelength, pixel size, channels) aspects. Besides contributing to obtain better detection and landslide inventory maps, the effort may help understanding whether the current resolutions in the different channels, spectral bands (Table 1) are the best options to detect and map landslides, or if more advanced technologies are needed. We stress that this research is highly multi- and inter-disciplinary, as it requires expertises in different areas, including e.g., signal processing, geomorphology, numerical modelling.

8.3. Operational framework

Our literature review revealed a consensus that SAR imagery can be used effectively to detect and map landslide failures of different types and sizes, and in a variety of environmental and physiographical settings. Then, a question to ask is whether scope exists for operational services for landslide detection and mapping based on SAR imagery. A second question to ask is if, or to what extent, such services are operationally feasible with the imagery, technologies, and tools currently available, or that will soon be available.

8.3.1. Scope for SAR-based landslide detection and mapping services

In 2012, Guzzetti and his co-workers (Guzzetti et al., 2012) estimated that landslide maps covered less than 1% of the slopes in the landmasses, and concluded that, despite their relevance for landslide hazard and risk assessment, landslide maps were unexpectedly rare. We argue that the situation has not improved significantly in the last nine years, despite global community efforts to compile and organise geographical landslide information (Van Den Eeckhaut and Hervás, 2012; Kirschbaum et al., 2015; Tanyaş et al., 2017; Herrera et al., 2018; Mateos et al., 2020), and the increased availability of optical satellite imagery, of high and very high resolution digital elevation and terrain models, of improved image classification models, and of enhanced visualisation software, which, all together, can be exploited to identify landslides and to prepare landslide inventory maps (Guzzetti et al., 2012; Casagli et al., 2016; Zhong et al., 2020).

We stress that knowing where landslides are, where and when they occur, and how they evolve in space and time, is of primary importance for the construction and the validation of landslide susceptibility models and maps (Reichenbach et al., 2018) and of advanced spatio-temporal hazard models (Lombardo et al., 2020), for the validation of LEWSs forecasts (Piciullo et al., 2018; Guzzetti et al., 2020), to investigate the complex interactions between landslides, climate, and environmental changes (Sidle and Ochiai, 2006; Crozier, 2010; Gariano and Guzzetti, 2016), to document and study the effects of severe geophysical (Tanyaş et al., 2017; Williams et al., 2018; Fan et al., 2019) and meteorological (Mondini et al., 2014; Konishi and Suga, 2017, 2018a; Tay et al., 2020) events on physical landscapes and social environments (Brabb, 1991; Glade et al., 2005; Kjekstad and Highland, 2009), and to study the evolution of landscapes dominated by mass-wasting processes (Hovius et al., 1997; Malamud et al., 2004a, 2004b; Guzzetti et al., 2009; Bucci et al., 2016; Vanmaercke et al., 2017).

Part of the problem related to the rapid detection of landslides for e.g., the validation of LEWS forecasts (Guzzetti et al., 2020) or the timely production of landslide maps for emergency response and rescue operations (Inyang and Daniels, 2009) following a major seismic (Yun et al., 2015; Esposito et al., 2018; Williams et al., 2018; Aimaiti et al., 2019; Ge et al., 2019; Uemoto et al., 2019; Burrows et al., 2020) or meteorological (Mondini et al., 2014; Konishi and Suga, 2017, 2018a; Tay et al., 2020) event, lays in the difficulty of obtaining suitable optical imagery free of clouds that can be interpreted visually, or classified automatically or semi-automatically (Joyce et al., 2009; Guzzetti et al., 2012; Torres et al., 2012; Casagli et al., 2016).

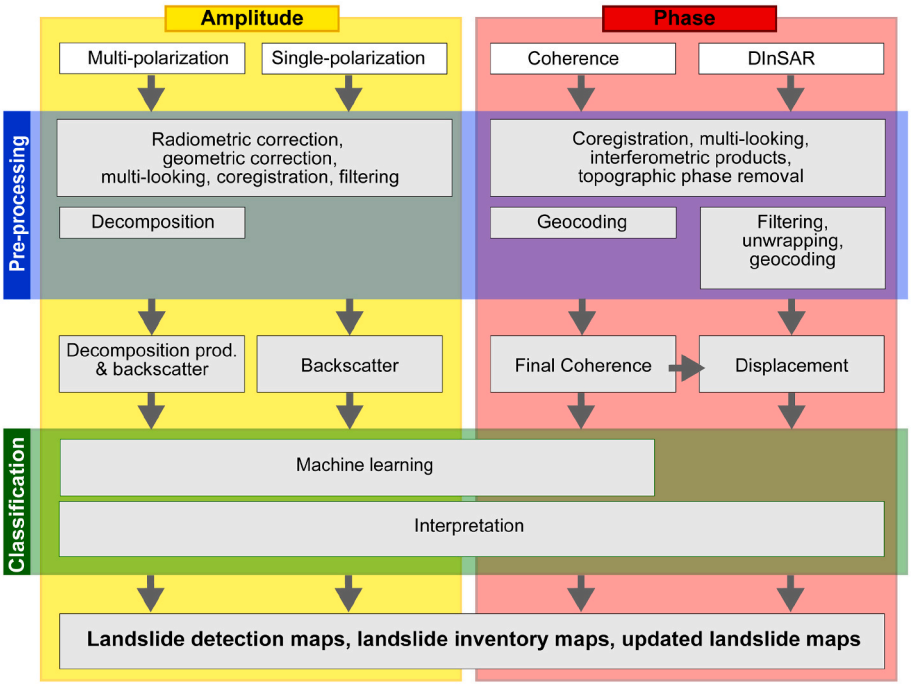

Fig. 10. Logical framework for the detection and mapping of landslide failures – where a landslide failure is the single most significant movement episode in the history of a landslide (Hungr et al., 2014) – and of landslide failure events i.e., populations of one or many landslides in an area caused by a single trigger (Guzzetti et al., 2012), using SAR imagery. Yellow rectangle shows amplitude domain, and red rectangle shows phase domain. Blue rectangle shows pre-processing approaches, and green rectangle shows classification methods. See text for explanation. (For interpretation of the references to colour in this figure legend, the reader is referred to the web version of this article.)

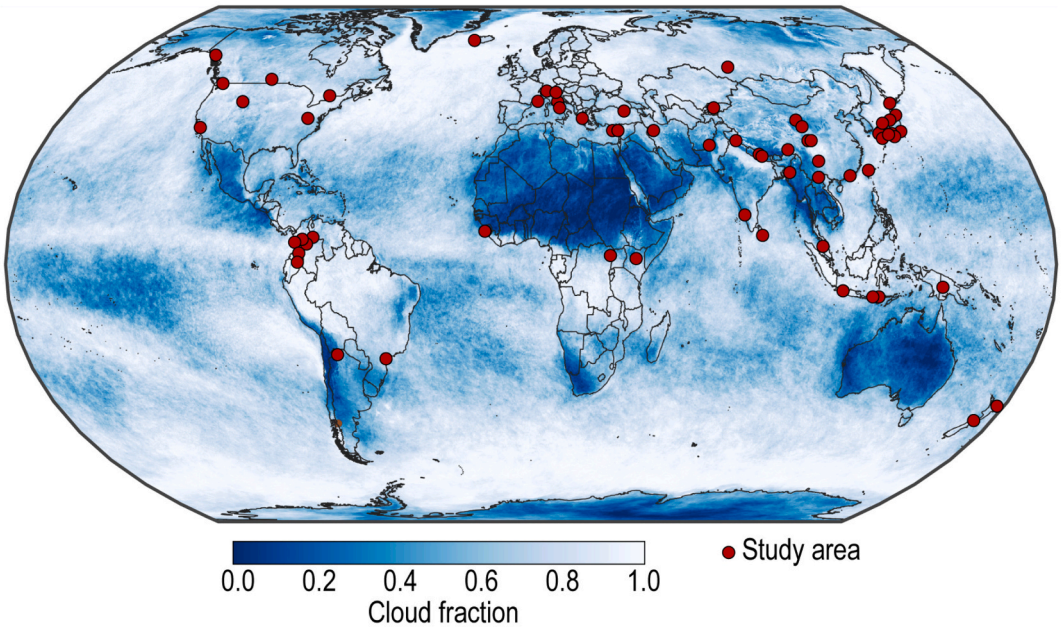

Fig. 11. Map shows global monthly (September 2019) cloud fraction i.e., the percentage of each 0.1° × 0.1° pixel covered by clouds, measured daily using the Moderate Resolution Imaging Spectroradiometer (MODIS) aboard NASA's Terra and Aqua satellites (NASA Earth Observations, 2020). Colours range from blue (no clouds) to white (totally cloudy). Red dots show locations of study areas in the literature database. See Fig. 2. Map uses Equal Earth map projection (EPSG:8857). Credits: Imagery by Reto Stockli, NASA's Earth Observatory (NEO), using data provided by the MODIS Atmosphere Science Team, NASA Goddard Space Flight Center. (For interpretation of the references to colour in this figure legend, the reader is referred to the web version of this article.)

Clouds can cover about 70% of the Earth's surface (Stubenrauch et al., 2013). Fig. 11 shows the global cloud fraction map for September 2019 i.e., the fraction of any given area that was cloudy, on average. One sees that the majority of the landmasses where landslides are known to exist or to be abundant were covered by clouds. Analysis of the NASA Earth Observations website for the 20-year period between February 2000 and July 2020 (*https://earthobservatory.nasa.gov/global-maps/MODAL2_M_CLD_FR*) reveals that similar monthly cloud coverage fractions are the norm. Mondini et al. (2019) showed that the large, 6-km long, rainfall and snowmelt induced landslide of 16 December 2017 in Villa Santa Lucia, Central Chile, was not visible to optical satellites until January 2018, due to the persistent cloud coverage.

Similarly, Robinson et al. (2019) calculated that 40% of the global population at risk from earthquakes are obscured from optical satellite view for more than three days between June and August. However, the ESA C-band Sentinel-1 image used by Mondini et al. (2019) and Burrows et al. (2020) to detect seismically-induced landslides triggered by the

Iburi earthquake in southern Hokkaido, Japan, on 6 September 2018 at 03:08 JST (5 September 2018 at 18:08 UTC), was taken during the night at 5:41 JST (5 September 2018 at 20:41 UTC) i.e., only about two and half hours from the earthquake. In principle, this could have allowed for the preparation of a preliminary landslide map within hours from the earthquake even in the absence of daylight.

We argue that satellite SAR sensors, given their ability to penetrate the clouds ("all-weather" sensors), and to work in presence and absence of daylight ("day-and-night" sensors), represent – and will represent in the near future – the best available technological option for the rapid detection of landslides from space, and for the rapid preparation of event landslide inventory maps when optical images are not available. We further argue that there is scope for operational, satellite-based SAR services for the timely detection of event landslides, and for the production and updating of landslide inventory maps.

8.3.2. Feasibility of operational landslide detection and mapping services

The design, implementation, and operation of SAR-based landslide detection and mapping services is not trivial, and it requires the preliminary definition of user, system, and service requirements. One has to decide on the general (e.g., LEWS forecast evaluation, rapid disaster response, long term map update) and the specific (e.g., landslide failure detection, landslide mapping) goals of the service, on the optimal and the acceptable (minimum) product delivery time or period (e.g., hours, days, weeks, months), and on the geographical scale, or scales, of the system (e.g., covering a single slope, a catchment, a region, a nation, a continent, or the entire globe). One has also to evaluate the sustainability of the system in terms of current and future (foreseeable) availability of adequate SAR imagery, of the feasibility of exploiting SAR imagery of different types (e.g., different bands, acquisition modes, area coverage), and of the availability and characteristics of ancillary information, including e.g., DEM, geological and land-cover maps. Additional key issues to consider include the availability of (i) adequate computer processing and storage facilities "(hardware"), of (ii) suited processing, modelling, and visualisation tools ("software"), and of (iii) the personnel, who has to cover multiple expertise. The design of a SAR-based, operational landslide detection and mapping service is not within the scope of the article, but in the following we provide some general consideration.

We first consider the image availability issue. Inspection of Fig. 5A reveals that availability of SAR satellites, and thus we assume of SAR imagery, has increased over the years. The revolutionary Capella (Space, 2020) and (ICEYE, 2020) missions promising few hours repeat passes will soon be fully operational. New missions, including e.g., SAOCOM-1b (European Space Agency, 2020e), TerraSAR-X Next Generation (European Space Agency, 2020f), COSMO-SkyMed Second Generation (European Space Agency, 2020a), NISAR (NASA Jet Propulsion Laboratory, 2020b), will further increase the availability of SAR imagery in the near future. We conclude that image availability is not (and will not be) an issue for the design and the implementation of operational, SAR-based landslide detection and mapping services.

However, we note that most of the past, existing and planned missions were designed, and are and will be operated mainly – if not entirely – for interferometric scopes and related products, including multi-temporal DInSAR-based motion measurements and deformation analyses. This limits their use for landslide failure detection and mapping purposes. We note that the ESA Sentinel 1 mission, which currently operates with the Interferometric Wide (IW) swath as the main acquisition mode designed chiefly for interferometric analyses, given its temporal resolution and the constant, scheduled, repeat passes (every six days, considering two satellites), proves very well suited for operational landslide detection and mapping.

We next discuss the image processing (hardware and software) issue. Considering the ESA Sentinel-1 mission as a reliable, economic, stable, medium-to-long term source of SAR imagery adequate for landslide detection and mapping, we tested the time necessary for the pre-processing of a pair of pre-event and a post-event ESA Sentinel-1 images, with a 250 km swath and covering an area of $\approx$ 41,250 km^2. Using an off-the-shelf, high-end laptop computer equipped with one i7 core 2.8 $GHz \times 8$ processor, 64 GB RAM, one TB disk, running Ubuntu 18.04, and the Sentinel Application Platform (SNAP) release 7.0 application software, the pre-processing phase took less than 10 min. Optional terrain correction took additional 2:30 min. The entire process used about 20 GB disk space. Similarly, pre-processing of five bursts of a single polarimetric channel – sufficient to detect a landslide event over a large area – took less than six minutes and used less than 20 GB of disk space. Phase unwrapping was more time consuming, with the total time dependent on various settings and the extent of the area, but was less than 150 min (2.5 h) using the statistical-cost, network-flow algorithm implemented in SNAPHU (Chen and Zebker, 2000), with tiles of 100 pixels. This simple experiment revealed that the processing of SAR imagery necessary for the detection and mapping of landslide failures in areas of several thousands square kilometres (i.e., a large catchment, a nation) is well within the capabilities of modest computer (hardware and software) facilities. Extrapolating the result to a larger number of images covering a larger or much larger area, or even to the entire globe, or other, better performing processing chains, is not linear (nor trivial), but we maintain that it is computationally and economically feasible with the existing computer technology (e.g., the European Space Agency's Geohazard Exploitation Platform (GEP) (https://geohazards-tep.eo.esa.int/#!)) at low to reasonable costs.

Ultimately, we consider the human factor. Landslide detection and mapping is by itself a difficult and uncertain operation, that requires expert investigators (Guzzetti et al., 2012). Use of SAR imagery is also not trivial; and it requires specific image processing tools and skills. The complexity of the SAR imagery, the variety of approaches and methods that can be used for image pre-processing and classification, and for the validation of the mapping results, and the complex – and often not considered – relationships between the image characteristics and the classification methods, also require expert investigators. We maintain that – to be successful – an operational landslide detection and mapping service has to relay on a team capable of covering multiple expertise including e.g., remote sensing, visualisation, machine learning, geomorphology, landslide interpretation and analysis. With this respect, such services are candidates for the "convergence" approach emerging in medicine and in other research fields (National Research Council, 2014; Sharp et al., 2016; Sharp and Hockfield, 2017).

We recommend designing and implementing operational, SAR-based services. We expect this to contribute to prepare landslide maps and to mitigate landslide hazards and the associated risks.

8.4. Perspective

The legacy of 26 years of experimentation in the use of remotely-sensed SAR imagery to detect and map single landslide failures, or populations of triggered landslides in broad areas, is a portfolio of technical solutions encompassing different image pre-processing approaches (Sec. 6.6) and classification methods (Sec. 6.7, Fig. 10), using different types of imagery (Sec. 7). The different technical solutions were tested in a variety of morphological, geological, climatic, seismic, and land-cover settings (Sec. 6.2, Fig. 2), and for different landslide types and triggering factors (Sec. 6.4). Despite the undisputed progress, important challenges remain to be faced for the future.

First, our review of the literature revealed that standards for the effective detection and mapping of landslides using remotely sensed SAR imagery are missing. Standards for the assessment of the quality of the obtained results and mapping products are also lacking. We stress that the lack of standards limits the possibility to compare different detection and mapping methods. As indicated by Guzzetti (2005), this can reduce the credibility and usefulness of the results, with potential negative consequences on the derivative products and analyses, including e.g., landslide inventory maps (Guzzetti et al., 2012), landslide susceptibly

modelling and zonation (Reichenbach et al., 2018), landslide hazard and risk evaluations (Guzzetti et al., 2012), and the validation of geographical landslide early warning systems (Piciullo et al., 2018; Guzzetti et al., 2020). We encourage investigators to converge towards and to adopt common, standard approaches and methods for landslide detection and mapping, and for their quality evaluation. We expect that this will raise the credibility and usefulness of the related products.

Second, the literature review also revealed that the full potential and the inherent limitations of the existing framework for landslide detection and mapping using airborne or satellite SAR imagery (Fig. 10) has not been explored fully. Reasons are manifold, including (i) the lack of a systematic use of SAR imagery, a result of the costs and inherent difficulty in obtaining images with specific, suited characteristics; (ii) the apparent difficulty of treating SAR imagery, a result of the scarcity and the cost of adequate software; and (iii) a lack of accuracy in reporting the results of the experiments in the literature. The ESA, C-band Sentinel1-A, B, with the programmed continuity until 2030 with the launch of Sentinel1-C and 1-D, and the JAXA, L-band ALOS-2 missions, are already fostering the use of SAR imagery for landslide detection and mapping (Fig. 5). We recommend that the recent governmental (e.g., the Argentinian SAOCOM, the Canadian Radarsat Constellation Mission) and private (e.g., the Cappella Space constellation) missions, and the foreseen private (e.g., Iceye) and governmental (e.g., the Italian COSMO-SkyMed Second Generation, the German TerraSAR-X Next Generation, and the joint U.S.A. and India NISAR) missions adopt flexible data acquisition programs and distribution policies. We expect this to favour the further expansion of the use of SAR imagery for landslide detection and mapping.

Improved desktop software, including e.g., the open source Delft Institute of Earth Observation and Space Systems (Doris) of Delft University of Technology, the ESA Polarimetric SAR Data Processing and Educational Tool (PolSARPro), the REdar Tools (RAT), the NASA JPL Repeat Orbit Interferometry PACkage (ROI_PAC), the ESA SentiNel Application Platform (SNAP), dedicated libraries and toolboxes for the Python high-level programming language, the commercial DIAPASON®, ENVI® SARscape®, IMAGINE Radar Mapping®, and Gamma® packages, as well as large computing platforms, including the ESA Thematic Exploitation Platform (TEP), are also favouring a wider use of SAR imagery for landslide detection and mapping, making it accessible even to investigators who are not experts in radar technology and image processing. However, we also note some counter-trends, such as the recent (July 31, 2020) shutdown of the Research and User Support (RUS) Copernicus Service, launched in September 2017 "*to prevent technical and knowledge barriers affecting user's uptake of Copernicus datasets*" (*https://rus-training.eu/news/rus-virtual-machines-switch-off-on-july-31*).

Third, in their critical analysis of conventional and – at the time – innovative and emerging techniques for landslide mapping based on remote sensing imagery and technologies, Guzzetti et al. (2012) argued that a crucial problem was the lack of experienced image interpreters, and that adequate training in landslide detection and mapping was difficult to obtain. When using SAR imagery, the problem is even more severe because of the inherent difficulty in handling the radar images – compared to optical images, and because the interpretation criteria that are consolidated for optical images (Guzzetti et al., 2012) are poorly defined for SAR images. We encourage investigators to define and test image interpretation criteria specific for SAR-based products. This should not be too difficult when the images are ortho-rectified using high and very-high resolution terrain elevation data, obtained by exploiting e.g., LiDAR technology. We further recommend that investigators define interpretation criteria for landslide detection and mapping based on SAR imagery. This will facilitate the production of homogeneous and comparable landslide detection and mapping products, and will favour the integration of landslide information obtained from different remote sensing and spatial technologies.

Fourth, Guzzetti et al. (2012) further argued that "*a combination of satellite, aerial and terrestrial remote sensing data represented the optimal solution for landslide detection and mapping, in different physiographic, climatic and land cover conditions*". Before 2012, only 13 articles (24.1%) in our literature database had been published, indicating that SAR imagery was only seldom used for landslide detection and mapping, and chiefly for experimenting the use of the technology (e.g., Singhroy, 1995; Vargas Cuervo, 1997; Singhroy et al., 1998; Chorowicz et al., 1998). The situation has changed significantly in the recent years, and today SAR imagery represents a mature, effective option for landslide detection and mapping. SAR imagery can be exploited to measure accurately the ground displacement caused by a strong earthquake and its cascading effects, including large populations of triggered landslides (Ge et al., 2019; Aimaiti et al., 2019; Ohki et al., 2020; Burrows et al., 2020; Adriano et al., 2020; Jung and Yun, 2020) shortly after they have occurred, it can help detect and map recent landslide dams, which can be breached, causing inundations (Konishi and Suga, 2018b; Mondini et al., 2019), and it can be exploited to map landslides and inundated areas caused by a typhoon, hurricane, or intense rainfall event within hours from their occurrence (Mondini, 2017; Adriano et al., 2020). With this respect, SAR-based multi-hazard detection and mapping platforms are a realistic opportunity for a more integrated effort in disaster risk management.

Ultimately, in the literature – and to a large extent in the daily practice – we note a persistent lack of interest in landslide mapping, both as a source of information for research activities, and for land and emergency management. We expect that the progress made and the expected developments in the exploitation of SAR imagery will facilitate greatly the timely detection and mapping of different types of landslides in a variety of morphological, geological, climatic and land cover context.

We encourage the broad community of research investigators, practitioners, engineers, planners, rescue operators, risk and disaster managers, and decision makers, who exploit – routinely or occasionally – landslide data and information, to take advantage of the new opportunities offered by remote sensing technologies, and specifically of SAR imagery and related processing techniques, for enhanced landslide detection and mapping. In this sense, a combined mission, optical and SAR, dedicated to landslide detection and mapping is a realistic opportunity today, as demonstrated by Mondini et al. (2019). We stress that the current scientific knowledge and technological capabilities are sufficient to design, implement, and manage landslide detection and mapping services operating on different geographical and temporal scales in many areas of the world. Global coverage services are also within the existing capabilities. For the latter, what is missing is a realistic cost-benefit analysis of a dedicated landslide detection and mapping mission, and a lively institutional interest driven by strong demand from a large user community.

9. Conclusions

In this work, we examined almost 26 years of literature on the use of Synthetic Aperture Radar (SAR) imagery for the detection and mapping of landslide failure events and populations of event landslides published in peer-reviewed journals. Critical analysis of the results of 147 case studies in 70 study areas in all continents, except Antarctica (Fig. 2), and the analysis of the existing and foreseen SAR missions and their technical and operational characteristics (Table 1), allows for the following general considerations.

SAR imagery taken from aerial or satellite platforms, used appropriately and with the necessary processing and visualisation software tools – which nowadays are widely available – represents a valuable asset for the efficient detection and mapping of individual landslides, and of populations of landslides of different types and sizes in broad areas, and in a variety of physiographical settings. The existing knowledge on landslide processes and the current technological capabilities are adequate to design, implement, and manage landslide detection and

mapping services operating on different geographical and temporal scales, including global coverage services. Such services may prove particularly useful for the validation of geographical landslide early warning systems (LEWSs) (Piciullo et al., 2018; Guzzetti et al., 2020; Calvello et al., 2020), including global rainfall-induced landslide nowcasting systems (Kirschbaum and Stanley, 2018). The unique ability of microwave radar sensors of seeing through the clouds ("all-weather"), and to work in presence and absence of daylight ("day-and-night"), makes SAR sensors particularly well suited for the rapid detection and mapping of landslides caused by large geophysical (Aimaiti et al., 2019; Burrows et al., 2019; Ge et al., 2019; Park and Lee, 2019; Burrows et al., 2020; Jung and Yun, 2020; Adriano et al., 2020) or meteorological (Suga and Konishi, 2012; Mondini and Chang, 2014; Konishi and Suga, 2018a; Tay et al., 2020; Adriano et al., 2020) events, when timely information on landslide occurrence is required e.g., for rescue operations and emergency management, as well as to construct multi-temporal landslide inventories which can be used for advanced landslide hazard modelling (Lombardo et al., 2020).

Despite 26 years of undisputed progress, a number of theoretical, research, and operational challenges remain to be faced for the effective use of SAR imagery for landslide detection and mapping. Table 2 lists the main recommendations that emerge from our review of the literature to meet the open challenges. For the challenges to be met, standards and shared best practices are needed to assess and hopefully reduce uncertainty, ensure repeatability and reproducibility, avoid misinterpretation and facilitate comparisons.

Our last conclusion originates from the evidence that, despite landslides being frequent and abundant, widely distributed, and locally extremely dangerous and destructive events caused by different geophysical and meteorological triggers, landslide events remain among the less documented natural events. This has negative consequences on our collective ability to understand landslide phenomena and their spatial and temporal evolution, to predict landslides and their impact, to measure the vulnerability to landslides of various elements at risk, including the population, and to mitigate landslide risk. Nowadays, knowledge and technology are available to document landslide events shortly after they have occurred. We encourage landslide scientists and professionals to take advantage of the opportunity and focus on systematic landslide detection and mapping projects. We expect this to attract institutional and private interests, which could support the common goal of improving our collective ability to systematically detect landslide events and their consequences, a key step towards the reduction of landslide risk.

Data availability

Data extracted from the 54 articles in the literature database are organised in tabular format in an "xlsx" file, available as ancillary material associated to the article.

Acknowledgments and credits

We are grateful to two anonymous reviewers and to the editor for their constructive comments that helped us to prepare a better structured and more informative article. The work was partially funded by the UKRI Natural Environment Research Council's and UK Government's Department for International Development's Science for Humanitarian Emergencies and Resilience research programme (grant number NERC/DFID NE/P000649/1), and by the Spanish Ministry of Economy and Competitiveness through the DEMOS project "Deformation monitoring using Sentinel-1 data" (Ref: CGL2017-83704-P). In the article, use of trade, product, or firm names is for descriptive purposes only and does not imply endorsement by the authors or their Institutions.

Declaration of Competing Interest

The authors declare that they have no known competing financial interests or personal relationships that could have appeared to influence the work reported in this paper.

Appendix A. List of abbreviations

Acronyms and abbreviations used in the text.

Acronym	Description
ARIA	Advanced Rapid Imaging and Analysis
ASI	Agenzia Spaziale Italiana, Italian Space Agency (Italy)
AUC	Area and the ROC Curve
CNN	Convolutional Neural Network
CCRS	Canada Centre for Remote Sensing (Canada)
CECL	Co-Event Coherence Loss
CONAE	Comisión Nacional de Actividades Espaciales (Argentina)
CLC	Corine Land Cover
CSA	Canadian Space Agency (Canada)
DBC	Differential Backscattering Coefficient
DInSAR	Differential Interferometry Synthetic Aperture Radar
DP	Dual Polarisation
DSGSD	Deep-Seated Gravitational Slope Deformation
ESA	European Space Agency (Europe)
FP	Full Polarisation
FPR	False Positive Rate
GIS	Geographical Information System
GSD	Ground Sampling Distance
HSI	Hue, Saturation, Intensity
LDA	Linear Discriminant Analysis
LOS	Line of Sight
MITI	Ministry of International Trade and Industry (Japan)
NASA	National Aeronautics and Space Administration (USA)
NASDA	National Space Development Agency (Japan)
NDSI	Normalised Difference Scattering Index

(*continued on next page*)

(*continued*)

Acronym	Description
NDVI	Normalised Differential Vegetation Index
NEO	NASA Earth Observations
NIED	Japanese National Research Institute for Earth Science and Disaster Resilience
OA	Overall accuracy
PECI	Post-Event Coherence Increase
PSS	Polarimetric Scattering Similarity
RCS	Radar Cross Section
RGB	Red, Green, Blue
ROC	Receiver Operating Characteristic curve
SAR	Synthetic Aperture Radar
SNAPHU	Statistical-Cost, Network-Flow Algorithm for Phase Unwrapping
SP	Single Polarisation
STA	Science and Technology Agency (Japan)
TEP	ESA Thematic Exploitation Platform

Appendix B. List of variables

Variables used in the text.

Variable	Unit	Description
$\overline{\alpha}$	scalar	Weighted average scattering
β	°/rad	Synthetic beam width
β_0	scalar	Radar brightness coefficient
k	cm^{-1}	Wavenumber
γ	scalar	Interferometric coherence
λ	cm	Wavelength
ϕ	°/rad	Phase
π	scalar	Pi
RVI	scalar	Radar *V*egetation Index
σ_0	scalar, dB	Backscattering coefficient
τ	s	π phase change
$\mathscr{A}$	scalar	Anisotropy
A_L	m^2	Landslide area
$[T_{2,3}]$	$unit^2$	Coherence matrix, for dual (2) and full (3) polarisation systems
$[C_{2,3}]$	$unit^2$	Covariance matrix, for dual (2) and full (3) polarisation systems
E	units	Expected value
H	scalar	Entropy
M_s	scalar	Earthquake surface wave magnitude
M_w	scalar	Earthquake moment magnitude
P_H	scalar	Pedestal height
R	m	Distance between the target and the receiving antenna
RVI	scalar	Radar *V*egetation Index
Θ_i	°/rad	Look angle
V_L	m^3	Landslide volume
S	units	Sinclair scattering matrix

Appendix C. Supplementary data

Supplementary data to this article can be found online at https://doi.org/10.1016/j.earscirev.2021.103574.

References

Adriano, B., Yokoya, N., Miura, H., Matsuoka, M., Koshimura, S., 2020. A semiautomatic pixel-object method for detecting landslides using multitemporal alos-2 intensity images. Remote Sens. 12, 561. https://doi.org/10.3390/rs12030561.

Aimaiti, Y., Liu, W., Yamazaki, F., Maruyama, Y., 2019. Earthquake-induced landslide mapping for the 2018 Hokkaido Eastern Iburi earthquake using Palsar-2 data. Remote Sens. 11 https://doi.org/10.3390/rs11202351.

Altese, E., Bolognani, O., Mancini, M., Troch, P.A., 1996. Retrieving soil moisture over bare soil from ERS 1 Synthetic Aperture Radar Data: sensitivity analysis based on a theoretical surface scattering model and field data. Water Resour. Res. 32, 653–661. https://doi.org/10.1029/95WR03638.

Alvioli, M., Mondini, A.C., Fiorucci, F., Cardinali, M., Marchesini, I., 2018. Topography-driven satellite imagery analysis for landslide mapping. Geomatics Nat. Hazards Risk 9, 544–567. https://doi.org/10.1080/19475705.2018.1458050.

Antonini, G., Ardizzone, F., Cardinali, M., Galli, M., Guzzetti, F., Reichenbach, P., 2002. Surface deposits and landslide inventory map of the area affected by the 1997 Umbria–Marche earthquakes. Boll. Della Soc. Geol. Ital. 121, 843–853.

Badoux, A., Andres, N., Techel, F., Hegg, C., 2016. Natural hazard fatalities in Switzerland from 1946 to 2015. Nat. Hazards Earth Syst. Sci. 16, 2747–2768. https://doi.org/10.5194/nhess-16-2747-2016.

Bai, Z., Fang, S., Gao, J., Zhang, Y., Jin, G., Wang, S., Zhu, Y., Xu, J., 2020. Could vegetation index be derive from synthetic aperture radar? – the linear relationship between interferometric coherence and NDVI. Sci. Rep. 10 https://doi.org/10.1038/s41598-020-63560-0.

Balz, T., Liao, M., 2010. Building-damage detection using post-seismic high-resolution SAR satellite data. Int. J. Remote Sens. 31, 3369–3391. https://doi.org/10.1080/01431161003727671.

Barboux, C., Delaloye, R., Lambiel, C., 2014. Inventorying slope movements in an alpine environment using DInSAR. Earth Surf. Process. Landf. 39, 2087–2099. https://doi.org/10.1002/esp.3603.

Bardi, F., Frodella, W., Ciampalini, A., Bianchini, S., Del Ventisette, C., Gigli, G., Fanti, R., Moretti, S., Basile, G., Casagli, N., 2014. Integration between ground based and satellite Sar data in landslide mapping: the san fratello case study. Geomorphology 223, 45–60. https://doi.org/10.1016/j.geomorph.2014.06.025.

Barra, A., Monserrat, O., Mazzanti, P., Esposito, C., Crosetto, M., Mugnozza, G.S., 2016. First insights on the potential of sentinel-1 for landslides detection. Geomatics Nat. Hazards Risk 7, 1874–1883. https://doi.org/10.1080/19475705.2016.1171258.

Basil, R., Bosi, V., Galadini, F., Galli, P., Meghraoui, M., Messina, P., Moro, M., Sposato, A., 1998. The Colfiorito earthquake sequence of September-October 1997: surface breaks and seismotectonic implications for the Central Apennines (Italy). J. Earthq. Eng. 2, 291–302. https://doi.org/10.1080/13632469809350323.

Berardino, P., Fornaro, G., Lanari, R., Sansosti, E., 2002. A new algorithm for surface deformation monitoring based on small baseline differential SAR interferograms. IEEE Trans. Geosci. Remote Sens. 40, 2375–2383. https://doi.org/10.1109/TGRS.2002.803792.

Bhattacharya, A., Mukherjee, K., 2017. Review on InSAR based displacement monitoring of indian himalayas: issues, challenges and possible advanced alternatives. Geocarto Int. 32, 298–321. https://doi.org/10.1080/10106049.2016.1140820.

Bianchini, S., Cigna, F., Righini, G., Proietti, C., Casagli, N., 2012. Landslide hotspot mapping by means of persistent scatterer interferometry. Environ. Earth Sci. 67, 1155–1172. https://doi.org/10.1007/s12665-012-1559-5.

Blair, T.C., McPherson, J.G., 1999. Grain-size and textural classification of coarse sedimentary particles. J. Sediment. Res. 69, 6–19. https://doi.org/10.2110/jsr.69.6.

Bovenga, F., Nutricato, R., Refice, A., Wasowski, J., 2006. Application of multi-temporal differential interferometry to slope instability detection in urban/peri-urban areas. Eng. Geol. 88, 218–239. https://doi.org/10.1016/j.enggeo.2006.09.015.

Bovenga, F., Belmonte, A., Refice, A., Pasquariello, G., Nutricato, R., Nitti, D., Chiaradia, M., 2018. Performance analysis of satellite missions for multi-temporal Sar interferometry. Sensors 18, 1359. https://doi.org/10.3390/s18051359.

Bozzano, F., Gambino, P., Prestininzi, A., Scarascia Mugnozza, G., Valenti, G., 1998. Ground effects induced by the Umbria-Marche earthquakes of September-October 1997, Central Italy. In: Moore, D., Hungr, O. (Eds.), Engineering Geology - A Global View from the Pacific Rim. Proceedings of the 8th International Congress of the IAEG, Vancouver, 21–25 September 1998, Balkema, Vancouver, 21–25 September, vol. 1998, pp. 825–830.

Brabb, E.E., 1991. The world landslide problem. Episodes 14, 52–61.

Brabb, E.E., Harrod, B.L. (Eds.), 1989. Landslides: Extent and Economic Significance: Proceedings 28th International Geological Congress Symposium on Landslides. Rotterdam and Brookfield, Vermont.

Bruzzone, L., Marconcini, M., Wegmuller, U., Wiesmann, A., 2004. An advanced system for the automatic classification of multitemporal SAR images. IEEE Trans. Geosci. Remote Sens. 42, 1321–1334. https://doi.org/10.1109/TGRS.2004.826821.

Bucci, F., Santangelo, M., Cardinali, M., Fiorucci, F., Guzzetti, F., 2016. Landslide distribution and size in response to Quaternary fault activity: the Peloritani Range, NE Sicily, Italy. Earth Surf. Process. Landf. 41, 711–720. https://doi.org/10.1002/esp.3898.

Burrows, K., Walters, R.J., Milledge, D., Spaans, K., Densmore, A.L., 2019. A new method for large-scale landslide classification from satellite radar. Remote Sens. 11 https://doi.org/10.3390/rs11030237.

Burrows, K., Walters, R.J., Milledge, D., Densmore, A.L., 2020. A systematic exploration of satellite radar coherence methods for rapid landslide detection. Nat. Hazards Earth Syst. Sci. 20, 3197–3214. https://doi.org/10.5194/nhess-20-3197-2020.

Calò, F., Ardizzone, F., Castaldo, R., Lollino, P., Tizzani, P., Guzzetti, F., Lanari, R., Angeli, M.G., Pontoni, F., Manunta, M., 2014. Enhanced landslide investigations through advanced DInSAR techniques: the Ivancich case study, Assisi, Italy. Remote Sens. Environ. 142, 69–82. https://doi.org/10.1016/j.rse.2013.11.003.

Calvello, M., Devoli, G., Freeborough, K., Gariano, S.L., Guzzetti, F., Kirschbaum, D., Nakaya, H., Robbins, J., Stähli, M., 2020. LandAware: a new international network on landslide early warning systems. Landslides. https://doi.org/10.1007/s10346-020-01548-7.

Canadian Space Agency, 2020. Radarsat Constellation Mission. https://www.asc-csa.gc.ca/eng/satellites/radarsat/default.asp.

Cantalloube, H., Nahum, C., 2000. How to compute a multi-look SAR image? In: Harris, R.A., Ouwehand, L. (Eds.), SAR workshop: CEOS Committee on Earth Observation Satellites, p. 635.

Carper, W.J., 1990. The use of intensity-hue-saturation transformations for merging spot panchromatic and multispectral image data. Photogramm. Eng. Remote. Sens. 56, 459–467.

Casagli, N., Cigna, F., Bianchini, S., Hölbling, D., Füreder, P., Righini, G., Conte, S.D., Friedl, B., Schneiderbauer, S., Iasio, C., Vlcko, J., Greif, V., Proske, H., Granica, K., Falco, S., Lozzi, S., Mora, O., Arnaud, A., Novali, F., Bianchi, M., 2016. Landslide mapping and monitoring by using radar and optical remote sensing: examples from the EC-FP7 project SAFER. Remote Sens. Appl. 4, 92–108. https://doi.org/10.1016/j.rsase.2016.07.001.

Casagli, N., Frodella, W., Morelli, S., Tofani, V., Ciampalini, A., Intrieri, E., Raspini, F., Rossi, G., Tanteri, L., Lu, P., 2017a. Spaceborne, UAV and ground-based remote sensing techniques for landslide mapping, monitoring and early warning. Geoenviron. Disasters 4, 9. https://doi.org/10.1186/s40677-017-0073-1.

Casagli, N., Tofani, V., Morelli, S., Frodella, W., Ciampalini, A., Raspini, F., Intrieri, E., 2017b. In: Mikoš, M., Arbanas, Ž., Yin, Y., Sassa, K. (Eds.), Remote sensing techniques in landslide mapping and monitoring, keynote lecture. Advancing Culture of Living with Landslides, Springer International Publishing, pp. 1–19.

Casu, F., Manconi, A., Pepe, A., Lanari, R., 2011. Deformation time-series generation in areas characterized by large displacement dynamics: the SAR amplitude pixel-offset SBAS technique. IEEE Trans. Geosci. Remote Sens. 49, 2752–2763.

Chang, K.T., Chiang, S.H., Chen, Y.C., Mondini, A.C., 2014. Modeling the spatial occurrence of shallow landslides triggered by typhoons. Geomorphology 208, 137–148. https://doi.org/10.1016/j.geomorph.2013.11.020.

Chen, C.W., Zebker, H.A., 2000. Network approaches to two-dimensional phase unwrapping: intractability and two new algorithms. J. Opt. Soc. Am. 17, 401–414. https://doi.org/10.1364/JOSAA.17.000401.

Chen, R.F., Chang, K.J., Angelier, J., Chan, Y.C., Deffontaines, B., Lee, C.T., Lin, M.L., 2006. Topographical changes revealed by high-resolution airborne LiDAR data: the 1999 Tsaoling landslide induced by the Chi–Chi earthquake. Eng. Geol. 88, 160–172. https://doi.org/10.1016/j.enggeo.2006.09.008.

Chen, X., Sun, Q., Hu, J., 2018. Generation of complete SAR geometric distortion maps based on DEM and Neighbor Gradient Algorithm. Appl. Sci. 8, 2206. https://doi.org/10.3390/app8112206.

Cheng, Yizong, 1995. Mean shift, mode seeking, and clustering. In: IEEE Transactions on Pattern Analysis and Machine Intelligence, 17, pp. 790–799. https://doi.org/10.1109/34.400568.

Chigira, M., Wang, W.N., Furuya, T., Kamai, T., 2003. Geological causes and geomorphological precursors of the Tsaoling landslide triggered by the 1999 Chi-Chi earthquake, Taiwan. Eng. Geol. 68, 259–273. https://doi.org/10.1016/S0013-7952(02)00232-6.

Chorlton, L.B., 2007. Generalized Geology of the World: Bedrock Domains and Major Faults in GIS Format: A Small-Scale World Geology Map with an Extended Geological Attribute Database.

Chorowicz, J., Scanvic, J., Rouzeau, O., Cuervo, G.V., 1998. Observation of recent and active landslides from SAR ERS-1 and JERS-1 imagery using a stereo-simulation approach: example of the Chicamocha valley in Colombia. Int. J. Remote Sens. 19, 3187–3196. https://doi.org/10.1080/014311698214253.

Ciampalini, A., Cigna, F., Ventisette, C.D., Moretti, S., Liguori, V., Casagli, N., 2012. Integrated geomorphological mapping in the north-western sector of Agrigento (Italy). J. Maps 8, 136–145.

Ciampalini, A., Raspini, F., Bianchini, S., Frodella, W., Bardi, F., Lagomarsino, D., Traglia, F.D., Moretti, S., Proietti, C., Pagliara, P., Onori, R., Corazza, A., Duro, A., Basile, G., Casagli, N., 2015. Remote sensing as tool for development of landslide databases: the case of the Messina province (Italy) geodatabase. Geomorphology 249, 103–118. https://doi.org/10.1016/j.geomorph.2015.01.029.

Cigna, F., Bianchini, S., Casagli, N., 2013. How to assess landslide activity and intensity with persistent scatterer interferometry (psi): the psi-based matrix approach. Landslides 10, 267–283. https://doi.org/10.1007/s10346-012-0335-7.

Cloude, S., 1992. Uniqueness of Target Decomposition Theorems in Radar Polarimetry. volume 350 of *NATO ASI Series (Series C: Mathematical and Physical Sciences)*. chapter 5, pp. 267–296. https://doi.org/10.1007/978-94-010-9243-2_10.

Cloude, S.R., Papathanassiou, K.P., 1998. Polarimetric Sar interferometry. IEEE Trans. Geosci. Remote Sens. 36, 1551–1565. https://doi.org/10.1109/36.718859.

Cloude, S.R., Pottier, E., 1996. A review of target decomposition theorems in radar polarimetry. IEEE Trans. Geosci. Remote Sens. 34, 498–518.

Cohen, J., 1960. A coefficient of agreement for nominal scales. Educ. Psychol. Meas. 20, 37–46. https://doi.org/10.1177/001316446002000104.

Comaniciu, D., Meer, P., 2002. Mean shift: a robust approach toward feature space analysis. IEEE Trans. Pattern Anal. Mach. Intell. 24, 603–619.

Comisión Nacional de Actividades Espaciales, 2020. Saocom. https://www.argentina.gob.ar/ciencia/conae/misiones-espaciales/saocom. (Accessed 4 June 2020).

Crozier, M.J., 2010. Deciphering the effect of climate change on landslide activity: a review. Geomorphology 124, 260–267. https://doi.org/10.1016/j.geomorph.2010.04.009.

Cruden, D., Varnes, D., 1996. Landslide types and processes. In: Turner, A.K., Schuster, R. L. (Eds.), Landslides: Investigation and Mitigation, vol. 247. National Academy Press, Washington, D.C, pp. 36–75.

Czuchlewski, K.R., Weissel, J.K., Kim, Y., 2003. Polarimetric synthetic aperture radar study of the Tsaoling landslide generated by the 1999 Chi-Chi earthquake, Taiwan. J. Geophys. Res. Earth Surf. 108 https://doi.org/10.1029/2003JF000037 n/a–n/a.

Darvishi, M., Schlögel, R., Bruzzone, L., Cuozzo, G., 2018. Integration of PSI, MAI, and intensity-based sub-pixel offset tracking results for landslide monitoring with X-Band corner reflectors – Italian Alps (Corvara). Remote Sens. 10, 409. https://doi.org/10.3390/rs10030409.

Del Ventisette, C., Ciampalini, A., Manunta, M., Calò, F., Paglia, L., Ardizzone, F., Mondini, A.C., Reichenbach, P., Mateos, R.M., Bianchini, S., García-Moreno, I., Füsi, B., Deák, Z., Rádi, K., Graniczny, M., Kowalski, Z., Piatkowska, A., Przylucka, M., Retzo, H., Strozzi, T., Colombo, D., Mora, O., Sánchez, F., Herrera Garcia, G., Moretti, S., Casagli, N., Guzzetti, F., 2013. Exploitation of large archives of ERS and ENVISAT C-Band SAR data to characterize ground deformations. Remote Sens. 5, 3896–3917. https://doi.org/10.3390/rs5083896.

Densmore, A.L., Anderson, R.S., McAdoo, B.G., Ellis, M.A., 1997. Hillslope evolution by bedrock landslides. Science 275, 369–372.

Department of Space, Indian Space Research Organisation, I, 2020. Risat-1. https://www.isro.gov.in/Spacecraft/risat-1.

Donezar, U., De Blas, T., Larrañaga, A., Ros, F., Albizua, L., Steel, A., Broglia, M., 2019. Applicability of the multitemporal coherence approach to Sentinel-1 for the detection and delineation of burnt areas in the context of the Copernicus Emergency Management Service. Remote Sens. 11, 2607. https://doi.org/10.3390/rs11222607.

Dowling, C.A., Santi, P.M., 2013. Debris flows and their toll on human life: a global analysis of debris-flow fatalities from 1950 to 2011. Nat. Hazards. https://doi.org/10.1007/s11069-013-0907-4.

Durden, S.L., van Zyl, J.J., Zebker, H.A., 1989. Modeling and observation of the radar polarization signature of forested areas. IEEE Trans. Geosci. Remote Sens. 27, 290–301.

El-Darymli, K., McGuire, P., Gill, E., Power, D., Moloney, C., 2014. Understanding the significance of radiometric calibration for synthetic aperture radar imagery. In: 2014

IEEE 27th Canadian Conference on electrical and Computer Engineering (CCECE), pp. 1–6.
Esposito, E., Porfido, S., Simonelli, A.L., Mastrolorenzo, G., Iaccarino, G., 2000. Landslides and other surface effects induced by the 1997 Umbria–Marche seismic sequence. Eng. Geol. 58, 353–376. https://doi.org/10.1016/S0013-7952(00)00035-1.
Esposito, G., Mondini, A.C., Marchesini, I., Reichenbach, P., Salvati, P., Rossi, M., 2018. An example of SAR-derived image segmentation for landslides detection. PeerJ. Preprints 6. https://doi.org/10.7287/peerj.preprints.27212v2 e27212v2.
Esposito, G., Marchesini, I., Mondini, A.C., Reichenbach, P., Rossi, M., Sterlacchini, S., 2020. A spaceborne SAR-based procedure to support the detection of landslides. Nat. Hazards Earth Syst. Sci. 20, 2379–2395. https://doi.org/10.5194/nhess-20-2379-2020.
European Environment Agency, 1992. CORINE Land Cover A European Community Project, 1 (Luxembourg).
European Environment Agency, 2007. CLC2006 Technical Guidelines, 1. Publications Office, Luxembourg.
European Space Agency, 2020a. COSMO-SkyMed Second Generation. https://directory.eoportal.org/web/eoportal/satellite-missions/c-missions/cosmo-skymed-second-generation.
European Space Agency, 2020b. Geometry Glossary. https://earth.esa.int/handbooks/asar/CNTR5-5.html.
European Space Agency, 2020c. Geophysical Measurements. https://sentinel.esa.int/web/sentinel/user-guides/sentinel-1-sar/product-overview/geophysical-measurements.
European Space Agency, 2020d. Polarimetric Decompositions. https://earth.esa.int/web/polsarpro/polarimetry-tutorial.
European Space Agency, 2020e. SAOCOM (SAR Observation and Communications Satellite). https://directory.eoportal.org/web/eoportal/satellite-missions/s/saocom.
European Space Agency, 2020f. TSX-NG (TerraSAR-X Next Generation). https://directory.eoportal.org/web/eoportal/satellite-missions/t/tsx-ng.
Fan, X., Scaringi, G., Korup, O., West, A.J., van Westen, C.J., Tanyaş, H., Hovius, N., Hales, T.C., Jibson, R.W., Allstadt, K.E., Zhang, L., Evans, S.G., Xu, C., Li, G., Pei, X., Xu, Q., Huang, R., 2019. Earthquake-induced chains of geologic hazards: patterns, mechanisms, and impacts. Rev. Geophys. 83 https://doi.org/10.1029/2018RG000626.
Farina, P., Colombo, D., Fumagalli, A., Marks, F., Moretti, S., 2006. Permanent scatterers for landslide investigations: outcomes from the esa-slam project. Eng. Geol. 88, 200–217. https://doi.org/10.1016/j.enggeo.2006.09.007.
Fell, R., 1994. Landslide risk assessment and acceptable risk. Can. Geotech. J. 31, 261–272. https://doi.org/10.1139/t94-031.
Ferretti, A., Prati, C., Rocca, F., 2001. Permanent scatterers in SAR interferometry. IEEE Trans. Geosci. Remote Sens. 39, 8–20. https://doi.org/10.1109/36.898661.
Ferretti, A., Monti-Guarnieri, A., Prati, C., Rocca, F., Massonnet, D., 2007. InSAR Principles: Guidelines for SAR Interferometry Processing and Interpretation. In: http://www.esa.int/About_Us/ESA_Publications/InSAR_Principles_Guidelines_for_SAR_Interferometry_Processing_and_Interpretation_br_ESA_TM-19.
Ferretti, A., Fumagalli, A., Novali, F., Prati, C., Rocca, F., Rucci, A., 2011. A new algorithm for processing interferometric data-stacks: SqueeSAR. IEEE Trans. Geosci. Remote Sens. 49, 3460–3470.
Fielding, E.J., Talebian, M., Rosen, P.A., Nazari, H., Jackson, J.A., Ghorashi, M., Walker, R., 2005. Surface ruptures and building damage of the 2003 bam, iran, earthquake mapped by satellite synthetic aperture radar interferometric correlation. J. Geophys. Res. Solid Earth 110. https://doi.org/10.1029/2004JB003299.
Freeman, A., Durden, S.L., 1993. Three-component scattering model to describe polarimetric NDVI data. In: Mott, H., Boerner, W.M. (Eds.), Radar Polarimetry, International Society for Optics and Photonics. SPIE, pp. 213–224. https://doi.org/10.1117/12.140618.
Freeman, A., Durden, S.L., 1998. A three-component scattering model for polarimetric SAR data. IEEE Trans. Geosci. Remote Sens. 36, 963–973. https://doi.org/10.1109/36.673687.
Frost, V.S., Stiles, J.A., Shanmugan, K.S., Holtzman, J.C., 1982. A model for radar images and its application to adaptive digital filtering of multiplicative noise. IEEE Trans. Pattern Anal. Mach. Intell. PAMI-4, 157–166. https://doi.org/10.1109/TPAMI.1982.4767223.
Froude, M.J., Petley, D.N., 2018. Global fatal landslide occurrence from 2004 to 2016. Nat. Hazards Earth Syst. Sci. 18, 2161–2181. https://doi.org/10.5194/nhess-18-2161-2018.
Fujiwara, S., Nakano, T., Morishita, Y., Kobayashi, T., Yarai, H., Une, H., Hayashi, K., 2019. Detection and interpretation of local surface deformation from the 2018 Hokkaido Eastern Iburi Earthquake using ALOS-2 SAR data. Earth Planets Space 71. https://doi.org/10.1186/s40623-019-1046-2.
Furukawa, K., Kaibori, M., Kubota, T., Jitousono, T., Gonda, Y., Sugihara, S., Hayashi, S. I., Ikeda, A., Araki, Y., Kashiwabara, Y., 2009. Debris disasters caused by heavy rainfall around Hofu City in Yamaguchi Prefecture on July 21, 2009. Journal of the Japan Society of Erosion. Control. Eng. 62, 62–73. https://doi.org/10.11475/sabo.62.3_62.
Furuta, R., Sawada, K., 2013. Case study of landslides recognition using dual/quad polarization data of ALOS/PALSAR. In: Conference Proceedings of 2013 Asia-Pacific Conference on Synthetic Aperture Radar (APSAR), pp. 481–484.
Furuta, R., Tomiyama, N., 2008. A Study of Detection of Landslide Disasters Due to the Pakistan Earthquake Using ALOS Data. In: https://www.isprs.org/proceedings/2011/ISRSE-34/211104015Final00320.pdf.
Gabriel, A.K., 2002. A simple model for SAR azimuth speckle, focusing, and interferometric decorrelation. IEEE Trans. Geosci. Remote Sens. 40, 1885–1889. https://doi.org/10.1109/TGRS.2002.802456.
García-Davalillo, J.C., Herrera, G., Notti, D., Strozzi, T., Álvarez-Fernández, I., 2014. DInSAR analysis of ALOS PALSAR images for the assessment of very slow landslides: the Tena Valley case study. Landslides 11, 225–246. https://doi.org/10.1007/s10346-012-0379-8.
Gariano, S.L., Guzzetti, F., 2016. Landslides in a changing climate. Earth Sci. Rev. 162, 227–252. https://doi.org/10.1016/j.earscirev.2016.08.011.
Ge, P., Gokon, H., Meguro, K., Koshimura, S., 2019. Study on the intensity and coherence information of high-resolution ALOS-2 SAR images for rapid massive landslide mapping at a pixel level. Remote Sens. 11 https://doi.org/10.3390/rs11232808.
Ghorbanian, A., Sahebi, M.R., Mohammadzadeh, A., 2019. Optimization approach to retrieve soil surface parameters from single-acquisition single-configuration SAR data. Compt. Rendus Geosci. 351, 332–339. https://doi.org/10.1016/j.crte.2018.11.005.
Giardini, D., Gruenthal, G., Shedlock, K., Zhang, P., 2003. The GSHAP global seismic hazard map. In: Lee, W., Kanamori, H., Jennings, P., Kisslinger, C. (Eds.), International Handbook of Earthquake and Engineering Seismology, Part b. first ed.. Academic Press. volume 81 of International Geophysics, pp. 1233–1239. https://doi.org/10.1016/S0074-6142(03)80188-2.
Giordan, D., Hayakawa, Y., Nex, F., Remondino, F., Tarolli, P., 2018. Review article: the use of remotely piloted aircraft systems (RPASs) for natural hazards monitoring and management. Nat. Hazards Earth Syst. Sci. 18, 1079–1096. https://doi.org/10.5194/nhess-18-1079-2018.
Given, L.M., 2008. The SAGE encyclopedia of qualitative research methods. In: Los Angeles. Sage Publications, Calif.
Glade, T., Anderson, M., Crozier, M.J. (Eds.), 2005. Landslide Hazard and Risk, 1. John Wiley & Sons.
Gokceoglu, C., Sezer, E., 2009. A statistical assessment on international landslide literature (1945–2008). Landslides 6, 345. https://doi.org/10.1007/s10346-009-0166-3.
Goodfellow, I., Bengio, Y., Courville, A., 2016. Deep Learning. MIT Press.
Goorabi, A., 2020. Detection of landslide induced by large earthquake using Insar coherence techniques – northwest zagros, Iran. Egypt. J. Remote Sens. Space Sci. 23, 195–205. https://doi.org/10.1016/j.ejrs.2019.04.002.
Grahn, T., Jaldell, H., 2017. Assessment of data availability for the development of landslide fatality curves. Landslides 14, 1113–1126. https://doi.org/10.1007/s10346-016-0775-6.
Griffith, D.A., 1987. Spatial Autocorrelation. A Primer. Association of American Geographers, Washington, DC.
Griffith, D.A., Chun, Y., 2016. Spatial autocorrelation and uncertainty associated with remotely-sensed data. Remote Sens. 8 https://doi.org/10.3390/rs8070535.
Guthrie, R.H., 2013. Socio-Economic Significance. Canadian Technical Guidelines and Best Practices Related to Landslides: A National Initiative for Loss Reduction. Technical Report. Geological Survey of Canada. https://doi.org/10.4095/292241.
Guzzetti, F., 2005. Landslide Hazard and Risk Assessment. Ph. Thesis. Mathematich-Naturwissenschaftlichen Fakultat, Rheinischen Friedrich-Wilhelms-Universitat Bonn. Bonn.
Guzzetti, F., 2021. On the prediction of landslides and their consequences. In: Sassa, K., Mikoš, M., Sassa, S., Bobrowsky, P.T., Takara, K., Dang, K. (Eds.), Understanding and Reducing Landslide Disaster Risk: Volume 1 Sendai Landslide Partnerships and Kyoto Landslide Commitment, 1. Springer International Publishing, Cham, pp. 3–32. https://doi.org/10.1007/978-3-030-60196-6_1.
Guzzetti, F., Cardinali, M., Reichenbach, P., Carrara, A., 2000. Comparing landslide maps: a case study in the upper Tiber River Basin, Central Italy. Environ. Manag. 25, 247–263. https://doi.org/10.1007/s002679910020.
Guzzetti, F., Ardizzone, F., Cardinali, M., Rossi, M., Valigi, D., 2009. Landslide volumes and landslide mobilization rates in Umbria, Central Italy. Earth Planet. Sci. Lett. 279, 222–229. https://doi.org/10.1016/j.epsl.2009.01.005.
Guzzetti, F., Mondini, A.C., Cardinali, M., Fiorucci, F., Santangelo, M., Chan, K.T., 2012. Landslide inventory maps: New tools for an old problem. Earth Sci. Rev. 112, 42–66. https://doi.org/10.1016/j.earscirev.2012.02.001.
Guzzetti, F., Gariano, S.L., Peruccacci, S., Brunetti, M.T., Marchesini, I., Rossi, M., Melillo, M., 2020. Geographical landslide early warning systems. Earth Sci. Rev. 200, 102973. https://doi.org/10.1016/j.earscirev.2019.102973.
Haydn, R., Dalke, G., Henkel, J., Bare, J., 1982. Application of the ihs color transform to the processing of multisensor data and image enhancement, in: Proceedings of the International Symposium on Remote Sensing of Arid and Semi-Arid Lands, Cairo, Egypt. Ann. Arbor. Mich. 599–616.
Herrera Garcia, G., Fernández-Merodo, J.A., Mulas, J., Pastor, M., Luzi, G., Monserrat, O., 2009. A landslide forecasting model using ground based SAR data: the Portalet case study. Eng. Geol. 105, 220–230. https://doi.org/10.1016/j.enggeo.2009.02.009.
Herrera Garcia, G., Gutiérrez, F., García-Davalillo, J.C., Guerrero, J.J., Notti, D., Galve, J. P., Fernández-Merodo, J.A., Cooksley, G., 2013. Multi-sensor advanced DInSAR monitoring of very slow landslides: the Tena Valley case study (Central Spanish Pyrenees). Remote Sens. Environ. 128, 31–43. https://doi.org/10.1016/j.rse.2012.09.020.
Herrera Garcia, G., García López Davalillo, J.C., Fernández-Merodo, J.A., Béjar Pizarro, M., Allasia, P., Lollino, P., Lollino, G., Guzzetti, F., Lvarez Fernandez, M.I., Manconi, A., Duro, J., Sánchez, C., Iglesias, R., 2017. The differential slow moving dynamic of a complex landslide: multi-sensor monitoring. In: Mikoš, M., Vilimek, V., Yin, Y., Sassa, K. (Eds.), 4th World Landslide Forum, Advancing Culture of Living with Landslides, Lubljana, 2017. Springer International Publishing, Cham, pp. 219–225. https://doi.org/10.1007/978-3-319-53498-5_25.

Herrera, G., Mateos, R.M., García-Davalillo, J.C., Grandjean, G., Poyiadji, E., Maftei, R., Filipciuc, T.C., Jemec Auflič, M., Jež, J., Podolszki, L., Trigila, A., Iadanza, C., Raetzo, H., Kociu, A., Przyłucka, M., Kułak, M., Sheehy, M., Pellicer, X.M., McKeown, C., Ryan, G., Kopačková, V., Frei, M., Kuhn, D., Hermanns, R.L., Koulermou, N., Smith, C.A., Engdahl, M., Buxó, P., Gonzalez, M., Dashwood, C., Reeves, H., Cigna, F., Liščák, P., Pauditš, P., Mikulėnas, V., Demir, V., Raha, M., Quental, L., Sandić, C., Fusi, B., Jensen, O.A., 2018. Landslide databases in the geological surveys of Europe. Landslides 15, 359–379. https://doi.org/10.1007/s10346-017-0902-z.

Hijmans, R.J., Cameron, S.E., Parra, J.L., Jones, P.G., Jarvis, A., 2005. Very high resolution interpolated climate surfaces for global land areas. Int. J. Climatol. 25, 1965–1978. https://doi.org/10.1002/joc.1276.

Hovius, N., Stark, C.P., Allen, P.A., 1997. Sediment flux from a mountain belt derivedby landslide mapping. Geology 25, 231–234.

Huang, Q., Wang, Y., Xu, J., Nishyirimbere, A., Li, Z., 2017. Geo-hazard detection and monitoring using SAR and optical images in a snow-covered area: the Menyuan (China) test site. ISPRS Int. J. Geo Inf. 6, 293. https://doi.org/10.3390/ijgi6100293.

Hung, J.J., Lee, C.T., Lin, M.L., 2002. Tsao-Ling rockslide, Taiwan. In: Catastrophic Landslides. Geological Society of America, pp. 91–115. https://doi.org/10.1130/REG15-p91.

Hungr, O., Evans, S.G., Bovis, M.J., Hutchinson, J.N., 2001. A review of the classification of landslides of the flow type. Environ. Eng. Geosci. 7, 221–238. https://doi.org/10.2113/gseegeosci.7.3.221.

Hungr, O., Leroueil, S., Picarelli, L., 2014. The varnes classification of landslide types, an update. Landslides 11, 167–194. https://doi.org/10.1007/s10346-013-0436-y.

ICEYE, 2020. Iceye SAR Data. https://www.iceye.com/sar-data (Accessed: 2020-06-05).

IEEE, 2020. IEEE Standard Letter Designations for Radar-Frequency Bands. IEEE Std 521-2019 (Revision of IEEE Std 521–2002), pp. 1–15.

Inyang, H., Daniels, J., 2009. Environmental Monitoring -Volume I. EOLSS Publications.

Jackson Jr., L., Bobrowsky, P.T., Bichler, A., 2012. Identification, Maps and Mapping. Technical Report. Geological Survey of Canada. https://doi.org/10.4095/292122.

Jacob, A.W., Vicente-Guijalba, F., Lopez-Martinez, C., Lopez-Sanchez, J.M., Litzinger, M., Kristen, H., Mestre-Quereda, A., Ziółkowski, D., Lavalle, M., Notarnicola, C., Suresh, G., Antropov, O., Ge, S., Praks, J., Ban, Y., Pottier, E., Mallorqu Franquet, J. J., Duro, J., Engdahl, M.E., 2020. Sentinel-1 InSAR coherence for land cover mapping: a comparison of multiple feature-based classifiers. IEEE J. Select. Topics Appl. Earth Observ. Remote Sens. 13, 535–552.

Jakob, M., 2005. A size classification for debris flows. Eng. Geol. 79, 151–161. https://doi.org/10.1016/j.enggeo.2005.01.006.

Jin, X., Han, J., 2010. K-Means Clustering. https://doi.org/10.1007/978-0-387-30164-8_425.

Joyce, K.E., Belliss, S.E., Samsonov, S.V., McNeill, S.J., Glassey, P.J., 2009. A review of the status of satellite remote sensing and image processing techniques for mapping natural hazards and disasters. Progress Phys. Geogr. 33, 183–207. https://doi.org/10.1177/0309133309339563.

Jung, J., Yun, S.H., 2020. Evaluation of coherent and incoherent landslide detection methods based on synthetic aperture radar for rapid response: a case study for the 2018 Hokkaido landslides. Remote Sens. 12, 265. https://doi.org/10.3390/rs12020265.

KARI, 2020. Korea Multi-Purpose Satellite (kompsat, arirang). https://www.kari.re.kr/eng/sub03_02_01.do. (Accessed 4 June 2020).

Khalil, R.Z., Saad-ul-Haque, 2018. InSAR coherence-based land cover classification of Okara, Pakistan. Egypt. J. Remote Sens. Space Sci. 21, S23–S28. https://doi.org/10.1016/j.ejrs.2017.08.005.

Kim, Y., van Zyl, J., 2001. Comparison of forest parameter estimation techniques using SAR data. In: IGARSS 2001. Scanning the Present and Resolving the Future. Proceedings IEEE 2001 International Geoscience and Remote Sensing Symposium, pp. 1395–1397. https://doi.org/10.1109/IGARSS.2001.976856.

Kim, Y., van Zyl, J.J., 2009. A time-series approach to estimate soil moisture using polarimetric radar data. IEEE Trans. Geosci. Remote Sens. 47, 2519–2527. https://doi.org/10.1109/TGRS.2009.2014944.

Kirschbaum Bach, D., Adler, R.F., Hong, Y., Hill, S., Lerner-Lam, A., 2009. A global landslide catalog for hazard applications: Method, results, and limitations. Nat. Hazards 52, 561–575. https://doi.org/10.1007/s11069-009-9401-4.

Kirschbaum, D., Stanley, T., 2018. Satellite-based assessment of rainfall-triggered landslide hazard for situational awareness. Earth's Future 6, 505–523. https://doi.org/10.1002/2017EF000715.

Kirschbaum, D., Stanley, T., Zhou, Y., 2015. Spatial and temporal analysis of a global landslide catalog. Geomorphology 249, 4–15. https://doi.org/10.1016/j.geomorph.2015.03.016.

Kjekstad, O., Highland, L., 2009. Economic and social impacts of landslides. In: Sassa, K., Canuti, P. (Eds.), Landslides – Disaster Risk Reduction. Springer Berlin Heidelberg, Berlin, Heidelberg, pp. 573–587. https://doi.org/10.1007/978-3-540-69970-5_30.

Konishi, T., Suga, Y., 2017. Extraction of damaged area caused by debris flows in Hiroshima using COSMO-SkyMed images. In: Notarnicola, C., Pierdicca, N., Santi, E. (Eds.), Active and Passive Microwave Remote Sensing for Environmental Monitoring, International Society for Optics and Photonics. SPIE, pp. 25–33. https://doi.org/10.1117/12.2277679.

Konishi, T., Suga, Y., 2018a. Landslide detection using COSMO-SkyMed images: a case study of a landslide event on Kii Peninsula, Japan. Eur. J. Remote Sens. 51, 205–221. https://doi.org/10.1080/22797254.2017.1418185.

Konishi, T., Suga, Y., 2018b. Landslide detection using polarimetric ALOS-2/PALSAR-2 data: a case study of 2016 Kumamoto earthquake in Japan. In: Bovenga, F., Notarnicola, C., Pierdicca, N., Santi, E. (Eds.), Active and Passive Microwave Remote Sensing for Environmental Monitoring II, International Society for Optics and Photonics. SPIE, pp. 54–61. https://doi.org/10.1117/12.2324030.

Kyriou, A., Nikolakopoulos, K., 2018a. A synergy of radar and optical data of Copernicus programme for landslide mapping. In: Michel, U., Schulz, K. (Eds.), Earth Resources and Environmental Remote Sensing/GIS Applications IX, International Society for Optics and Photonics. SPIE, pp. 106–114. https://doi.org/10.1117/12.2325622.

Kyriou, A., Nikolakopoulos, K., 2018b. Assessing the suitability of Sentinel-1 data for landslide mapping. Eur. J. Remote Sens. 51, 402–411. https://doi.org/10.1080/22797254.2018.1444944.

Lanari, R., Mora, O., Manunta, M., Mallorqui, J., Berardino, P., Sansosti, E., 2004. A small-baseline approach for investigating deformations on full-resolution differential SAR interferograms. IEEE Trans. Geosci. Remote Sens. 42, 1377–1386. https://doi.org/10.1109/TGRS.2004.828196.

Lauknes, T., Shanker, A.P., Dehls, J., Zebker, H., Henderson, I., Larsen, Y., 2010. Detailed rockslide mapping in northern Norway with small baseline and persistent scatterer interferometric SAR time series methods. Remote Sens. Environ. 114, 2097–2109. https://doi.org/10.1016/j.rse.2010.04.015.

Lavé, J., Burbank, D.W., 2004. Denudation processes and rates in the Transverse Ranges, southern California: Erosional response of a transitional landscape to external and anthropogenic forcing. J. Geophys. Res. 109 (F01006).

Lee, J.S., 1981. Speckle analysis and smoothing of synthetic aperture radar images. Comp. Graph. Image Process. 17, 24–32. https://doi.org/10.1016/S0146-664X(81)80005-6.

Lee, J.S., 1986. Speckle suppression and analysis for Synthetic Aperture Radar Images. Opt. Eng. 25, 636–643. https://doi.org/10.1117/12.7973877.

Lee, S., 2010. Overview of kompsat-5 program, mission, and system. In: 2010 IEEE International Geoscience and Remote Sensing Symposium, pp. 797–800.

Lee, J., Pottier, E., 2017. Polarimetric Radar Imaging: From Basics to Applications. Optical Science and Engineering. CRC Press.

Lee, J., Jurkevich, L., Dewaele, P., Wambacq, P., Oosterlinck, A., 1994a. Speckle filtering of synthetic aperture radar images: a review. Remote Sens. Rev. 8 https://doi.org/10.1080/02757259409532206.

Lee, J.S., Grunes, M.R., Kwok, R., 1994b. Classification of multi-look polarimetric SAR imagery based on complex wishart distribution. Int. J. Remote Sens. 15, 2299–2311. https://doi.org/10.1080/01431169408954244.

Leroueil, S., Vaunat, J., Picarelli, L., Locat, J., Senneset, K., 1996. Geotechnical characterization of slope movements, international symposium; 7th, landslides. In: Landslides, 7th Landslides International Symposium, A.A. Balkema, pp. 53–74.

Li, N., Wang, R., Deng, Y., Liu, Y., Li, B., Wang, C., Balz, T., 2014a. Unsupervised polarimetric synthetic aperture radar classification of large-scale landslides caused by wenchuan earthquake in hue-saturation-intensity color space. J. Appl. Remote. Sens. 8, 1–9. https://doi.org/10.1117/1.JRS.8.083595.

Li, N., Wang, R., Deng, Y., Liu, Y., Wang, C., Balz, T., Li, B., 2014b. Polarimetric response of landslides at X-band following the wenchuan earthquake. IEEE Geosci. Remote Sens. Lett. 11, 1722–1726. https://doi.org/10.1109/LGRS.2014.2306820.

Liu, X., Zhao, C., Zhang, Q., Peng, J., Zhu, W., Lu, Z., 2018. Multi-temporal loess landslide inventory mapping with C-, X- and L-band SAR datasets—a case study of Heifangtai loess landslides, China. Remote Sens. 10, 1756. https://doi.org/10.3390/rs10111756.

Lombardo, L., Opitz, T., Ardizzone, F., Guzzetti, F., Huser, R., 2020. Space-time landslide predictive modelling. Earth Sci. Rev. 209, 103318. https://doi.org/10.1016/j.earscirev.2020.103318.

Lopès, A., Garello, R., Le Hégarat-Mascle, S., 2008. Speckle models. In: Matre, H. (Ed.), Processing of Synthetic Aperture Radar Images. ISTE, London, UK, pp. 87–142. https://doi.org/10.1002/9780470611111.ch5.

Lu, P., Stumpf, A., Kerle, N., Casagli, N., 2011. Object-oriented change detection for landslide rapid mapping. In: Geoscience and Remote Sensing Letters, 8. IEEE, pp. 701–705. https://doi.org/10.1109/LGRS.2010.2101045.

Lu, P., Bai, S., Tofani, V., Casagli, N., 2019a. Landslides detection through optimized hot spot analysis on persistent scatterers and distributed scatterers. ISPRS J. Photogramm. Remote Sens. 156, 147–159. https://doi.org/10.1016/j.isprsjprs.2019.08.004.

Lu, P., Qin, Y., Li, Z., Mondini, A.C., Casagli, N., 2019b. Landslide mapping from multi-sensor data through improved change detection-based markov random field. Remote Sens. Environ. 231, 111235. https://doi.org/10.1016/j.rse.2019.111235.

Luo, S., Tong, L., Chen, Y., Tan, L., 2016. Landslides identification based on polarimetric decomposition techniques using Radarsat-2 polarimetric images. Int. J. Remote Sens. 37, 2831–2843. https://doi.org/10.1080/01431161.2015.1041620.

Lv, Z.Y., Shi, W., Zhang, X., Benediktsson, J.A., 2018. Landslide inventory mapping from bitemporal high-resolution remote sensing images using change detection and multiscale segmentation. IEEE J. Select. Topics Appl. Earth Observ. Remote Sens. 11, 1520–1532.

Mabu, S., Nakayama, Y., Kuremoto, T., 2020. Landslide classification from synthetic aperture radar images using convolutional neural network with multichannel information. J. Signal Process. 24, 61–73. https://doi.org/10.2299/jsp.24.61.

Malamud, B.D., Turcotte, D.L., Guzzetti, F., Reichenbach, P., 2004a. Landslide inventories and their statistical properties. Earth Surf. Process. Landf. 29, 687–711. https://doi.org/10.1002/esp.1064.

Malamud, B.D., Turcotte, D.L., Guzzetti, F., Reichenbach, P., 2004b. Landslides, earthquakes, and erosion. Earth Planet. Sci. Lett. 229, 45–59. https://doi.org/10.1016/j.epsl.2004.10.018.

Manconi, A., 2019. Technical note: Limitations on the Use of Space Borne Differential Sar Interferometry for Systematic Monitoring and Failure Forecast of Alpine Landslides. https://doi.org/10.31223/osf.io/3nmqj.

Manconi, A., Casu, F., Ardizzone, F., Bonano, M., Cardinali, M., De Luca, C., Gueguen, E., Marchesini, I., Parise, M., Vennari, C., Lanari, R., Guzzetti, F., 2014. Brief communication: Rapid mapping of landslide events: the 3 December 2013

Montescaglioso landslide, Italy. Nat. Hazards Earth Syst. Sci. 14, 1835–1841. https://doi.org/10.5194/nhess-14-1835-2014.
Mateos, R.M., López-Vinielles, J., Poyiadji, E., Tsagkas, D., Sheehy, M., Hadjicharalambous, K., Liscák, P., Podolski, L., Laskowicz, I., Iadanza, C., Gauert, C., Todorović, S., Auflič, M.J., Maftei, R., Hermanns, R.L., Kociu, A., Sandić, C., Mauter, R., Sarro, R., Béjar, M., Herrera, G., 2020. Integration of landslide hazard into urban planning across Europe. Landsc. Urban Plan. 196, 103740. https://doi.org/10.1016/j.landurbplan.2019.103740.
Matsuoka, M., Yamazaki, F., 2004. Use of satellite SAR intensity imagery for detecting building areas damaged due to earthquakes. Earthquake Spectra 20, 975–994. https://doi.org/10.1193/1.1774182.
Meyer, F., 2019. Chapter 2. Spaceborne Synthetic aperture radar: principles, data access, and basic processing techniques. In: The SAR Handbook. Comprehensive Methodologies for Forest Monitoring and Biomass Estimation, vol. 1, p. 307. https://doi.org/10.25966/nr2c-s697.
Michie, D., Spiegelhalter, D., Taylor, C., 1994. Machine Learning, Neural and Statistical Classification. Prentice Hall.
Michoud, C., Baumann, V., Lauknes, T.R., Penna, I., Derron, M.H., Jaboyedoff, M., 2016. Large slope deformations detection and monitoring along shores of the Potrerillos dam reservoir, Argentina, based on a small-baseline Insar approach. Landslides 13, 451–465. https://doi.org/10.1007/s10346-015-0583-4.
MirMazloumi, S.M., Sahebi, M.R., 2016. Assessment of different backscattering models for bare soil surface parameters estimation from SAR data in band C, L and P. Eur. J. Remote Sens. 49, 261–278. https://doi.org/10.5721/EuJRS20164915.
Mondini, A.C., 2017. Measures of spatial autocorrelation changes in multitemporal SAR images for event landslides detection. Remote Sens. 9 https://doi.org/10.3390/rs9060554.
Mondini, A.C., Chang, K.T., 2014. Combining spectral and geoenvironmental information for probabilistic event landslide mapping. Geomorphology 213, 183–189. https://doi.org/10.1016/j.geomorph.2014.01.007.
Mondini, A.C., Chang, K.T., Yin, H.Y., 2011. Combining multiple change detection indices for mapping landslides triggered by typhoons. Geomorphology 134, 440–451. https://doi.org/10.1016/j.geomorph.2011.07.021.
Mondini, A., Viero, A., Cavalli, M., Marchi, L., Herrera, G., Guzzetti, F., 2014. Comparison of event landslide inventories: the Pogliaschina catchment test case, Italy. Nat. Hazards Earth Syst. Sci. 2 https://doi.org/10.5194/nhessd-2-1093-2014.
Mondini, A.C., Chang, K.T., Chiang, S.H., Schlögel, R., Notarnicola, C., Saito, H., 2017. Automatic mapping of event landslides at basin scale in Taiwan using a Montecarlo approach and synthetic land cover fingerprints. Int. J. Appl. Earth Obs. Geoinf. 63, 112–121. https://doi.org/10.1016/j.jag.2017.07.016.
Mondini, A.C., Santangelo, M., Rocchetti, M., Rossetto, E., Manconi, A., Monserrat, O., 2019. Sentinel-1 SAR amplitude imagery for rapid landslide detection. Remote Sens. 11 https://doi.org/10.3390/rs11070760.
Moro, M., Saroli, M., Salvi, S., Stramondo, S., Doumaz, F., 2007. The relationship between seismic deformation and deep-seated gravitational movements during the 1997 Umbria–Marche (Central Italy) earthquakes. Geomorphology 89, 297–307. https://doi.org/10.1016/j.geomorph.2006.12.013.
Mukunoki, T., Kasama, K., Murakami, S., Ikemi, H., Ishikura, R., Fujikawa, T., Yasufuku, N., Kitazono, Y., 2016. Reconnaissance report on geotechnical damage caused by an earthquake with JMA seismic intensity 7 twice in 28h, Kumamoto, Japan. Soils Found. 56, 947–964. https://doi.org/10.1016/j.sandf.2016.11.001.
Mwaniki, M., Kuria, D., Boitt, M., Ngigi, T., 2017. Image enhancements of Landsat 8 (OLI) and SAR data for preliminary landslide identification and mapping applied to the central region of Kenya. Geomorphology 282, 162–175. https://doi.org/10.1016/j.geomorph.2017.01.015.
Nadim, F., Kjekstad, O., Peduzzi, P., Herold, C., Jaedicke, C., 2006. Global landslide and avalanche hotspots. Landslides 3, 159–173. https://doi.org/10.1007/s10346-006-0036-1.
Nadim, F., Jaedicke, C., Smebye, H., Kalsnes, B., 2013. Assessment of global landslide hazard hotspots. In: Sassa, K., Rouhban, B., Briceño, S., McSaveney, M.J., He, B. (Eds.), Landslides: Global Risk Preparedness. Springer Berlin Heidelberg, Berlin, Heidelberg, pp. 59–71. https://doi.org/10.1007/978-3-642-22087-6_4.
Nagano, H., Hashimoto, H., Kuroda, Y., Takaoka, H., 2011. Debris flows produced by heavy rains on July 21, 2009 in Hofu City, Japan. In: 5th International Conference on Debris-Flow Hazard Mitigation, pp. 725–733. https://doi.org/10.4408/IJEGE.2011-03.B-079.
NASA, 2020. The Thematic Mapper. https://landsat.gsfc.nasa.gov/the-thematic-mapper/ (Accessed: 2020-06-04).
NASA Earth Observations, 2020. Cloud Fraction (https://neo.sci.gsfc.nasa.gov/view.php?datasetId=MYDAL2_M_CLD_FR date=2019-12-01. Accessed: 2020-06-05).
NASA Jet Propulsion Laboratory, 2020a. AIRSAR, Airborne Synthetic Aperture Radar. https://airsar.jpl.nasa.gov/.
NASA Jet Propulsion Laboratory, 2020b. NASA-ISRO SAR Mission (NISAR). https://nisar.jpl.nasa.gov/.
National Research Council, 2014. Convergence: Facilitating Transdisciplinary Integration of Life Sciences, Physical Sciences, Engineering, and beyond. National Academies Press, Washington, D.C.. https://doi.org/10.17226/18722
Nico, G., Pappalepore, M., Pasquariello, G., Refice, A., Samarelli, S., 2000. Comparison of SAR amplitude vs. coherence flood detection methods – GIS application. Int. J. Remote Sens. 21, 1619–1631. https://doi.org/10.1080/014311600209931.
Nielsen, A.A., Conradsen, K., Skriver, H., 2015. Change detection in full and dual polarization, single- and multifrequency SAR data. IEEE J. Select. Topics Appl. Earth Observ. Remote Sens. 8, 4041–4048. https://doi.org/10.1109/JSTARS.2015.2416434.
Notti, D., Davalillo, J.C., Herrera, G., Mora, O., 2010. Assessment of the performance of x-band satellite radar data for landslide mapping and monitoring: Upper Tena valley case study. Nat. Hazards Earth Syst. Sci. 10, 1865–1875. https://doi.org/10.5194/nhess-10-1865-2010.
Ochiai, H., Sakurai, M., Hogai, D., Goto, S., Wakai, A., Fukuoka, H., Nakamura, S., Kimura, S., 2017. Landslide disasters induced by the northern kyushu heavy rainfall in july 2017. J. Jpn. Landslide Soc. 54, 225–228. https://doi.org/10.3313/jls.54.225.
Ohki, M., Abe, T., Tadono, T., Shimada, M., 2020. Landslide detection in mountainous forest areas using polarimetry and interferometric coherence. Earth Planets Space 72. https://doi.org/10.1186/s40623-020-01191-5.
Okada, Y., 1985. Surface deformation due to shear and tensile faults in a half-space. Bull. Seismol. Soc. Am. 75, 1135–1154.
Olen, S., Bookhagen, B., 2018. Mapping damage-affected areas after natural hazard events using Sentinel-1 coherence time series. Remote Sens. 10, 1272. https://doi.org/10.3390/rs10081272.
Oliver, C., Quegan, S., 2004. Understanding Synthetic Aperture Radar Images. SciTech Radar and Defense Series. SciTech Publ.
Oxioli, D., Boccardo, P., Brovelli, M., Molinari, M., Guarnieri, A., Oxoli, D., 2018. Coherent change detection for repeated-pass interferometric SAR images: an application to earthquake damage assessment on buildings. Int. Arch. Photogramm. Remote. Sens. Spat. Inf. Sci. 383–388. https://doi.org/10.5194/isprs-archives-XLII-3-W4-383-2018.
Park, S.E., Lee, S.G., 2019. On the use of Single-, Dual-, and Quad-Polarimetric SAR observation for landslide detection. ISPRS Int. J. Geo Inf. 8 https://doi.org/10.3390/ijgi8090384.
Peel, M.C., Finlayson, B.L., McMahon, T.A., 2007. Updated world map of the Koeppen-Geiger climate classification. Hydrol. Earth Syst. Sci. 11, 1633–1644. https://doi.org/10.5194/hess-11-1633-2007.
Petley, D.N., 2012. Global patterns of loss of life from landslides. Geology 40, 927–930. https://doi.org/10.1130/G33217.1.
Piciullo, L., Calvello, M., Cepeda, J.M., 2018. Territorial early warning systems for rainfall-induced landslides. Earth Sci. Rev. 179, 228–247. https://doi.org/10.1016/j.earscirev.2018.02.013.
Pike, R.J., 1988. The geometric signature: Quantifying landslide-terrain types from digital elevation models. Math. Geol. 20, 491–511. https://doi.org/10.1007/BF00890333.
Plank, S., 2014. Rapid damage assessment by means of multi-temporal SAR — a comprehensive review and outlook to Sentinel-1. Remote Sens. 6, 4870–4906. https://doi.org/10.3390/rs6064870.
Plank, S., Twele, A., Martinis, S., 2016. Landslide mapping in vegetated areas using change detection based on optical and polarimetric SAR data. Remote Sens. 8, 307.
Pohl, C., Van Genderen, J., 1998. Review article multisensor image fusion in remote sensing: Concepts, methods and applications. Int. J. Remote Sens. 19, 823–854. https://doi.org/10.1080/014311698215748.
Praks, J., Koeniguer, E., Hallikainen, M., 2009. Alternatives to target entropy and alpha angle in SAR polarimetry. In: Geoscience and Remote Sensing, IEEE Transactions on 47, pp. 2262–2274. https://doi.org/10.1109/TGRS.2009.2013459.
Prati, C., Rocca, F., 1993. Improving slant-range resolution with multiple SAR surveys. IEEE Trans. Aerosp. Electron. Syst. 29, 135–143.
Prati, C., Rocca, F., Guarnieri, A.M., Damonti, E., 1990. Seismic migration for SAR focusing: Interferometrical applications. IEEE Trans. Geosci. Remote Sens. 28, 627–640.
Pulliainen, J.T., Heiska, K., Hyyppa, J., Hallikainen, M.T., 1994. Backscattering properties of boreal forests at the C- and X-bands. IEEE Trans. Geosci. Remote Sens. 32, 1041–1050.
Pulvirenti, L., Chini, M., Pierdicca, N., Boni, G., 2017. Detection of flooded urban areas using SAR: An approach based on the coherence of stable scatterers. In: 2017 IEEE International Geoscience and Remote Sensing Symposium, pp. 5701–5704.
Rafi, Z., Ahmed, N., Ur-Rehman, S., Azeem, T., Abd El-Aal, A.E.A.K., 2013. Analysis of Quetta-Ziarat earthquake of 29 October 2008 in Pakistan. Arab. J. Geosci. 6, 1731–1737. https://doi.org/10.1007/s12517-011-0485-2.
Raspini, F., Ciampalini, A., Del Conte, S., Lombardi, L., Nocentini, M., Gigli, G., Ferretti, A., Casagli, N., 2015. Exploitation of amplitude and phase of satellite Sar images for landslide mapping: the case of montescaglioso (South Italy). Remote Sens. 7, 14576–14596. https://doi.org/10.3390/rs71114576.
Raspini, F., Bianchini, S., Ciampalini, A., Del Soldato, M., Solari, L., Novali, F., Del Conte, S., Rucci, A., Ferretti, A., Casagli, N., 2018. Continuous, semi-automatic monitoring of ground deformation using Sentinel-1 satellites. Sci. Rep. 8 https://doi.org/10.1038/s41598-018-25369-w.
Ray, R.L., Lazzari, M., Olutimehin, T., 2020. Remote sensing approaches and related techniques to map and study landslides. In: Ray, R., Lazzari, M. (Eds.), Landslides. IntechOpen, Rijeka. Chapter 2, pp. 1–24. https://doi.org/10.5772/intechopen.93681.
Reichenbach, P., Rossi, M., Malamud, B.D., Mihir, M., Guzzetti, F., 2018. A review of statistically-based landslide susceptibility models. Earth Sci. Rev. 180, 60–91. https://doi.org/10.1016/j.earscirev.2018.03.001.
Rib, H., Liang, T., 1978. Recognition and identification. In: Schuster, R.L., Krizek, R.J. (Eds.), Landslide Analysis and Control. National Academy of Sciences, Washington. Volume 1 of *Transportation Research Board Special Report*, pp. 34–80.
Richards, J., 2009a. Remote Sensing with Imaging Radar. Signals and Communication Technology. Springer, Berlin Heidelberg. https://books.google.it/books?id=DAsz9ZwkGXcC.
Richards, J., 2009b. Remote Sensing with Imaging Radar, Signals and Communication Technology. Springer-Verlag, Berlin Heidelberg. https://doi.org/10.1007/978-3-642-02020-9_1.
Richards, J., Jia, X., 2006. Remote Sensing digital Image Analysis. Springer-Verlag, Berlin Heidelberg. https://doi.org/10.1007/3-540-29711-1.

Richards, J.A., Woodgate, P.W., Skidmore, A.K., 1987. An explanation of enhanced radar backscattering from flooded forests. Int. J. Remote Sens. 8, 1093–1100. https://doi.org/10.1080/01431168708954756.
Righini, G., Pancioli, V., Casagli, N., 2012. Updating landslide inventory maps using persistent scatterer interferometry (psi). Int. J. Remote Sens. 33, 2068–2096. https://doi.org/10.1080/01431161.2011.605087.
Roa, Y., Azcueta, M., Berardino, P., Esposito, C., Euillades, L., Euillades, P., Natale, A., Perna, S., 2020. On the interferometric and polarimetric capabilities of the Argentinian L-band Sarat System. In: 2020 IEEE Latin American GRSS ISPRS Remote Sensing Conference (LAGIRS), pp. 640–645.
Robinson, T.R., Rosser, N., Walters, R.J., 2019. The spatial and temporal influence of cloud cover on satellite-based emergency mapping of earthquake disasters. Sci. Rep. 9 https://doi.org/10.1038/s41598-019-49008-0.
Rocca, F., Prati, C., Monti Guarnieri, A., Ferretti, A., 2000. SAR interferometry and its applications. Surv. Geophys. 21, 159–176. https://doi.org/10.1023/A:1006710731155.
Rodriguez, E., Martin, J.M., 1992. Theory and design of interferometric synthetic aperture radars. IEEE Proceedings F - Radar. Signal Process. 139, 147–159.
Rodriguez, K.M., Weissel, J.K., Kim, Y., 2002. Classification of landslide surfaces using fully polarimetric SAR: examples from Taiwan. In: IEEE International Geoscience and Remote Sensing Symposium, 5, pp. 2918–2920. https://doi.org/10.1109/IGARSS.2002.1026821.
Rossi, M., Guzzetti, F., Reichenbach, P., Mondini, A., Peruccacci, S., 2010. Optimal landslide susceptibility zonation based on multiple forecasts. Geomorphology 114, 129–142. https://doi.org/10.1016/j.geomorph.2009.06.020.
Rossi, M., Guzzetti, F., Salvati, P., Donnini, M., Napolitano, E., Bianchi, C., 2019. A predictive model of societal landslide risk in Italy. Earth Sci. Rev. 196, 102849. https://doi.org/10.1016/j.earscirev.2019.04.021.
Salvati, P., Petrucci, O., Rossi, M., Bianchi, C., Pasqua, A.A., Guzzetti, F., 2018. Gender, age and circumstances analysis of flood and landslide fatalities in Italy. Sci. Total Environ. 610-611, 867–879. https://doi.org/10.1016/j.scitotenv.2017.08.064.
Santangelo, M., Marchesini, I., Bucci, F., Cardinali, Mauro, Fiorucci, F., Guzzetti, F., 2015. An approach to reduce mapping errors in the production of landslide inventory maps. Nat. Hazards Earth Syst. Sci. 15, 2111–2126. https://doi.org/10.5194/nhess-15-2111-2015.
Sassa, K., Canuti, P., 2009. Landslides – Disaster Risk Reduction. Springer-Verlag, Berlin Heidelberg. https://doi.org/10.1007/978-3-540-69970-5, 2009.
Scaioni, M., 2013. Remote sensing for landslide investigations: from research into practice. Remote Sens. 5, 5488–5492. https://doi.org/10.3390/rs5115488.
Scaioni, M., Longoni, L., Melillo, V., Papini, M., 2014. Remote sensing for landslide investigations: an overview of recent achievements and perspectives. Remote Sens. 6, 9600–9652. https://doi.org/10.3390/rs6109600.
Schuster, R.L., Highland, L.M., 2001. Socioeconomic and Environmental Impacts of Landslides in the Western Hemisphere. U.S. Geological Survey Open-File Report 01-276. U.S. Geological Survey.
Sharp, P., Hockfield, S., 2017. Convergence: the future of health. Science 355, 589.1–589. https://doi.org/10.1126/science.aam8563.
Sharp, P., Jacks, T., Hockfield, S., 2016. Convergence: The Future of Health. White Paper. MIT, Washington D.C.
Shibayama, T., Yamaguchi, Y., 2013. An application of polarimtric radar analysis on geophysical phenomena. In: 2013 IEEE International Geoscience and Remote Sensing Symposium - IGARSS, pp. 3191–3194. https://doi.org/10.1109/IGARSS.2013.6723505.
Shibayama, T., Yamaguchi, Y., Yamada, H., 2015. Polarimetric scattering properties of landslides in forested areas and the dependence on the local incidence angle. Remote Sens. 7, 15424–15442. https://doi.org/10.3390/rs71115424.
Shimada, M., Watanabe, M., Kawano, N., Ohki, M., Motooka, T., Wada, Y., 2014. Detecting mountainous landslides by SAR polarimetry: a comparative study using Pi-SAR-L2 and X-band SARs. In: Transactions of the Japan Society for Aeronautical and Space Sciences, Aerospace Technology Japan, 12, pp. 9–15.
Sidle, R.C., Ochiai, H., 2006. Landslides: Processes, prediction, and land use. In: Number 18 in Water Resources Monograph. American Geophysical Union, Washington, DC.
Singhroy, V., 1995. SAR integrated techniques for geohazard assessment. Adv. Space Res. 15, 67–78. https://doi.org/10.1016/0273-1177(95)00076-Q.
Singhroy, V., Mattar, K., Gray, A., 1998. Landslide characterisation in Canada using interferometric SAR and combined SAR and TM images. Adv. Space Res. 21, 465–476. https://doi.org/10.1016/S0273-1177(97)00882-X.
Singleton, A., Li, Z., Hoey, T., Muller, J.P., 2014. Evaluating sub-pixel offset techniques as an alternative to D-InSAR for monitoring episodic landslide movements in vegetated terrain. Remote Sens. Environ. 147, 133–144. https://doi.org/10.1016/j.rse.2014.03.003.
Solari, L., Soldato, M.D., Montalti, R., Bianchini, S., Raspini, F., Thuegaz, P., Bertolo, D., Tofani, V., Casagli, N., 2019. A sentinel-1 based hot-spot analysis: landslide mapping in North-Western Italy. Int. J. Remote Sens. 40, 7898–7921. https://doi.org/10.1080/01431161.2019.1607612.
Solari, L., Del Soldato, M., Raspini, F., Barra, A., Bianchini, S., Confuorto, P., Casagli, N., Crosetto, M., 2020. Review of satellite interferometry for landslide detection in Italy. Remote Sens. 12, 1351. https://doi.org/10.3390/rs12081351.
Space, C., 2020. The Capella 36. https://www.capellaspace.com/technology/.
Stramondo, S., Tesauro, M., Briole, P., Sansosti, E., Salvi, S., Lanari, R., Anzidei, M., Baldi, P., Fornaro, G., Avallone, A., 1999. The september 26, 1997 Colfiorito, Italy, earthquakes: Modeled coseismic surface displacement from SAR interferometry and GPS. Geophys. Res. Lett. 26, 883–886. https://doi.org/10.1029/1999GL900141.
Stubenrauch, C.J., Rossow, W.B., Kinne, S., Ackerman, S., Cesana, G., Chepfer, H., Di Girolamo, L., Getzewich, B., Guignard, A., Heidinger, A., Maddux, B.C., Menzel, W.P., Minnis, P., Pearl, C., Platnick, S., Poulsen, C., Riedi, J., Sun-Mack, S., Walther, A., Winker, D., Zeng, S., Zhao, G., 2013. Assessment of global cloud datasets from satellites: project and database initiated by the GEWEX radiation panel. Bull. Am. Meteorol. Soc. 94, 1031–1049. https://doi.org/10.1175/BAMS-D-12-00117.1.
Suga, Y., Konishi, T., 2012. Landslide detection using very high-resolution satellite imageries. In: Entekhabi, D., Honda, Y., Sawada, H., Shi, J., Oki, T. (Eds.), Land Surface Remote Sensing, International Society for Optics and Photonics. SPIE, pp. 348–353. https://doi.org/10.1117/12.976033.
Sun, L., Muller, J.P., 2016. Evaluation of the use of sub-pixel offset tracking techniques to monitor landslides in densely vegetated steeply sloped areas. Remote Sens. 8, 659. https://doi.org/10.3390/rs8080659.
Sun, L., Dabboor, M., Belair, S., Carrera, M.L., Merzouki, A., 2019. Simulating C-band SAR footprint-scale backscatter over agricultural area with a physical land surface model. Water Resour. Res. 55, 4594–4612. https://doi.org/10.1029/2019WR025163.
Tanyaş, H., van Westen, C.J., Allstadt, K.E., Nowicki Jessee, M.A., Görüm, T., Jibson, R.W., Godt, J.W., Sato, H.P., Schmitt, R.G., Marc, O., Hovius, N., 2017. Presentation and analysis of a worldwide database of earthquake-induced landslide inventories. J. Geophys. Res. Earth Surf. 122, 1991–2015. https://doi.org/10.1002/2017JF004236.
Tavakkoli Piralilou, S., Shahabi, H., Jarihani, B., Ghorbanzadeh, O., Blaschke, T., Gholamnia, K., Meena, S.R., Aryal, J., 2019. Landslide detection using multi-scale image segmentation and different machine learning models in the higher Himalayas. Remote Sens. 11 https://doi.org/10.3390/rs11212575.
Tay, C.W.J., Yun, S.H., Chin, S.T., Bhardwaj, A., Jung, J., Hill, E.M., 2020. Rapid flood and damage mapping using synthetic aperture radar in response to Typhoon Hagibis, Japan. Sci. Data 7. https://doi.org/10.1038/s41597-020-0443-5.
Temme, A., Guzzetti, F., Samia, J., Mirus, B.B., 2020. The future of landslides' past— a framework for assessing consecutive landsliding systems. Landslides. https://doi.org/10.1007/s10346-020-01405-7.
Tessari, G., Floris, M., Pasquali, P., 2017. Phase and amplitude analyses of SAR data for landslide detection and monitoring in non-urban areas located in the North-Eastern Italian pre-Alps. Environ. Earth Sci. 76, 85. https://doi.org/10.1007/s12665-017-6403-5.
Tien Bui, D., Shahabi, H., Shirzadi, A., Chapi, K., Alizadeh, M., Chen, W., Mohammadi, A., Ahmad, B.B., Panahi, M., Hong, H., Tian, Y., 2018. Landslide detection and susceptibility mapping by AIRSAR data using support vector machine and index of entropy models in Cameron Highlands, Malaysia. Remote Sens. 10 https://doi.org/10.3390/rs10101527.
Torres, R., Snoeij, P., Geudtner, D., Bibby, D., Davidson, M., Attema, E., Potin, P., Rommen, B., Floury, N., Brown, M., Traver, I.N., Deghaye, P., Duesmann, B., Rosich, B., Miranda, N., Bruno, C., L'Abbate, M., Croci, R., Pietropaolo, A., Huchler, M., Rostan, F., 2012. GMES Sentinel-1 mission. Remote Sens. Environ. 120, 9–24. https://doi.org/10.1016/j.rse.2011.05.028.
Trigila, A., Iadanza, C., Spizzichino, D., 2010. Quality assessment of the Italian Landslide Inventory using GIS processing. Landslides 7, 455–470. https://doi.org/10.1007/s10346-010-0213-0.
Turner, A.K., Schuster, R.L. (Eds.), 1996. Landslides: Investigation and Methods. volume 1 of *Transportation Research Board*, First ed. The National Academies of Sciences Engineering Medicine.
Tzouvaras, M., Danezis, C., Hadjimitsis, D.G., 2020. Small scale landslide detection using sentinel-1 interferometric Sar coherence. Remote Sens. 12, 1560. https://doi.org/10.3390/rs12101560.
Uemoto, J., Moriyama, T., Nadai, A., Kojima, S., Umehara, T., 2019. Landslide detection based on height and amplitude differences using pre- and post-event airborne X-band SAR data. Nat. Hazards 95, 485–503. https://doi.org/10.1007/s11069-018-3492-8.
Ulaby, F., Kouyate, F., Fung, A., Sieber, A.J., 1982. A backscatter model for a randomly perturbed periodic surface. IEEE Trans. Geosci. Remote Sens. GE-20, 518–528. https://doi.org/10.1109/TGRS.1982.350420.
UNESCO Working Party on World Landslide Inventory, 1993. A suggested method for describing the activity of a landslide. Bull. Int. Assoc. Eng. Geol. 47, 53–57. https://doi.org/10.1007/BF02639593.
UNESCO Working Party on World Landslide Inventory, 1995. A suggested method for describing the rate of movement of a landslide. Bull. Int. Assoc. Eng. Geol. 52, 75–78. https://doi.org/10.1007/BF02602683.
Van Den Eeckhaut, M., Hervás, J., 2012. State of the art of national landslide databases in Europe and their potential for assessing landslide susceptibility, hazard and risk. Geomorphology 139–140, 545–558. https://doi.org/10.1016/j.geomorph.2011.12.006.
van Zyl, J.J., 1993. Application of Cloude's target decomposition theorem to polarimetric imaging radar data. In: Mott, H., Boerner, W.M. (Eds.), Radar Polarimetry, International Society for Optics and Photonics. SPIE, pp. 184–191. https://doi.org/10.1117/12.140615.
Vanmaercke, M., Kettner, A.J., Eeckhaut, M.V.D., Poesen, J., Mamaliga, A., Verstraeten, G., Rădoane, M., Obreja, F., Upton, P., Syvitski, J.P., Govers, G., 2014. Moderate seismic activity affects contemporary sediment yields. Progress Phys. Geogr. 38, 145–172. https://doi.org/10.1177/0309133313516160.
Vanmaercke, M., Ardizzone, F., Rossi, M., Guzzetti, F., 2017. Exploring the effects of seismicity on landslides and catchment sediment yield: an Italian case study. Geomorphology 278, 171–183. https://doi.org/10.1016/j.geomorph.2016.11.010.
Vargas Cuervo, G., 1997. Evaluacion de imagenes de satelite SAR ERS-1 y Spot-Landsat en la cartografia de movimientos en masa. In: Guyenne, T.D. (Ed.), The Use and Applications of ERS in Latin America, p. 109.
Vasile, G., Trouve, E., Lee, Jong-Sen, Buzuloiu, V., 2006. Intensity-driven adaptive-neighborhood technique for polarimetric and interferometric SAR parameters estimation. IEEE Trans. Geosci. Remote Sens. 44, 1609–1621. https://doi.org/10.1109/TGRS.2005.864142.

Wang, F., Wu, Y.H., Yang, H., Tanida, Y., Kamei, A., 2015. Preliminary investigation of the 20 August 2014 debris flows triggered by a severe rainstorm in Hiroshima City, Japan. Geoenviron. Disasters 2. https://doi.org/10.1186/s40677-015-0025-6.

Watanabe, M., Yonezawa, C., Iisaka, J., Sato, M., 2012. Alos/palsar full polarimetric observations of the Iwate–Miyagi Nairiku earthquake of 2008. Int. J. Remote Sens. 33, 1234–1245. https://doi.org/10.1080/01431161.2011.554453.

Watanabe, M., Thapa, R., Shimada, M., 2016. Pi-SAR-L2 observation of the landslide caused by Typhoon Wipha on Izu Oshima island. Remote Sens. 8, 282. https://doi.org/10.3390/rs8040282.

Williams, J.G., Rosser, N.J., Kincey, M.E., Benjamin, J., Oven, K.J., Densmore, A.L., Milledge, D.G., Robinson, T.R., Jordan, C.A., Dijkstra, T.A., 2018. Satellite-based emergency mapping using optical imagery: experience and reflections from the 2015 Nepal earthquakes. Nat. Hazards Earth Syst. Sci. 18, 185–205. https://doi.org/10.5194/nhess-18-185-2018.

Xu, C., Ma, S., Tan, Z., Xie, C., Toda, S., Huang, X., 2017. Landslides triggered by the 2016 Mj 7.3 Kumamoto, Japan, earthquake. Landslides 15, 1–14. https://doi.org/10.1007/s10346-017-0929-1.

Xue, D., He, Z., Hu, D., 2011. Application of radar remote sensing in landslide geohazard risk assessment. In: Li, J. (Ed.), International Symposium on Lidar and Radar Mapping 2011: Technologies and Applications, International Society for Optics and Photonics. SPIE, pp. 579–584. https://doi.org/10.1117/12.912922.

Yamagishi, H., Yamazaki, F., 2018. Landslides by the 2018 Hokkaido Iburi-Tobu Earthquake on September 6. Landslides 15, 2521–2524. https://doi.org/10.1007/s10346-018-1092-z.

Yamaguchi, Y., 2012. Disaster monitoring by fully polarimetric SAR data acquired with alos-palsar. Proc. IEEE 100, 2851–2860. https://doi.org/10.1109/JPROC.2012.2195469.

Yang, Jian, Peng, Ying-Ning, Lin, Shi-Ming, 2001. Similarity between two scattering matrices. Electron. Lett. 37, 193–194. https://doi.org/10.1049/el:20010104.

Yang, H., Wang, F., Miyajima, M., 2015. Investigation of shallow landslides triggered by heavy rainfall during typhoon Wipha (2013), Izu Oshima Island, Japan. Geoenviron. Disasters 2. https://doi.org/10.1186/s40677-015-0023-8.

Yisok, Oh., 2004. Quantitative retrieval of soil moisture content and surface roughness from multipolarized radar observations of bare soil surfaces. IEEE Trans. Geosci. Remote Sens. 42, 596–601. https://doi.org/10.1109/TGRS.2003.821065.

Yonezawa, C., Watanabe, M., Saito, G., 2012. Polarimetric decomposition analysis of alos palsar observation data before and after a landslide event. Remote Sens. 4, 2314–2328. https://doi.org/10.3390/rs4082314.

Yun, S.H., Hudnut, K., Owen, S., Webb, F., Simons, M., Sacco, P., Gurrola, E., Manipon, G., Liang, C., Fielding, E., Milillo, P., Hua, H., Coletta, A., 2015. Rapid damage mapping for the 2015 Mw 7.8 Gorkha Earthquake using Synthetic Aperture Radar data from COSMO–SkyMed and ALOS-2 satellites. Seismol. Res. Lett. 86, 1549–1556. https://doi.org/10.1785/0220150152.

Zhao, C., Lu, Z., 2018. Remote sensing of landslides—a review. Remote Sens. 10, 279. https://doi.org/10.3390/rs10020279.

Zhong, C., Liu, Y., Gao, P., Chen, W., Li, H., Hou, Y., Nuremanguli, T., Ma, H., 2020. Landslide mapping with remote sensing: challenges and opportunities. Int. J. Remote Sens. 41, 1555–1581. https://doi.org/10.1080/01431161.2019.1672904.